UNIVERSITY OF OKLAHOMA

GRADUATE COLLEGE

Prospecting for Elements: Galactic Halo Planetary Nebulae Abundances & Virgo Spiral Galaxy Color Profiles

A Dissertation

SUBMITTED TO THE GRADUATE FACULTY

In partial fulfillment of the requirements
for the degree of

Doctor of Philosophy

by

JOSEPH W. HOWARD

Norman, Oklahoma
1998

UMI Number: 9839818

UMI
300 North Zeeb Road
Ann Arbor, MI 48103

PROSPECTING FOR ELEMENTS: GALACTIC HALO PLANETARY NEBULAE ABUNDANCES & VIRGO SPIRAL GALAXY COLOR PROFILES

A Dissertation APPROVED FOR THE
DEPARTMENT OF PHYSICS AND ASTRONOMY

BY

Dr. Richard C. Henry

Dr. William J. Romanishin

Dr. John J. Cowan

Dr. Edward A. Baron

Dr. Richard D. Elmore

Acknowledgments

Where does someone start an acknowledgement when he has benefited from so many wonderful people? I consider myself extremely lucky to have had a rewarding experience in almost everything I have ever accomplished, but I certainly would not be here today without help.

To my wife Mindy: How often have I turned to you for help, advice, emotional support, and understanding? More times than I can count. You are my strength. You are my heart. You are my motivator. I hope I do you a similar justice. I thank you for all that you have ever done for me. And, yes, I am going to say, "I love ya!"

To my Father: I will not be able to adequately praise you enough in the space provided here. You have always been here for me. I need help, you provide it. I need advice, you give it. I need a good kick in the pants, you provide the foot. I have learned so much from your love and dedication. You have given me my confidence. You have taught me how to be a man. You showed me how to go after opportunity, how to never give up, and have courage.

To my Mother: I owe you, especially you, everything. I remember that summer long ago as a child where you taught me to read, much to my displeasure. I now look back to that time as the most important defining moment in my life. I owe you my education. You showed me that I could use my mind. Without a doubt, my mother, is the most important key in everything that I have ever accomplished. I will state for everyone that my mom in the best in the world.

To my Big Brother & Sister: Thank you for giving me guidance throughout my life. You have forged the way ahead of me and have provided me with great insight.

To my Grandparents: I never got a chance to meet some of you, others I knew very well. Nana & Papa, thank you for the help in providing for my education. Granddad Joe, I wish I could have known you. Grandma Joe, you taught me how to be feisty. I miss you all dearly.

To Dr. Henry: I want to thank you for being my advisor these many years and causing my great interest in all the cloudy structures in the universe. My graduate education has benefited from your caring, patient, and methodical ways of investigation. Thank you for helping me find an aim, an interest, and a curiosity about all the interesting structures, places, and processes going on in the universe.

To Dr. Romanishin: I want to thank you for providing the observational materials for this study. I also want to thank you for graciously answering my questions as I learned the technology, observational techiniques, and craft of image reduction.

To Dave Minard: I want to thank you for all your concerned effort and help tutoring me in the use of the IRAF and AWK packages. I also want to thank you for any and all help you kindly provided to make this study possible.

To my committee members: Thank you for your time and consideration. I thank you.

To the "Crew": Many fine graduate students have come and gone through Nielsen 403. I am glad to have worked, known, and become friends with all of you. Tim, Xu, Francesca, Christi, Jackie, Steve, Chris, Shahriar, Jim, Tom, and Tom - Thank You!

To the Universe: Thank you being there and being so darned intriging. One day I hope to unravel more of your mysteries.

Contents

List of Tables

List of Figures

Abstract

Halo Planetary Nebulae

Using published spectral line data for nine halo planetary nebulae (HPNe), I have calculated photoionization models in an attempt to gain insight into the physical conditions and chemical abundances of these nebulae. The nine HPNE reported upon are K648, DdDm-1, NGC2242, NGC4361, PN243.8-37.1, PN006-41.9, M2-29, BB-1, and H4-1. The derived abundance ranges for the HPNe are: C 6.60-8.95, N 7.18-8.00, O 7.56-8.56, Ne 6.24-7.71, Ar 4.12-7.70, and S 4.90-7.00 [log(x)+12]. The temperature range for the central stars of these nebulae is 40,000 to 140,000K. Specifically, with a few exceptions, I find that all nine objects exhibit subsolar O/H: most show enhanced C/O and N/O, and a constant Ne/O ration. I also note the existence of comparatively larger abundance scatter in the HPNe as opposed to disk PNe, and suggest that this is consistent with the accretion model of halo formation formulated by Searle & Zinn. In addition, I test the effects on derived abundances and central star temperatures of a variety of model atmospheres as well as blackbodies for input ionizing spectra. I find that nebular line strengths are relatively insensitive to atmospheric details; thus blackbody spectra are suitable for central star continua.

Near-Infrared Virgo Cluster Spiral Colors

Near-infrared (NIR) surface photometry in J (1.2μm), H (1.6μm) and K (2.2μm) have been obtained for a sample of Virgo cluster spirals; NGC4321, NGC4303, NGC4571, NGC4689, and NGC4254 which span a large range in HI deficiency. The spirals range from a normal gas content to a deficiency of a factor of 10 compared to normal galaxies. Using previous HII region abundance studies along with the NIR colors an attempt has been made to calibrate any correlation between the J-K index to the overall gas phase abundance gradients as a first step to probing the underlying stellar metallicity. Decomposition techniques have been used to produce estimates of spiral bulge/disk masses and luminosities in all three J, H, & K bands, as well as to explore the variation of mass-to-light ratios within the separate galaxy components. An analysis of the NIR colors is performed in an attempt to unravel the similar effects that stellar ages, dust content, metallicity, and some non-stellar emission processes has upon colors. The derived color gradients for the J-K index are very shallow and show a range of behaviors across the galaxy sample.

Thesis Author: Joseph W. Howard
Thesis Advisor: Dr. Richard C. Henry

Chapter 1

Why go Prospecting?

Chemical abundances in spiral galaxies represent the result of billions of years of dynamical and chemical evolution. Fundamental processes such as star formation, stellar nucleosynthesis, and gas infall operate simultaneously at rates which are both a function of time and location to ultimately produce the abundance patterns observed today. Therefore, understanding the general form of any differing abundance patterns, how it varies from galactic bulge to halo to disk, galaxy to galaxy, and indeed the origin of the differences is extremely important for learning about the individual processes as well as how they work together within a galaxy.

It is to this end that two realms of research have been undertaken: the rather local study of galactic halo planetary nebulae and the large distance and time removed study of radial abundance patterns in extra-galactic spiral galaxies.

1. Halo Planetary Nebulae

Planetary nebulae (PNe) are spherical shells of low-density gas that have been blown off by the death spasms of their very hot central stars. The progenitors of PNe are intermediate mass stars with zero-age main sequence masses ranging from $0.8M_{\odot}$ to nearly $8.0M_{\odot}$. The standard model for the formation of a planetary nebula follows the idea that as intermediate mass stars leave their eventual red giant phase and before the central core becomes a white dwarf the remaining outer envelope of the star is ejected, forming the structure of a planetary nebula (Peimbert 1990).

The study of this gaseous remnant and its behavior can provide the chemical compostion of some fourteen different elements: H, He, C, N, O, Ne, Na, Mg, Al, Si, S, Ar, Ca, and sometimes, but not often even Fe, and Ni. The gas that makes up the PNe has, to some extent, undergone some processing during the stellar chemical evolution of the progenitor star. Current ideas about the evolution of chemical content as intermediate mass stars evolve to produce PNe place those elements into two groups: those inextricably linked and affected by stellar nucleosynthesis events, such as H, He, C, N, and possibly O and those not thought to be altered by further processing, such as Ne, S, and Ar (Buell 1998, Boothroyd & Sackmann 1988). Qualitative and quantitative research on the first group can lead to further understanding and constraints on the chemical yields of stellar evolution models, while the abundances of the second group of elements are mostly indicative of the progenitor's elemental composition as it originally formed.

Since a PN is just a low-density gas that is heated and ionized by the intense radiation field of the central white dwarf, it is possible under these circumstances to use photoionization codes to predict the physical conditions, ionization structure, gas and electron density, temperature, elemental abundances, and its resulting emission-line spectrum once compared to observation in a unique and self-consistent process. By simultaneously solving rigorous equations pertaining to thermal and statistical equilibrium along with the accompanying heating and cooling processes in the PNe a definitive synopsis of the basic structure of the PNe can be obtained (Ferland 1990).

Halo planetary nebulae (HPNe) are a further subset of PNe that are a classification unto themselves because of their markedly different chemical and dynamical make-up compared to regular disk and bulge PNe (Peimbert 1990). HPNe offer the chance to study a group of planetary nebulae that are metal deficient, the stellar progenitor's chemical evolution under such conditions, and to explore the chemical composition of the remote galactic suburbs. Once comparisons and differences are drawn to galactic disk and bulge PNe, there can be no doubt that a great deal can be concluded from the respective chemical histories of HPNe.

Planetary nebulae offer a chance to study a large range in nucleosynthetic history and evolution, differences in many stellar populations with various range of ages, and the ability to explore a significant range in initial metallicities especially with HPNe. The determination of the chemical compositions of halo planetary nebulae is essential to the further pursuit in understanding the chemical evolution of, at least, our galaxy.

2. Virgo Cluster Spiral Galaxies

Spiral galaxies have found an elite status in helping to determine the chemical and physical parameters governing galactic evolution. For many years the physical parameters of spiral galaxies have been determined in a multitude of ways: broadband colors have been used to estimate the stellar populations (Worthey 1994), HII regions have been used to find abundance variations within galaxies (Henry et al. 1992, Henry et al. 1994, Henry & Howard 1995, Skillman et al. 1996, Vila-Costas & Edmunds 1992), and kinematical properties have been used to explore not only processes that might lead to the chemical structure of the galaxy but also its past and future chemo-stellar populations (Worthey 1994, Vazdekis et al. 1996, Guhathakurta et al. 1988, Matteucci 1992, Dopita & Ryder 1994).

The Virgo Cluster, due to its proximity and its high galactic altitude, provides the logical starting point for a study relating Near-Infrared (NIR) colors and chemical abundance variations. The NIR range of wavelengths have the advantage over broadband colors in that it is relatively free of extinction effects, and the NIR comes from the old stellar population which greatly dominates the galactic stellar mass (Charlot & Bruzual 1991). Although multiband imaging and any derived color variations have been used to study the dynamics of different stellar populations in elliptical galaxies, little has been done using color information to derive dynamical and chemical data in late-type spiral galaxies (de Jong 1996).

It is much easier to measure abundances and any respective gradients in the HII region gas phase in spiral galaxies, so why look for a measure of *stellar* abundance gradients? Simply, an analysis of HII regions can not take place to determine abundances where there is not much gas or many large O and B main sequence stars to photoionize the clouds into emission. Finding a NIR color-metallicity relation is of obvious importance in areas were a spiral galaxy may have had most of its gas stripped away, such as one finds in Virgo cluster spirals (Skillman et al. 1996). In addition, there are a number of processes that can alter the abundances of the gas phase of a galaxy differently than that of its constituent stellar component. A continual infall of unenriched gas from a galactic halo would dilute the disk gas perhaps leading to possibly higher metallicities in the stars than the gas (Tinsley 1980, Romanishin 1990). Likewise, stars may form in areas of enhanced metallicity causing a difference in stellar to gas adundances. All of these possible behaviors could result in different abundances and any gradients between what may be determined by HII regions and the stars within a galaxy. It is also quite possible that the form of abundance gradients found in interstellar gas will be very similar to those in the stars. Thus, this study is motivated to explore the idea that NIR color gradients may link with metallicity along with HII region abundance gradients. Specifically, a handful of Virgo cluster spirals, NGC4321, NGC4303, NGC4254, NGC4571, & NGC4689, have been observed in the NIR (J,H,K) passband to investigate the idea that the NIR J-K color can be partially linked with metallicity in the stars and compared to HII region abundances. The J-K index is used for this study because it is directly related to the temperature of giant branch stars and therefore also sensitive to the metallicity of the stars because of the effect that metallicity has on the effective surface temperatures of stars, and since the NIR suffers much less extinction that can erroneously alter color determinations.

There are certain characteristics of the Virgo Cluster spirals that must be taken into account so as to identify any sample biases that may exist. On the whole spirals in the cluster, as opposed to field spirals, show varying degrees of HI deficiency (Henry et al. 1992, Giovanelli & Haynes 1985, Warmels 1986) and appear to be redder and more metal rich for a given morphological type (Skillman et al. 1996). There is ample evidence that close encounters and tidal disturbances, stripping, and shaking have influenced Virgo galaxy evolution (Henry et al. 1994) as well. The cluster also shows a gradient in morphological type moving out in the cluster from early to late Hubble types (Kennicutt 1985). All of these cluster environmental influences can alter their respective chemical and dynamical structures differently than what may be occuring in normal field galaxies. However, most of these effects are small enough not to cause any great harm to the study at hand because the differences are small compared to the intrinsic variations between different individual galaxies.

2.1. Age? Metallicity? Dust?

What could cause color structures or gradients within a galaxy? It is a rather disappointing situation that metallicity effects in the light of galaxies can very well be masked and confused with differing age effects in the stellar population mix and by the influence of any dust-component reddening that may be present (O'Connell 1986). Searching for a metal abundance-luminosity relationship requires looking for a non-degenerate calibrated measure of metallicity that is relatively insensitive to the changes in the mix of young and old stellar populations caused by ongoing star formation in the spiral arms of disks, a measure that is far less attenuated than optical observations to redder wavelengths by any dust component in the galaxy's structure, and is *sensitive* to any variation in mean stellar metallicity. The near-infrared color indexes (H-K), (J-H), and specifically (J-K) may measure up to this challenge.

What general color behavior might one expect of late-type face-on spirals? Often visual band plates of spirals suggest, and cause the perception, that the outer parts are bluer and the bulges are redder (Peletier & Balcells 1996), but is this entirely true as a function of radius? Since higher metallicity often leads to redder colors, to what extent, range, and population does any color behavior occur? This has often lead to the assumed idea that the inner galaxy has higher metallicity than the outer disk because of its redder color (de Jong 1996). What three factors could contribute to such reddening color behavior?

- Various mixes of stellar populations can cause color gradients. A mix with an older percentage of stars will produce redder integrated colors. Younger populations are bluer. A radial gradient in the age mix of stars will be reflected in the colors (Worthey 1994, Vazdekis et al. 1996, Charlot & Bruzual 1991).

- Metallicity gradients will produce a reddening of color with increasing abundance of metals. Metals are the primary electron donors in the outer envelopes of stars and hence the opacity. This combination controls the stellar radius and as a consequence the surface temperature and color (Bothun et al. 1984).

- If in spirals the concentration of dust density decreases as a function of increasing distance from the spiral bulge this will also produce a reddening of color inward into the galaxy (de Jong 1996, Peletier et al. 1994, Peletier & Balcells 1996).

It has long been established that Near-Infrared (NIR) wavelengths, longward of $1\mu m$, emphasize the older and more stable stellar population of K & M giants and dwarfs in the integrated light of spiral galaxies (Rauscher 1995, Thuan 1983). The more numerous older stellar component is a much better measure of the overall mean metallicity in stellar populations within spiral galaxies rather than the sparse young and massive stars that dominate the optical bands which reveal only the very recent star formation history. Since galaxies are dominated by the number of the old stellar component the NIR is hopefully sampling the largest population and thus gaining the largest average metallicity behavior of the galaxy. The NIR colors may provide a great tool to measure the mean effective surface temperatures of the K & M giant branch and dwarfs. Surface temperatures are sensitive to metallicity abundances, lower metallicity stars produce higher effective temperatures (bluer) while higher abundances of metals cause a greater percentage of the star's energy to radiate away at longer wavelengths causing lower (redder) surface temperatures.

3. Thesis Goals

The principal goals of this thesis are:

- Treat Galactic Halo Planetary Nebulae as a distinct group of objects and consistently model their abundances using photoionization models.
- Establish any trends within halo planetary nebula chemistry and any comparisons and/or similarities with galactic disk and bulge PNe.
- Investigate the physics and implications behind using more physical representations for the white dwarf central star's spectrum upon the modeling of planetary nebula abundances. Essentially, is there is any justifiable reason to prefer more rigorous stellar atmosphere assumptions other than that of a simple blackbody radiator?
- Probe the efficacy of using near-infrared colors of a handful of face-on Virgo Cluster grand-design spiral galaxies as a means to map stellar metallicity in spiral disks. Establish whether the J-K color can be used as an abundance

probe while remaining insensitive to the changes in the stellar age population mix and reddening from dust.

- Deconvolve the luminosity profiles of the spiral galaxies in all three J, H, & K passbands to derive estimates of their respective bulge/disk masses and luminosities. Explore whether any conclusions can be drawn from the galaxy's basic physical parameters.

- Discuss the general structure of the spiral galaxy's near-infrared magnitude profiles.

- Use the NIR to derive new physical parameters of the individual galaxy's bulge/disk mass and luminosity and compare to previous results in a hope to test the quantitative agreement.

- Establish whether there is measure of consistent NIR color gradients present in any structures of the sample of face-on spiral galaxies and whether any strong linkage can be made to abundance gradients from HII region data on the same studied galaxies.

Chapter 2

Planetary Nebulae: Halo & Disk

1. Halo Planetary Nebulae Introduction

Planetary nebulae form during the asymptotic giant branch evolutionary stage of medium mass stars experiencing helium shell flashes around their carbon cores. These flashes effectively eject most of the outer envelope of the star, leaving behind a hot post-stellar object at the core and an extended nebula containing some of the nucleosynthetic products of the progenitor star's evolution. An analysis of abundances in the nebula can provide constraints on the mixing, dredge-up, and nuclear processes that occurred during the evolution of the progenitor star, as well as information regarding the chemical enrichment processes affecting the abundances of the interstellar medium.

Halo planetary nebulae (HPNe) form an important and distinctive group of metal deficient systems within the galaxy. HPNe not only provide the opportunity to study evolution of individual metal-poor stars, but in addition, because the progenitor star's original content of elements such as neon, argon, sulfur and perhaps oxygen is unaltered during evolution, they also serve as probes of halo metallicity at the time of their formation (Torres-Peimbert & Peimbert 1979).

Halo or Type IV planetary nebulae are characterized by their height above the galactic plane, their kinematic characteristics, and/or their low metallicity relative to disk planetary nebulae. Specifically, $|z| > 0.8kpc$, $|\Delta V_{pr}| > 60km/s$, and

$log(O/H)+12 < 8.1$, where $|z|$ is the distance away from the galactic plane (Peimbert 1990) and $|\Delta V_{pr}|$ is the peculiar radial velocity relative to the galactic rotation curve at the object's galactocentric distance. Basic physical data for the known HPNe are provided in Table 2.1. Column (1) gives the object name followed by its PK. Catalog number in column (2), while additional names are listed in Column (3). In columns (4) through (8) I provide nebular diameter, radial velocity, distance, apparent visual magnitude, and logarithmic extinction for each object. The final column gives references from which the information on each HPN was obtained.

Halo Planetary Nebulae Physical Data.

Object (1)	Pk. No. (2)	Other Names (3)	$R('')$ (4)	$V(km/s)$ (5)	$d(kpc)$ (6)	m_V (7)	$C(H\beta)$ (8)	Ref[1] (9)
K648	65−27.1	Ps-1	1.0	−141	10	14.9	0.08	6,12,13,15
DdDm-1	61+41.1		0.5	−304	17	15.6	0.0	5,11
PN006-41.9	6−41.9	PRMG-1	8.4	—	7	17.0	0.15	3
NGC2242	170−15.1		22	30	6	15.0	0.16	7,8
NGC4361	292+43.1		81	30	1.2	13.2	0.10	8,9
M2-29	4−03.1		3.6	−103	4	17.7	0.97	1,2,14
BB-1	108−76.1	BoBn-1	3.0	196	10.8	—	0.23	1,15
H4-1	49+88.1		2.7	−14.1	—	19.5	—	10,15
PN243.8-37.1	243.8−37.1		23	—	5.0	15.6	0.09	10
GJJC-1	9.8−07.5		4	−15.3	3.1	14.3	0.53	4

Table 2.1: [1]References: 1. Peña et al. (1991), 2. and 3. Peña et al. (1989) 4. Gillett et al. (1989), Cohen & Gillett (1989) 5. Clegg et al. (1987) 6. Adams et al. (1984) 7. Shaw & Bidelman (1987), Maheara et al. (1987) 8. Torres-Peimbert et al. (1990) 9. Mendez et al. (1988) 10. Peña et al. (1990), Barker (1980), Torres-Peimbert et al. (1979) 11. Dolidze & Dzhimselejshvili (1966) 12. O'Dell et al. (1964) 13. Peimbert (1973) 14. Boeshaar & Bond (1977) 15. Barker (1983).

K648 is the proto-type HPN often used as a comparison to other planetary nebulae and has been studied by numerous authors including Pease (1928), O'Dell (1964), Peimbert (1973), Miller (1969), Adams et al. (1984), and Henry, Kwitter, & Howard (1996). DdDm-1 was discovered by Dolidze and Dzhimshelejshvili (1966) and has been analyzed by Barker and Cudworth (1984) and Clegg et al. (1987). Papers have been presented on NGC2242 by Huchra (1984), Maheara et al. (1986,1987), Shaw and Bidelman (1987). Garnett and Dinerstein (1988,1989) and Torres-Peimbert et al. (1990), while NGC4361 has been analyzed by Aller et al. (1978), Adam and Köppen (1985), and Torres-Peimbert et al. (1990). PN243.8-37.1 and PN006-41.9 were recently discovered and analyzed by Peña et al. (1989,1990). M2-29 is located toward the galactic center and has been studied by Webster (1988), Acker et al. (1989), and Peña and Torres-Peimbert (1991). Papers on BB-1 include Barker (1980), Torres-Peimbert et al. (1981), and Kwitter & Henry (1996). H4-1 was discovered by Haro (1951) and studied by Hawley and Miller (1978), Torres-Peimbert and Peimbert (1979), and Henry et al. (1996). Finally, GJJC-1 was discovered and identified by Gillett et al. (1989) and analyzed by Cohen & Gillett (1989). Speculations about GJJC-1 do not appear in this work because the observations were not adaptable to this study.

The primary goal of this chapter is to use published spectral line intensities to model nine halo planetary nebulae, using detailed photoionization analysis techniques. In doing so a homogeneous set of abundances and physical characteristics by employing a consistent modeling procedure for each object can be derived. The results are then compared with similar available data for disk PNe. In the end it is hoped that an inference about the chemical properties of each nebula as well as chemical evolution differences and similarities between the disk and halo of the galaxy can be discussed.

Most planetary nebula models treat the central star as a simple blackbody radiator. This is a good first approximation, but perhaps not a very physical one, because there are many complex processes occuring in the atmosphere which can influence the formation of spectral lines. On the other hand, more detailed model stellar atmospheres which treat non-LTE and non-grey effects as well as stellar winds are now available in the literature. Thus, in §4 a probe of different central star models was done to test the relevence of atmosphere grids published by Kurucz (1991).

Husfield and Kudritzki (1984), Werner (1991), and Clegg and Middlemass (1987), where the last set of models includes the dynamical properties of stellar atmospheres in the central white dwarf star.

The modeling process and model results for each HPN are discussed in §2. In §3 I present a discussion of inferred abundances and stellar properties followed by a detailed comparison of stellar atmosphere grids is presented in §4. Finally, §5 contains a summary of conclusions for this chapter.

2. Halo Planetary Nebulae: Theoretical Models

Detailed photoionization models have been computed for the nine HPNe described in §1, using the photoionization code CLOUDY (Ferland 1990; Baldwin et al. 1991) and employing published emission line strengths as constraints. The calculation proceeds by stepping outward through the nebula from the central star and determining both an ionization and temperature balance at each point. The latter is done by equating the heating and cooling rates from all ions and grains at each location. The program includes effects of charge exchange as well as radiative and dielectric recombination processes.

2.1. Input Parameters and Assumptions

The principal input parameters are the stellar effective temperature, gas density, and abundances of fourteen elements: H, He, C, N, O, Ne, Na, Mg, Al, Si, S, Ar, Ca, Fe, and Ni. During the calculation, the geometry of the nebula was assumed to be spherical, of constant density, and to be dynamically expanding outwards from the central star. The filling factor was either taken directly from the observations or assumed to be 0.1. The starting radius of the model, i.e. the distance from the star to the inner surface of the nebula, was also taken from previous observational determinations when possible. If there were no previous estimates, these parameters were treated as free parameters and were varied until the spectral line intensities were well matched.

The calculation produces the line strengths of hundreds of emission features for many ions as output. These are then compared to the observations, and if necessary, the calculation is repeated with altered input parameters until a reasonable match between model and observations is achieved.

Blackbody form for all of the input stellar spectra has been adopted. This choice is justified by calculating models of each of the nine HPNe fluxes from four different grids of detailed atmosphere calculations. The results of this study are presented in §4, where it is shown that current observational data cannot discriminate between blackbody and other theoretical atmospheric input fluxes. Thus, the discussions to follow refer only to results using blackbody ionizing spectra as input to the photoionization models.

2.2. Results

The resultant model calculations for each HPN are shown in Tables 2.2a and 2.2b, where the first two columns contain the wavelength and associated ion emission lines used in the analysis. Observed line strengths taken from the references in column (9) of Table 2.1 are listed in the columns labeled "observed," while the columns labeled "model" show the resulting line intensities produced by the best model. Line strengths in Tables 2.2a to 2.2c have been scaled to a system where the strength of $H\beta = 100$. Included in the lower panel of each table are electron temperatures and densities from both previous studies and the theoretical models.

Abundance ratios inferred from the models are given in Table 2.3, where He/H and O/H values are expressed in $log(x) + 12$ form, while the remaining ratios are presented as $log(x)$, where x is one of the ratios in the heading. The last column gives the input stellar effective temperature. For purposes of comparison, the solar and disk PN values are provided in the last two rows of the table (Grevesse & Anders 1989; Peimbert 1990).

Finally, Table 2.4 presents a comparison of abundances, stellar temperatures, and nebular densities with previously published values whose sources are given in the bottom row. Note that the derived abundances, although reasonably consistent with earlier published results, show some variation, especially in the cases of argon and neon. Discrepancies between the results particularly for Ne and Ar may arise because the model analysis is more tightly constrained than previous studies, and thus forced to adopt slightly different abundances to satisfy these constraints. Specifically, in the case of argon, not only was their an attempt to match [ArIII] λ7135, but also [ArIV] λ4740 and [ArV] λ7006. Also, including and matching such lines as [NeV] λ2424 [NII] λ1750, and NIV] λ1485 tended to produce differing abundance results for the same elements when compared to previous results that did not match all of these lines. The disagreement between some of the previously published electron densities and the modeled electron densities is most likely a result of the paucity of observed sulphur lines. Specifically, for PN006-41.9, NGC4361, and PN243.8-37.1 the density is an unconstrained parameter because of the lack of any good [SII] observations for these HPNe. But density is indirectly constrained in that certain densities produce poor fits to the data.

The accuracy of the derived abundances depends on the uncertainties of the observed line intensities, the accuracy of the measured atomic transition rates for the elements and their ions, and simply from how much the abundances could be varied within the photoionization models to still obtain a reasonably well fit model to the observations. An estimate of the overall uncertainty is 0.1 - 0.25 dex for C, N, and O, and 0.2-0.3 dex for Ar, Ne, and S.

Table 2.2a. Line Intensities.

Object Wavelength	Ion	K648 Observed	K648 Model	DdDm-1 Observed	DdDm-1 Model	PN006-41.9 Observed	PN006-41.9 Model
5876	He I	13.0	13.2	14.1	14.6	11.0	11.5
1640	He II	...	0.45	...	0.45	...	77.5
4686	He II	<1.0	0.05	...	0.05	13.0	8.17
4267	C II	<1.0	0.29	<0.13	0.01	...	0.00
1909	C III]	640.0	637.3	...	0.53	...	36.4
1549	C IV	...	21.9	...	0.53	...	1481.9
4658	C IV	...	0.0	...	0.0	...	0.01
6548	[N II]	1.70	1.28	...	16.2	...	0.62
6584	[N II]	3.90	3.83	53.7	48.5	<3.00	1.85
1750	[N II]	...	2.26	...	7.77	...	14.2
1485	N IV]	...	0.04	...	0.08	...	361.2
1240	N V	...	0.0	...	0.0	...	113.3
3727	[O II]	26.0	26.1	112.0	107.7	0.40	0.78
4363	[O III]	2.70	2.72	4.57	4.45	28.6	24.5
5007	[O III]	210.0	208.4	417.0	439.9	1119.8	1081.7
4959	[O III]	70.0	69.5	144.0	146.6	407.0	360.6
3869	[Ne III]	11.1	11.0	29.0	29.7	107.0	104.4
3968	[Ne III]	2.5	3.40	24.0	9.1	34.0	32.0
4720	[Ne IV]	...	0.0	...	0.0	...	0.20
2424	[Ne IV]	...	0.0	...	0.0	...	6.64
7135	[Ar III]	0.20	0.21	7.60	7.58	3.00	0.19
4740	[Ar IV]	...	0.03	<0.24	0.33	12.9	12.7
7006	[Ar V]	...	0.0	...	0.0	...	0.16
6716	[S II]	...	0.82	3.00	3.20	...	0.21
6725	[S II][1]	<2.00	1.75	...	1.20	<3.00	0.49
6731	[S II]	...	0.93	5.20	4.93	...	0.28
9069	[S III]	...	13.1	...	36.9	...	1.15
9532	[S III]	...	34.1	...	96.1	...	3.01
Temp.							
T(O+)		10,600 K	13,000 K		11,900 K		14,100 K
T(O++)		12,500 K	12,700 K	11,800 K	11,400 K	15,000 K	16,000 K
Ne		1700	999	4400	2938	750	1936

[1] Blended combination of $[SII]\lambda 6716 + [SII]\lambda 6731$

Table 2.2b. Line Intensities.

Object Wavelength	Ion	NGC2242 Observed	NGC2242 Model	NGC4361 Observed	NGC4361 Model	M2-29 Observed	M2-29 Model
5876	He I	< 1.50	1.48	<0.60	0.57	14.3	14.9
1640	He II	812.0	881.9	812.0	794.6	...	15.1
4686	He II	107.0	92.5	110.0	84.2	1.40	1.59
4267	C II	...	0.01	0.48	0.01	...	0.02
1909	C III]	316.0	260.6	218.0	284.4	...	231.1
1549	C IV	2340.0	2499.9	2630.0	2364.3	...	89.1
4658	C IV	...	0.05	1.30	0.04	...	0.01
6548	[N II]	...	0.06	...	0.09	5.90	5.81
6584	[N II]	<3.00	0.19	<0.80	0.27	17.0	17.4
1750	[N II]	30.0	11.3	<63.0	15.0	...	29.3
1485	N IV]	117.0	110.7	...	119.4	...	6.80
1240	N V	100.0	109.5	<63.0	70.6	...	0.00
3727	[O II]	<2.00	0.91	<1.40	1.12	34.0	32.9
4363	[O III]	5.40	6.25	6.00	7.07	15.0	11.0
5007	[O III]	200.0	183.7	204.0	220.2	452.0	482.4
4959	[O III]	66.0	61.4	68.0	73.4	149.0	160.8
3869	[Ne III]	16.0	20.8	19.0	21.3	58.0	55.7
3968	[Ne III]	19.0	6 40	20.0	6.53	32.4	17.1
4720	[Ne IV]	2.00	6.78	2.20	4.42	...	0.01
2424	[Ne IV]	323.0	207.9	234.0	142.8	...	0.24
7135	[Ar III]	3.80	0.50	2.00	0.60	9.20	9.37
4740	[Ar IV]	6.90	6.61	6.40	6.58	...	4.67
7006	[Ar V]	6.30	4.08	5.00	2.92	...	0.00
6716	[S II]	...	0.06	...	0.14	1.38	1.44
6725	[S II][1]	...	0.10	...	0.25	...	3.38
6731	[S II]	...	0.04	...	0.11	2.00	1.95
9069	[S III]	...	1.01	...	2.63	...	9.35
9532	[S III]	...	2.63	...	6.84	...	24.4
Temp.							
T(O+)		20,400 K		19,700 K		14,300 K	
T(O++)		17,600 K	20,300 K	19,300 K	19,700 K	9900 K[2]	
Ne		1400	1191	1500	1200	3000	2111

[1] Blended combination of$[SII]\lambda6716 + [SII]\lambda6731$

[2] Peña 1996. Recent HST observations.

Table 2.2c. Line Intensities.

Object Wavelength	Ion	BB-1 Observed	BB-1 Model	H4-1 Observed	H4-1 Model	PN243.8-37.1 Observed	PN243.8-37.1 Model
5876	He I	...	14.2	15.4	14.5	1.70	1.23
1640	He II	245.5	311.5	...	103.9	776.0	732.4
4686	He II	25.7	15.9	10.4	11.0	104.7	76.8
4267	C II	1.10	0.39	...	0.12	...	0.0
1909	C III]	1585.0	1189.0	484.0	535.7	<100.0	33.6
1549	C IV	2089.0	1896.6	144.0	128.1	<117.0	182.2
4658	C IV	...	0.71	...	0.0	...	0.0
6548	[N II]	9.80	11.7	35.9	37.6	...	0.19
6584	[N II]	30.9	35.2	<116.0	112.9	...	0.56
1750	[N II]	44.7	30.6	...	31.8	32.4	34.8
1485	N IV]	...	30.8	...	5.72	< 141.0	170.3
1240	N V	64.6	4.13	...	0.08	<158.0	33.6
3727	[O II]	13.2	11.2	247.0	200.5	1.70	1.64
4363	[O III]	5.60	5.16	12.9	12.9	13.2	18.4
5007	[O III]	...	0.30	669.0	722.8	562.3	496.2
4959	[O III]	109.6	117.2	213.0	240.9	199.5	165.2
3869	[Ne III]	166.0	167.5	8.30	8.19	75.9	78.1
3968	[Ne III]	67.6	51.4	...	2.51	34.7	24.0
4720	[Ne IV]	...	0.30	...	0.01	...	8.99
2424	[Ne IV]	...	17.0	...	0.25	...	240.2
7135	[Ar III]	0.30	0.23	1.05	1.40	..	1.16
4740	[Ar IV]	0.50	0.47	...	0.37	7.40	8.40
7006	[Ar V]	...	0.03	...	0.01	...	1.49
6716	[S II]	0.00	0.11	0.68	0.74	...	0.57
6725	[S II][1]	...	0.28	...	1.46	...	1.61
6731	[S II]	0.10	0.17	0.71	0.72	...	1.04
9069	[S III]	...	0.63	...	1.12	...	33.5
9532	[S III]	...	1.66	...	2.94	...	87.3
Temp.							
T(O+)			12,700 K		13,000 K		21,300 K
T(O++)		14,500 K	13,200 K	11,700 K	14,400 K	19,000 K	21,300 K
Ne		3000	2903	1000	669	1000	6274

[1] Blended combination of $[SII]\lambda6716 + [SII]\lambda6731$

Model Abundances & Central Star Temperatures

Object	He/H	O/H	C/O	N/O	Ne/O	Ar/O	S/O	$T_*(10^3$K)
K648	10.96	7.61	0.89	−0.89	−1.04	−3.89	−1.50	45.6
DdDm-1	10.98	8.12	−0.92	−0.53	−0.92	−2.35	−1.52	45.6
PN006-41.9	10.96	8.06	−0.06	0.12	−0.83	−2.56	−1.06	102.3
NGC2242	10.99	8.19	−0.34	−0.91	−0.77	−2.67	−2.19	137.0
NGC4361	11.00	8.15	−0.26	−0.80	−0.90	−2.75	−1.85	121.2
M2-29	10.97	7.71	−0.16	−0.45	−0.77	−2.05	−1.78	73.3
BB-1	11.05	7.83	1.12	0.17	−0.11	−3.33	−2.33	125.0
H4-1	11.06	8.09	0.11	−0.45	−1.82	−3.17	−3.04	112.5
PN243.8-37.1	11.00	8.10	−1.50	−0.60	−0.74	−2.57	< −1.10	99.7
Sun	11.00	8.90	−0.20	−0.90	−0.80	−2.30	−1.70	
<Disk PN>	11.04	8.70	0.00	−0.55	−0.60	−2.10	—	

Table 2.3: Derived abundances for best fit models using a blackbody as the central star's radiation field.

Table 2.4. Comparisons: Abundances, Stellar Temp., & Nebular Densities.

	K648		DdDm-1		PN006-41.9	
	Current	Other	Current	Other	Current	Other
He	10.98	11.02	10.95	11.00	10.94	10.96
C	8.42	8.73	7.23	7.23	8.08	—
N	6.63	6.50	7.45	7.40	8.00	—
O	7.56	7.67	8.03	8.15	8.62	8.10
Ne	6.50	6.70	7.08	7.30	7.23	7.50
S	5.86	—	6.36	6.53	5.49	—
Ar	4.12	—	5.72	5.86	7.00	5.80
$T_*(10^3K)$	43.9	40.0	44.7	38.0	80.6	75.0
$Log N_e(cm^{-3})$	3.0	3.2	3.8	3.6	3.4	2.7
Ref[1]		A		B,D		H
	NGC2242		NGC4361		M2-29	
He	10.46	11.00	10.15	11.00	11.07	10.97
C	8.06	8.40	8.09	8.10	7.58	—
N	7.59	7.65	7.06	7.30	7.27	7.17
O	7.63	8.05	7.70	7.85	7.80	7.31
Ne	6.74	7.80	6.83	7.55	7.08	6.72
S	6.30	6.30	6.30	6.20	5.86	5.91
Ar	5.58	5.90	5.51	5.80	5.93	5.26
$T_*(10^3K)$	124.8	80.0	96.6	80.0	183.3	50.0
$Log N_e(cm^{-3})$	3.6	3.2	3.4	3.5	3.6	3.5
Ref[1]		E		E		C
	BB-1		H4-1		PN243.8-37.1	
He	11.03	11.02	11.12	10.99	10.32	11.00
C	8.95	9.16	8.08	9.29	6.78	7.60
N	7.81	7.89	7.52	7.87	7.45	8.00
O	7.82	7.68	8.03	8.50	7.66	8.40
Ne	7.71	7.76	6.24	6.80	6.97	7.90
S	5.47	5.80	4.89	5.90	<6.90	—
Ar	4.57	4.74	4.99	5.20	5.26	6.20
$T_*(10^3K)$	125.0	—	127.9	—	90.0	90.0
$Log N_e(cm^{-3})$	3.6	3.5	—	—	3.6	3.0
Ref[1]		C		F		G

[1]A: S. Adams et al. (1984), B: T.Barker & Cudworth (1994), C: M. Peña et al. (1991), D: R.E.S. Clegg et al. (1987), E: Torres-Peimbert et al. (1990), F: Torres-Peimbert (1979), G: M. Peña et al. (1990), H: M. Peña et al. (1989).

3. Discussion

Interpreting abundance results such as those presented here is complicated by the presence of several known factors which influence the levels of those elements. For example, an element's abundance in a planetary nebula is due not only to the amount present in the stellar progenitor at the time of its birth, but also to any nucleosynthetic process within the star which either enhances or destroys certain amounts of that element. Figures 2.1a - 2.1e show plots of five abundance ratios versus log(O/H)+12 for our nine HPNe as derived from our models. All abundance ratios are normalized to solar values (Grevesse & Anders 1989). Each HPN is denoted by a unique symbol while a group of disk PNe, studied by Aller and Czyzak (1983), are all denoted as a plus mark. A few general trends can be seen. First, O/H is clearly subsolar in all nine objects, a trend which is very consistent with the idea that these PNe formed in the halo out of metal-poor material. The size of the deficiency, i.e. a factor of 10 or so, is typical of what is found in the halo.

In Fig. 2.1a, we see that most of the objects exhibit carbon enrichment relative to the solar values. This seems especially true for K648 and BB-1. However, the opposite effect is seen for DdDm-1 and PN 243.8-37.1, where carbon has not enriched the nebula. This might be explained if DdDm-1 experienced fewer dredge-up episodes than K648 and BB-1, thus leaving DdDm-1 and PN 243.8-37.1 with less carbon enrichment (Clegg & Middlemass 1987). Nitrogen shows much the same behavior relative to solar values as shown in Fig. 2.1b, i.e. all objects except K648 and NGC2242 exhibit nitrogen enrichment.

Of course, one must also consider effects of oxygen depletion on the C/O and N/O ratios. Simply, the presence of less oxygen requires less carbon or nitrogen to be mixed out into the (eventual) nebular material to inflate the C/O and N/O ratios. [For example, the more oxygen-rich the progenitor star is, the more difficult it is to

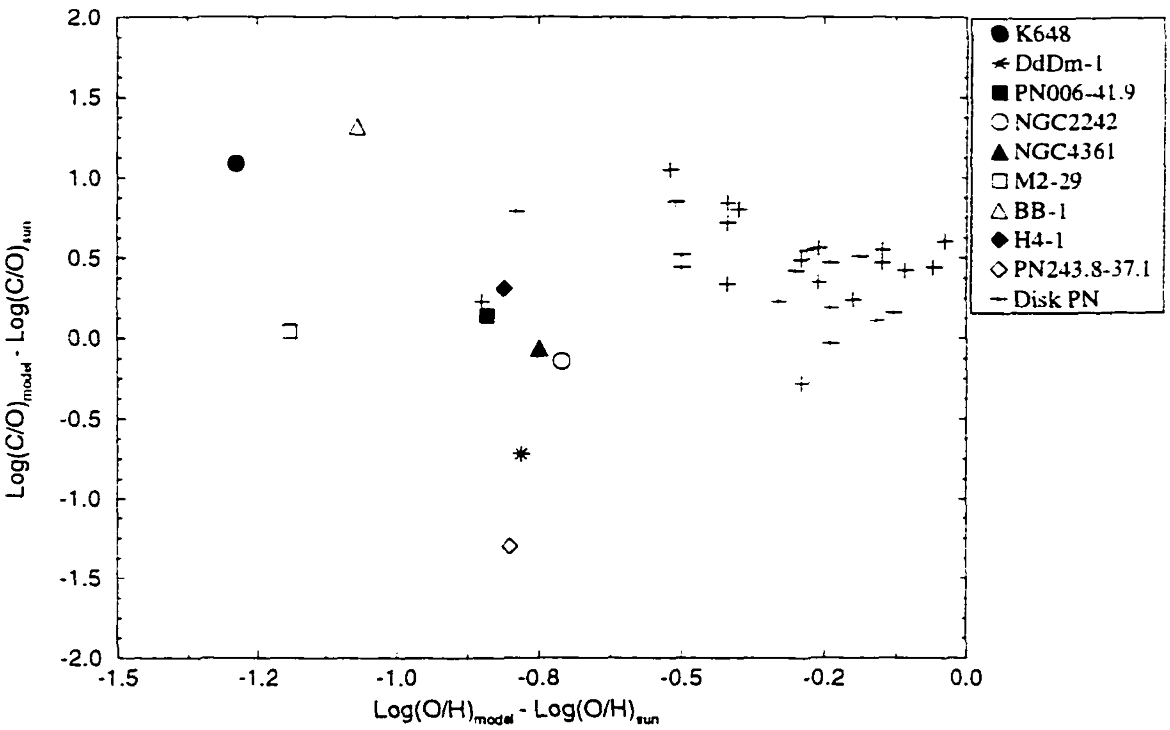

Fig. 2.1a.— Plot of Log(C/O) vs. Log(O/H)+12. Each HPN is denoted by a unique symbol while a group of disk PNe are shown as plus marks. The legend for this figure is valid for all figures.

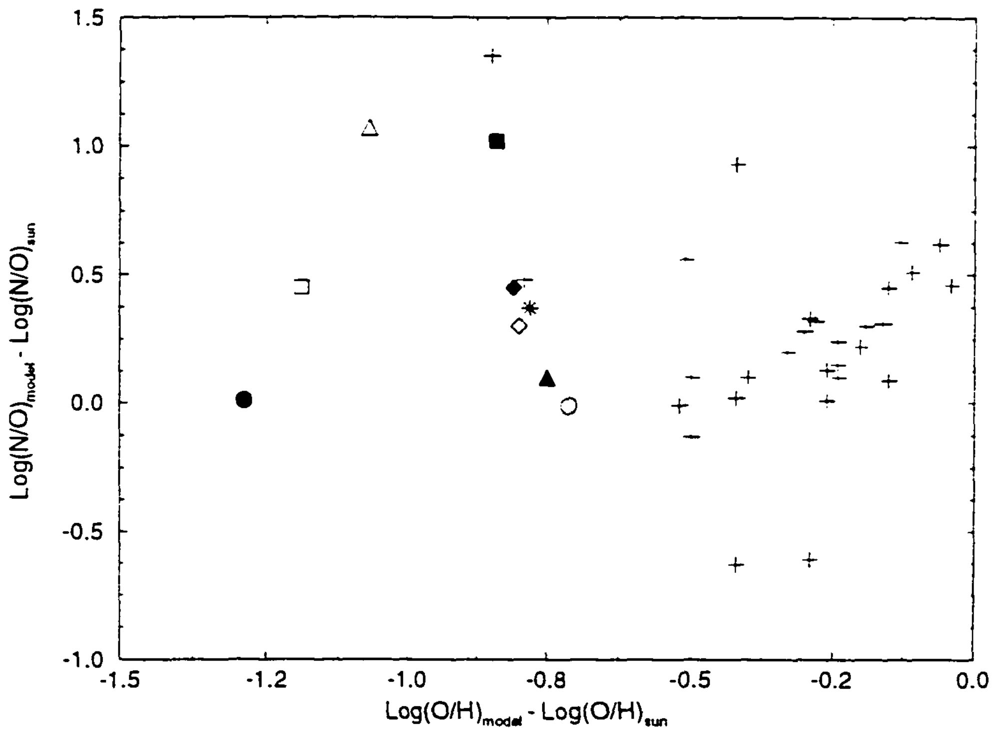

Fig. 2.1b.— Same as Fig. 2.1a but for N/O.

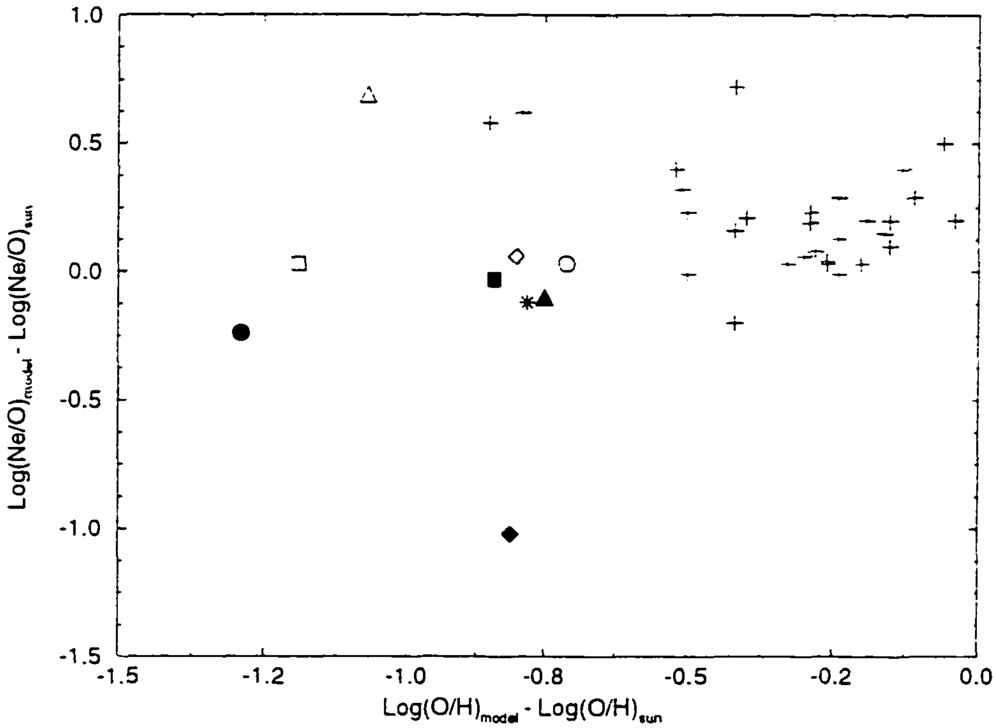

Fig. 2.1c.— Same as Fig. 2.1a but for Ne/O.

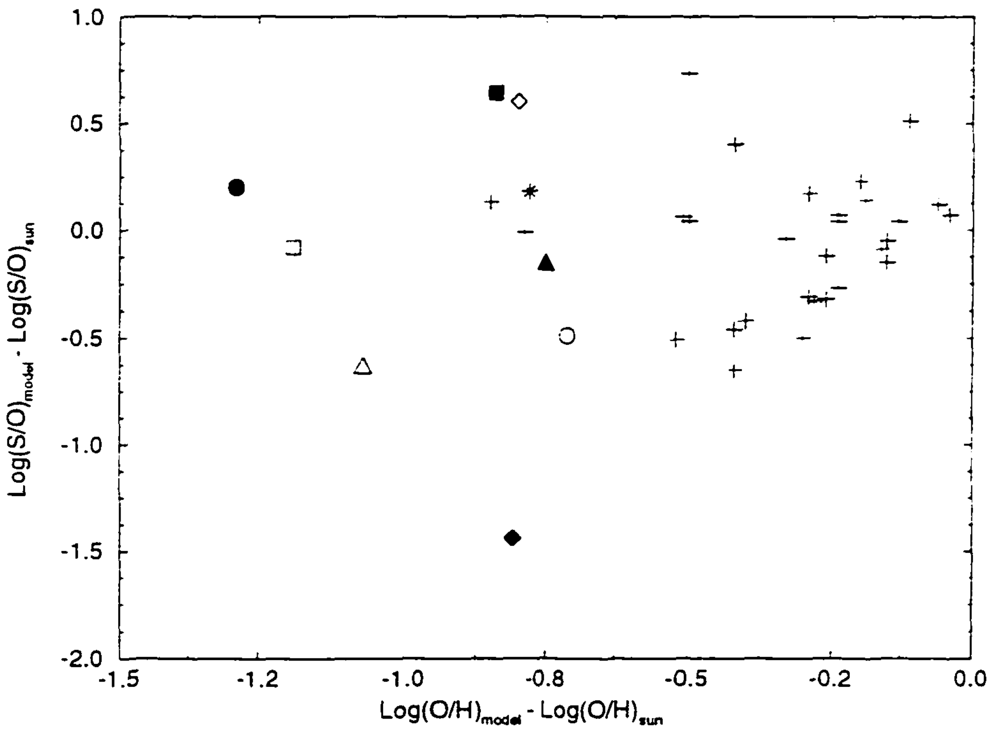

Fig. 2.1d.— Same as Fig. 2.1a but for S/O.

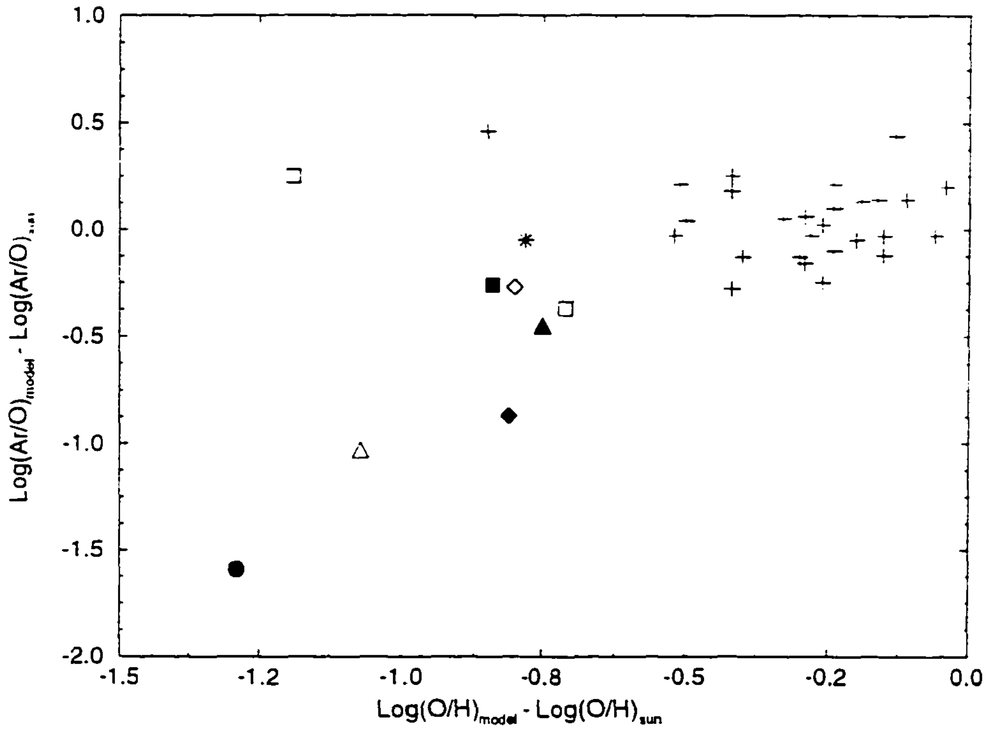

Fig. 2.1e.— Same as Fig. 2.1a but for Ar/O.

turn it into a carbon star (Boothroyd & Sackmann 1988).] If oxygen depletion were the principal factor in elevating observed C/O and N/O, then we would expect to see an inverse relation between C and N, and O in Figs. 2.1a and 2.1b The absence of such a relation suggests that true enhancement is taking place.

The low carbon abundance apparent in DdDm-1 and PN243.8-37.1 may set the low end for mixing and dredged-up carbon enrichment (Iben 1983, Iben & Renzini 1983). It has been suggested (Clegg & Middlemass 1987) that the progenitor of DdDm-1 was a star of low mass. Thus, fewer thermal pulses occurred before PN formation (Clegg & Middlemass 1987), and less carbon was dredged up.

Results for Ne/O, S/O, and Ar/O are shown in Figs. 2.1c, 2.1d, and 2.1e, respectively. Ne/O in Fig. 2.1c is roughly consistent with the solar value for all but two HPNe. Relative to the solar value, BB-1 shows a high Ne/O ratio while H4-1's ratio is low. All other objects are within 0.2 dex of the solar value. For S/O in Fig. 2.1d we note that the spread in values for halo and disk PNe is nearly the same; for the HPNe, excepting H4-1, the spread is symmetric about the solar value. In Fig. 2.1e we see that most of the HPNe have values of Ar/O below the solar value.

Figs. 2.1 suggest the HPNe are significantly enriched with C and N but show a spread in Ne/O, S/O, and Ar/O which is larger than can be explained by uncertainties. The bulk of the carbon present in presumably comes from nucleosynthetic processes experienced by the progenitor star prior to producing a planetary nebula. During hydrogen burning in the CN cycle, carbon is depleted as nitrogen is produced but later produced by helium burning. The key is getting this carbon to the stellar surface and more importantly from there to the planetary nebula. In HPNe the amount of carbon in the nebula can supply constraints to thermal pulse mechanisms, mixing, and dredge-up processes. (Renzini et al. 1981). Thus, K648 and BB-1 may set the upper limit of carbon yield for successful dredge-up.

In contrast to the enrichment expected for C and N during the lifetime of a PN progenitor star, ratios of Ne/O, S/O, and Ar/O should reflect the conditions at the time of progenitor birth[1]

Fig. 2.1c shows that Ne/O is roughly constant among HPNe, a finding consistent with that of Henry (1989) for a large sample of planetary nebulae. This finding implies both that Ne and O are produced by stars within the same mass range, and furthermore, in most HPNe studied here, nucleosynthesis in the stellar progenitors did not alter the star's inherited amounts of these two elements. On the other hand, H4-1 and BB-1 do not follow this behavior at all. Ne/O for H4-1's is subsolar while it exceeds the solar level in BB-1. This might imply different original neon abundances for the progenitor stars. It is interesting to note that the average disk value for Ne/O is higher than the average value for the HPNe. This would suggest that the extra neon in the disk stars is coming from an additional source and/or mechanism which is unimportant in the halo, or that the neon produced by stars in the halo is not sufficiently mixed and enhanced in the interstellar medium of the halo. Alternatively, the younger and slightly more massive progenitor stars of PNe in the disk may destroy oxygen in extra ON cycling.

With respect to Ar/O in Fig. 2.1d, there seems to be two groups. H4-1, K648, and BB-1 all show very low argon abundances compared to the others, i.e. Ar/O< -3.0, a finding noted by Peña et al. (1991). Also it seems that those objects with extremely low Ar/O show some of the highest carbon enrichment relative to solar values of C/O. This is especially true for K648 and BB-1.

Finally, note that results in Figures 2.1 show a relatively large amount of scatter in abundances for the halo objects when compared with the disk PNe. This is particularly interesting in the cases of Ne/O and Ar/O (Figs. 2.1c and 2.1d,

[1]Processes which could ostensibly change these ratios include the production of ^{22}Ne from ^{14}N and/or the destruction of ^{16}O in the ON cycle.

respectively), since, as already mentioned, these ratios are expected to be constant among all PNe, assuming that the halo and disk systems are each homogeneous when stars form within them. Note that the scatter observed in HPNe is qualitatively similar to what is seen by Gilroy et al. (1988) in their analysis of 20 metal poor Population II stars as well as Cowan et al. (1996). Interestingly, Searle and Zinn (1978) have suggested halo formation models which include the accretion of extragalactic material into the primordial halo material. Such a process might produce HPNe which would reflect the differing abundances of the halo material.

4. The Atmospheres of Planetary Nebula Central Stars

Planetary nebula central stars have hot atmospheres that are highly non-grey and where non-LTE effects may be very important. In the case of local thermodynamic equilibrium, there is no reason to assume that we may apply the equilibrium relations of thermodynamics and statistical mechanics for local temperature and density to all portions of the atmosphere of these AGB stars. The radiative processes producing the star's continuum depend directly upon the structure of the star's radiation field, and thus equilibrium equations apply only if the radiation is isotropic and has a Planck distribution. Indeed a much different situation exists in the outer observable layers of the star. Radiation flows freely from the stellar surface to empty space, the radiation field has an absolute intensity, direction, and frequency distribution, and the atmosphere has a large temperature gradient. Thus the radiation field is very non-local and anisotropic in nature (Mihalas 1978).

Several grids of detailed model atmospheres are available in the literature, and we consider if observed nebular properties are extensive and sensitive enough to allow a choice to be made among them and blackbodies as the proper ionizing source for each of the HPNe. Thus, various stellar continuum models were experimented with to test blackbodies and four different model atmosphere grids by using predicted fluxes as ionizing sources to compute individual best-fit models of each of the nine HPNe in the sample. The four grids tested were an LTE grid (Kurucz 1991). plus three different non-LTE grids (Werner & Heber 1991; Clegg & Middlemass 1987; and Husfield & Kudritzki 1984).

Kurucz (1991) produced a set of LTE. line blanketed. static plane-parallel stellar atmospheres which spans temperatures $3,500K$ to $50,000K$ and $log(g)$ 0.0 to 5.0. These models include up-to-date line opacities. continuous opacities. and an approximate treatment of convective overshooting. The models are computed for solar abundances and cover an effective range in spectral type from K to O stars. I employed model atmospheres from the upper temperature range of the grid. i.e. 35,000K to 50,000K in our tests.

The grid of Werner & Heber (1991) spans temperatures of $80,000K$ to $200,000K$ and $log(g)$ 5.0 to 8.0. All the models assume solar abundances. include H and He line opacities. and use a detailed treatment of model atoms for C, N, and O within the atmosphere. Werner & Heber note that CNO line blanketing greatly affects both the temperature structure of the star and level populations of atoms within the atmosphere. as both are governed by the non-local behavior of the NLTE radiation field produced.

Clegg and Middlemass (1987) produced a hot non-LTE model atmosphere grid with H and He opacity sources spanning temperatures of $40,000K$ to $180,000K$, $log(g)$ 4.0 to 8.0, and He/H of 0.10 to 0.01 by number. The models include H line blanketing, except for stars with $T_{eff} > 10^5K$. The spread in T_{eff} and $log(g)$ was based on Schönberner's (1981, 1983) evolutionary tracks for planetary nebula central stars. The plane parallel models are in radiative equilibrium. and H^o, He^o, and He^+ depart from LTE by 5, 5. and 6 levels, respectively. Bound-free and six bound-bound transitions were included for H^o, and bound-free transitions were included for He^o and He^+.

Finally, Husfield and Kudritzki (1984) calculated a small grid of models which spans $50,000K$ to $115,000K$ and $log(g)$ 3.8 to 5.75. These models are non-LTE, static, plane parallel, and are in hydrostatic and radiative equilibrium, with a chemical composition of Y=n(helium)/n(hydrogen)=0.1 and solar CNO. The models use the complete linearization technique developed by Auer and Mihalas (1969, 1970) with details described by Kudritzki (1976).

Using fluxes from each of the four grids of model atmospheres, An attempt to match the observed line strengths for each of the nine HPNe was undertaken.

Fig. 2.2 plots the log of the ratio of predicted to observed line strengths for seven important lines. Individual HPNe are uniquely represented by a symbol shape defined in the legend. For any one line strength, symbols correspond from left to right to blackbody, Kurucz or Werner, Husfield-Kudritzki, and Clegg-Middlemass, respectively. (The order is explicitly shown for the line C III] λ1909.) A few ratios of observed to predicted line strengths were not plotted because the observed line was very uncertain and differed markedly from the predicted line intensity in the model. Notice there is close agreement between model and observation for these representative lines, with exceptions in the cases of [NII] λ6584 and [OII] λ3727 for PN006-41.9. Line intensity discrepancies for [NII] λ6584 may be due to de-blending problems with the observations since [NII] λ6584 is very near Hα (Torres-Peimbert et al. 1990), while the discrepancy for [OII] λ3727 may be a symptom of poor signal to noise due to the line's weakness. Clearly, the results indicate that observed line strengths are suitably compatable with all four model atmosphere grids as well as blackbody continuum shapes adopted in the earlier sections.

Figures 2.3a and 2.3b show differences in inferred abundances and central star temperatures derived for each model. Fig. 2.3a plots the log of the best fit abundances derived using each type of stellar continuum normalized to the analogous results for blackbody input spectra. For any one model atmosphere along the horizontal

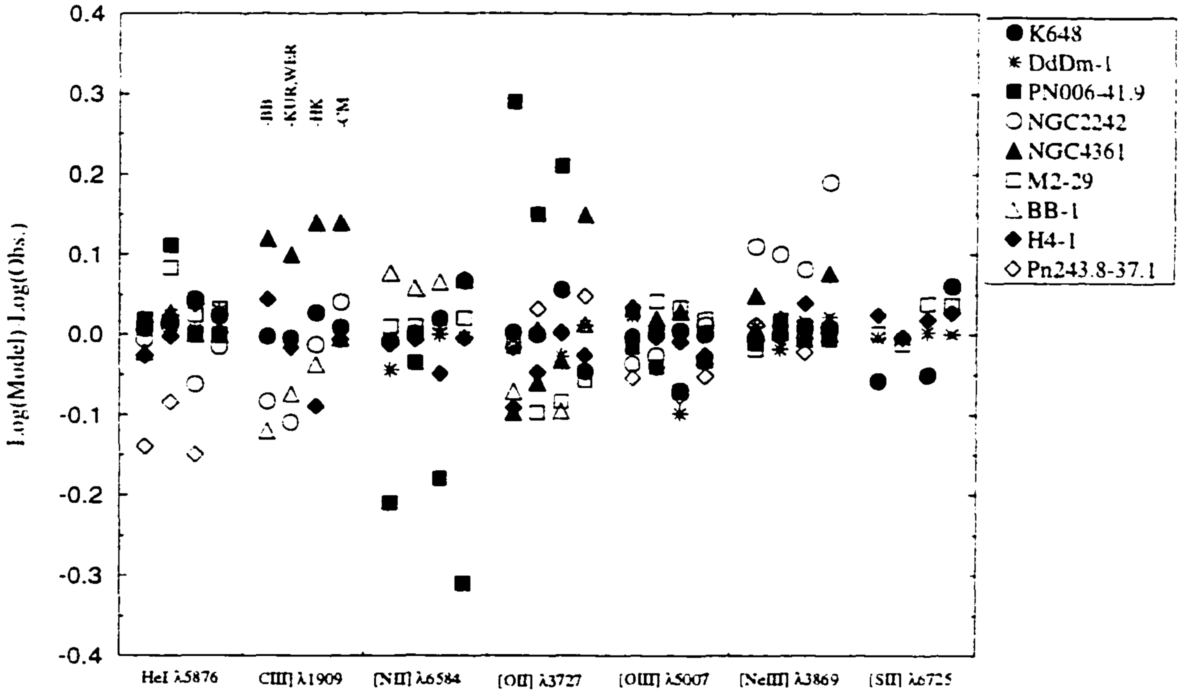

Fig. 2.2.— Plot of a sample of theoretically produced line strengths compared to the observations. For any one line strength, symbols correspond from left to right, blackbody, Kurucz or Werner, Husfield-Kudritzki, and Clegg-Middlemass, respectively. Individual HPNe are uniquely represented by the symbols in the legend.

scale, the unique symbol for each HPN indicates, from left to right, the difference in carbon, nitrogen, and oxygen abundances used in the two photoionization models incorporating the model atmosphere and blackbody. The points plotted reflect only the results that fell within the span of stellar temperature for the theoretical atmosphere grids for the specific modeled HPNe. Taken together, the abundances implied when using the stellar atmosphere models for the central star compared to those associated with blackbodies generally are lower.

Figure 2.3b shows the difference in inferred effective temperature between the model atmosphere and blackbody. For most models, a lower stellar temperature, compared to blackbody, was necessary, perhaps due to the influence of line blanketing in the model atmospheres. The flux produced by the star is conserved, so the flux blocked by forming lines must emerge at other frequencies, thus altering the emergent continuum of the star (Mihalas 1978). Line blanketing, or the blocking effect, caused by the presence of heavier elements in the atmosphere effectively cools the surface layers of the star. Blackbody models will therefore tend to imply higher effective temperatures of central stars.

The set of Kurucz LTE models (Kurucz 1991) compared to blackbody tend to lead to slightly lower derived oxygen abundance, higher nitrogen abundance, and cooler central star temperatures. In the case of carbon for K648 and DdDm-1 the Kurucz models imply a lower carbon abundance for carbon rich K648, and yielded a higher estimate of carbon abundance for carbon poor DdDm-1. LTE model lines in the central star are dependent on the local temperature and density of the line producing region, thus the emergent continuum that later illuminates the nebula will reflect the same local behavior. How the carbon heating and cooling is treated in the outer layers of the star via LTE equilibrium approximations may influence likewise the later carbon abundance results in the nebula.

The set of Husfield - Kudritzki models (Husfield & Kudritzki 1984) compared to

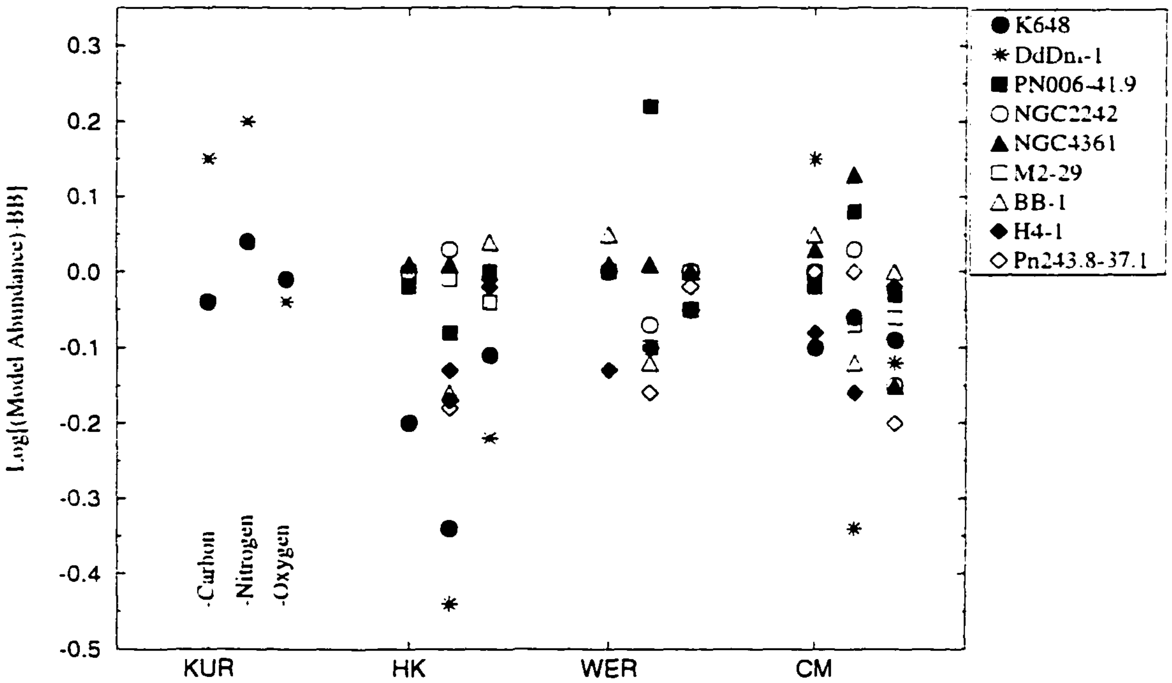

Fig. 2.3a.— Plot of the log input abundance of C, N, & O for each of the atmospheric models compared to blackbody results.

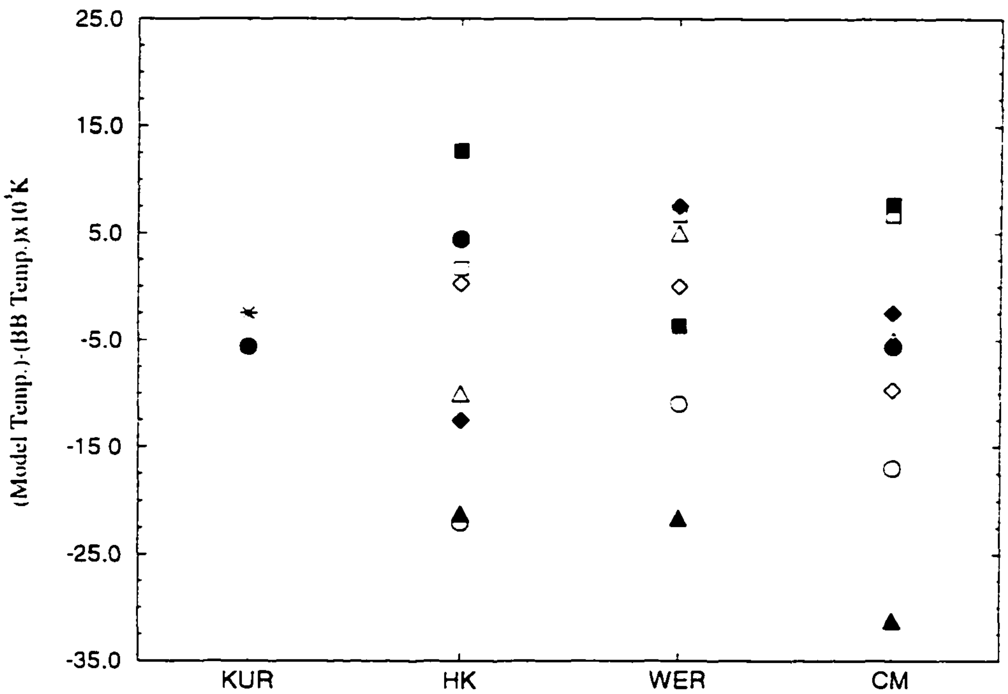

Fig. 2.3b.— Plot of the stellar atmospheric model temperatures used for the central star compared to the blackbody results.

blackbody resulted in smaller to the same carbon and nitrogen abundances. Only NGC2242 and BB-1 using these models resulted in slightly increasing nitrogen and oxygen abundances significantly. As for oxygen, the Husfield - Kudritzki models yielded nearly the same abundance for the PN's with hot cores, and lower abundances for the PN's with cooler central stars. These differences may be the result of the NLTE radiations field's non-local dependence on temperature and density. The hotter stars, as opposed to the cooler, may include more high ionization lines that cause the star's emergent flux to be redistributed to frequencies which oxygen is more sensitive.

Werner's stellar atmosphere models (Werner & Heber 1991) when compared to the blackbody models resulted in mostly cooler central stellar components for the PN's and only significantly influenced nitrogen in abundance. BB-1 and PN243.8-37.1 had lower nitrogen abundances with these models. In fact, the Werner set of models tended to stray the least in abundance and temperature results to those same results under a blackbody model.

Finally, Clegg - Middlemass (Clegg & Middlemass 1987) models when compared to the blackbody counterpart lead to lower PN central star temperature, higher carbon abundance for carbon poor DdDm-1, lower carbon abundance for carbon richer K648 and H4-1, generally lower oxygen abundance, and the same to slightly lower nitrogen abundances. Only DdDm-1 showed much lower nitrogen abundance when compared to the nitrogen abundance derived using a blackbody.

Because of the relatively close agreement on derived abundances and stellar temperatures between model atmopsheres and blackbody, no particular input spectrum in obviously preferable given available constraints. Thus for purposes of simplicity, blackbody spectra have been consistently adopted as input for the models presented in the earlier sections of this chapter.

5. Halo Planetary Nebulae Conclusions

Theoretical photoionization models have been calculated for the nine HPNe and compared to observations because of their distinctive metal poor chemical abundances and their potential contribution to understanding stellar nucleosynthesis as well as galactic chemical evolution. For the most part, elemental abundances are found which are relatively consistent with past results for these objects in the literature.

Specifically, results show that, relative to the sun, all nine objects show subsolar O/H, most show enhanced C/O (except DdDm-1 and Pn243.8-37.1) and N/O (except NGC2242 and K648), and seven of the nine HPNe show a relatively constant value for Ne/O. Interestingly, Ar/O hints at possibly two differing groups within the nine HPNe, those that are extremely Ar poor (H4-1, K648, and BB-1) and those which are not. All trends are reasonably consistent with nucleosynthesis ideas relevant to intermediate-mass stars.

In §4 the effects upon nebular spectra of various assumptions regarding the properties of the atmospheres of central stars were considered. The results show that nebular emission line strengths are relatively insensitive to atmospheric details. Therefore, blackbodies are currently quite suitable representatives of a central star continuum.

Finally, in comparing the model results of HPNe to a sample of disk PNe there is shown that abundances at the time of progenitor formation appear to have been less homogeneous in the halo than in the disk. Specifically, there is more abundance scatter for halo than disk PNe, consistent with recent findings for halo and disk stars. This suggests a more complete mixing of material in the disk of the galaxy and is qualitatively consistent with halo formation theories involving the accretion of material with differing chemical abundances.

Chapter 3

IR Imaging of Virgo Spiral Galaxies.

1. Introduction

Much research has addressed the question of abundance gradients across the disks of spiral galaxies using HII region emission spectra to measure gas phase abundances. Little is known, outside the Milky Way, about possible gradients in mean stellar metal abundance. However, Near-Infrared (NIR) observations may provide a golden opportunity to probe the metallicities in the largest stellar content within spiral galaxies, the old K and M giants and dwarfs that by number and stellar mass dominate the spiral galaxy, and compare the stellar abundances to abundance information already observered for the galaxy interstellar gas component. The advantages of the NIR wavelength range are the relative independence from extinction and the fact that the light in the NIR arises from the old stellar population which greatly dominates the galactic stellar mass (Charlot & Bruzual 1991, Worthey 1994). So the use of NIR may more easily avoid any confusion dust may cause in the determination of galaxy color structures, as well as probe the dominating stellar mass of the galactic structures. The basic hypothesis of this research is: is it possible to identify and calibrate any correlation that may exist between the NIR colors of a spiral galaxy's stellar content, especially (J-K), and the gaseous HII region abundances in its respective interstellar medium as a first step to using NIR colors as probes of mean stellar metallicity? There are a number of reasons to find a measure of mean stellar abundance distribution in the bulges and disks of extragalactic spiral galaxies.

HII regions can not be used to determine abundances where there is not much gas or many large OB stars. Abundance information is important in understanding some spirals which have had most of their gaseous component stripped away. i.e. such as in rich clusters where effects of the environment may have stripped away a spiral galaxy's gas phase and greatly altered its chemical evolution (Skillman et al. 1996. Whitmore 1990. Haynes 1990. Sarazin 1988). Indeed, finding a calibrating measure of stellar metallicity is direly needed where a gaseous component is not present. Stellar metallicity data can be important to many current theories and observations about extragalactic chemo-evolutionary processes.

One can probe the connections between abundance ratios of gas and stars in the galaxy. The chemical evolution histories of star formation and processes occurring to influence the interstellar medium such as stripping, inflow, supernovae rates, and stellar abundance yields could provide invaluable information. Spiral galaxies are known to have radial metallicity gradients in their current gas content (Skillman et al. 1996). These gradients have been directly modeled using observed spectra of HII regions contained in the spiral arms of the galaxies and a knowledge of the photoionization processes going on in the gaseous mix (Henry & Howard 1995, Vila-Costas & Edmunds 1992). The origin of these gradients is still very much under study and remain unclear. However, various chemical models can empirically reproduce the gradients by various combinations of radial variations in star formation rates, gas fraction concentration, radial flows of gas, initial mass functions and evolutionary stellar yields, and accummulations of unprocessed gas relative to the star formation rate (Pagel 1989, Phillips & Edmunds 1991, Güsten & Mezger 1982, Diaz & Tosi 1984, Pitts & Tayler 1989). It would seem likely that the stars that currently form from the interstellar medium would also likely have some similar metallicity gradient. Since the Near-Infrared (NIR) is expected to be dominated by the older stellar population of stars residing in the galaxy, it would make a wonderful calibrating measure to compare the current metallicity content in the gas of a galaxy to the stellar metallicity of the old population of stars. One could provide ideas about the form, speed, and extent of enrichment that has taken place since the currently living old stellar component and young stellar component formed. Almost all closed box chemo-evolutionary models predict the current gas content of a galaxy to be more enriched than that of the stellar component, but where and how this enrichment takes place is a very convoluted problem (Tinsley 1980). Understanding the actual stellar metallicity abundances and any structural dependencies can shed light on what must be done to untangle the chemical evolution puzzle as supernovae, inflow, and stripping occur to provide the current gas metallicities and any gradients that might exist.

Possible information about where stars form could be investigated. Stars may preferentially form in galactic regions of enhanced metal abundance. In fact, the stars might then have higher abundances than the gas because of a forming bias (Romanishin 1990). If the above is true, being able to measure the current metallicity in the older stellar population would help find any spatial-metallicity effects present in the structure of spiral galaxies. Many galaxy formation and evolution models predict stellar metallicity gradients. As the stars live and die, slowly enriching the material they are contained in, they may also be changing the preferred time and place they form later stellar generations. This chemical fingerprint could be left locked in the functional form of abundance in the older stellar population.

Infall of intergalactic gas will continually dilute the galaxy's interstellar medium altering the enrichment ratio of the disk gas. A comparison of the old stars to current metallicity can constrain the amount and strength of infall. The metallicity behaviors observed for the stellar content of a galaxy will depend on the type and homogeniety of infall (Güsten & Mezger 1982, Diaz & Tosi 1984). Understanding the chemical mixture and differences between the stars that dominate the structures of a galaxy and the gaseous content which rule the current star formation will yield better models and explanations of the complex processes that push the holistic evolution of a galaxy and how its galactic environment may contribute.

It is possible to actually map individual spiral arms along the spiral disk and get very local (J-K) color information and thus possibly very local metallicity. The (J-K) color techniques may be the only way to study stellar abundances in some galaxies, especially those with varying degrees of HI deficiency. It would be worthwhile to probe the various structures within a galaxy and the influences of the old stellar population within the galaxy. Is there any difference in the metallicities of the old stellar population between the bulge and disk? Is there any degree of metal variation along a spiral arm radially outward, or across an arm? Might there be any abundance differences between arms and intra-arms? These are the questions that might be answerable *if* this NIR technique proves fruitful.

The primary objective of this study is to measure a handful of Virgo cluster spiral galaxies which span a large range in HI deficiency in the J (1.2μ), H (1.6μ), and K($2.2\ \mu$) bands, and to attempt to establish a link between any color gradient associated with the stellar component of a galaxy to the gas content abundances and their respective gradients. The Virgo cluster is preferable for this undertaking because of its relative closeness to our own galaxy, its rich array of spiral galaxies, and its high galactic latitude. All of these benefits help further reduce any problems that might arise from extinction. The spiral galaxies chosen represent a wide range of gas content for comparison purposes. The spirals range from normal gas content to a deficiency of a factor of 10 compared to field galaxies of the same type. The list of spirals includes galaxies clearly deficient in HI (NGC4689 and NGC4571), to intermediate objects (NGC4254 and NGC4321), and to a galaxy located on the outskirts of the cluster exhibiting apparently normal HI distributions (NGC4303) (Warmels 1988,Cayatte et al. 1990). Previous HII region studies have been carried out on all these galaxies (Henry et al. 1994, Skillman et al. 1996). This portion of the thesis will attempt to identify and calibrate any correlation that exists between the NIR colors, especially (J-K), and HII region abundances as a first step to using NIR colors as probes of mean stellar metallicity. As part of this study physical and dynamical properties that might help lead to a further understanding of the galaxy's structure will also be determined. Finally, all of the information will be compared to previous results and stellar population models to further test the search for a useful measure of stellar abundance.

Table 3.1 summarizes the properties of the Virgo galaxies chosen. The table lists projected separation from M87, radial velocity, RSA and RC3 types (de Vaucouleurs et al. 1991), luminosity, rotation velocity, optical diameter as is defined in the RC3 catalog, HI deficiency relative to field spiral galaxies of the same type as defined by Cayatte et al. (1994), and the effective galactic radius derived from the photometry of Kodaira et al. (1986). M87 is a giant elliptical galaxy that dominates the Virgo cluster galaxies and provides a tremendous portion of the entire cluster's gravitational potential well. Figure 3.1 shows the local spatial distribution of the galaxies under study relative to M87 in the Virgo Cluster.

The Virgo Cluster is in itself an important structure to explore because of its approximate 2000 member galaxies wh:. .ı dominates our intergalactic neighborhood, it represents the physical center of our local supercluster (Coma-Virgo Supercluster), and influences all the galaxies and galaxy groups by the gravitational attraction of its enormous mass.

1.1. N4321

NGC4321 (M100) is the brightest and possibly the largest spiral galaxy in the Virgo cluster (Sandage 1961) and has been extensively observed. Giant blue stars dominate the spiral arms and highlight recent star formation that may be from density perturbations caused by interactions with neighboring cluster galaxies.

The distribution of the HII regions within the galaxy has been studied by Anderson et al. (1980) while the chemical compositions of several HII regions and any disk abundance gradients they may imply have been explored by Henry et al. (1994), Skillman et al. (1996), and Vila-Costas & Edmunds (1992). Guhathakurta et al. (1988) have obtained rotation curves. NGC4321 is often used, as well as the other galaxies in this sample, to explore the environmental effects of the cluster upon HI distribution and the chemical compositions of cluster galaxies as compared to field galaxies (Henry et al. 1992). Finally, Arsenault et al. (1988) find good evidence for a bar and an Hα ring highlighting enhanced star formation within the structures of NGC4321.

1.2. N4303

NGC4303 (M61) was discovered by Oriani on May 5, 1779 when following the comet of that year, 6 days before Charles Messier's discovery. NGC4303 is a late-type barred spiral classified as SAB(rs)bc and is also one of the largest spiral galaxies in the Virgo scluster. The galaxy has numerous giant HII regions positioned along its spiral arms (Hodge & Kennicutt 1983) which makes it an attractive object to study chemically. The galaxy is located in the outskirts of the cluster, seems to have HI amounts typical of a normal field galaxy, and is undergoing a prodigous burst of star formation (Kennicutt 1989, Martin & Roy 1992) with a rate of $14 M_{\odot}/yr$ (Kennicutt 1983). In this regard, the galaxy has a high observed rate of supernovae, SN1926A, 1961I, & 1964F. Supernova 1961I appeared in the spiral arms about 82" from the center (Barbon et al. 1989). Cayatte et al. (1990) note that NGC4303 could be weakly interacting with two nearby neighbors.

1.3. N4571

NGC4571 was one of the discoveries of William Herschel. The galaxy has a high peculiar motion toward the local group, as it is receding from us with only 298 km/sec, compared to the cluster's overall 1100 km/sec (Binggeli et al. 1987). NGC4571 is a moderate-luminosity spiral classified as SBc II with a correspondingly lower disk surface brightness (van den Bergh et al. 1990). NGC4571 is thought to be located very near M87 and the core of the Virgo cluster because it shows significant signs of HI stripping (Cayatte et al. 1990)

The galaxy has a sufficiently low disk luminosity that individual stars can be resolved (Sandage & Bedke 1988) and the disk contains a number of observed of Cepheids (Pierce et al 1992). Most recently researchers at Canada France Hawaii Telescope (CFHT) used observations of these Cepheid variable stars to determine estimates of the Hubble flow constant (Pierce et al 1992).

1.4. N4689

NGC4689 is another moderate luminosity spiral much like NGC4571. There is a great paucity of previous detailed observations of this Virgo member. Skillman et al. (1996) and Vila-Costas & Edmunds (1992) have HII region chemical abundances and have inferred a fairly shallow gradient from the few HII regions that can be observed. Devereux et al. (1987) has integrated H band observations of the inner 250pc of the bulge.

1.5. N4254

NGC4254 was the second galaxy to be recognized as a spiral by Lord Rosse in 1848. NGC4254 (M99) is classified as an Sa(s)c type galaxy and is unusually asymmetric, which may be due to recent encounters with other members of the cluster (Rauscher 1995). The galaxy is undergoing large scale and vigorous star formation

(Keel 1983, Rauscher 1995). Three supernovae have been recorded in NGC4254, 1967H and 1972Q both type II, and 1986I a type I supernova (Henry et al. 1994).

The spiral arms of the galaxy show great flocculence and evidence of large dust lanes cutting across the arms. The southern arm shows much more evidence of star formation than the less defined northern arm (Keel 1983).

2. Near-IR Observations

All NIR observations in J, H, and K were obtained during an April 1993 observing run at Kitt Peak National Observatory (KPNO) by Dr. William Romanishin, using the NOAO Simultaneous Quad-color Infrared Imaging Device (SQIID) on the 1.3m telescope. The field of view was ~5.5 arcmin with an image scale of 1.366 arcsec/pixel (at H). Cold dichroics allow the four separate detectors within SQIID to image the infrared J, H, & K windows simultaneously. Each detector is a Hughes 256 × 256 hybrid platinum silicide Schotty barrier diode array with 30μ pixels. Dark current is less than 2 e/sec, read noise is roughly 60 electrons, and well capacity is a million electrons. Quantum efficiency is about 6.6% at J, 5.5% at H, and 3.4% at K. Each channel is solely optimized specifically over a very narrow bandpass so the instrument has high throughput and any ghosting is thoroughly minimized. The SQIID detector area, overall stability, adequate quantum efficiency, signal to noise capability, and dark signal contraints combine to make the detector a great tool for simultaneous full-field observation of J, H, and K[1]. Further details of the SQIID camera are discussed by Ellis et al. 1992.

[1]Unfortunately, the SQIID device is no longer in operation at KPNO and is no longer able to be used further.

Table 3.1. Virgo Cluster Spiral Galaxy Properties

Name	R_{M87}[1]	Velocity[2]	Type[3]	T-Type[4]	L_B[5]	V_c[6]	D_o[7]	R_E[8]	HI_d[9]
NGC4254	$3^\circ.7$	2354	Sc(s)	5	42	307	5.6	0.87	0.17
NGC4303	8.2	1486	Sc(s)	4	43	216	6.5	1.11	0.08
NGC4321	4.0	1540	Sc(s)	4	47	201	7.6	1.39	0.42
NGC4571	2.4	298	Sc(s)	6.5	9	165	3.7	0.87	0.44
NGC4689	4.6	1578	Sc(s)	4	13	185	4.4	1.11	0.75

[1]Projected distance from M87 in *degrees*.

[2]Radial velocity with respect to the Galactic center of rest from the RC3 in *km/s*.

[3]Morphological type from the RSA.

[4]Morphological type from the RC3.

[5]Blue luminosity in units of $10^9 L_\odot$ assuming all galaxies at the distance of 16.8 Mpc and using B_T^o from the RC3.

[6]Maximum rotation curve velocity in km/s from Warmels 1986.

[7]Corrected optical diameter Do from the RC3 in *arcmin*.

[8]Disk effective radius derived from the photometry of Kodaira et al. 1986 in *arcmin*.

[9]HI deficiency in dex as defined by Cayatte et al. 1994.

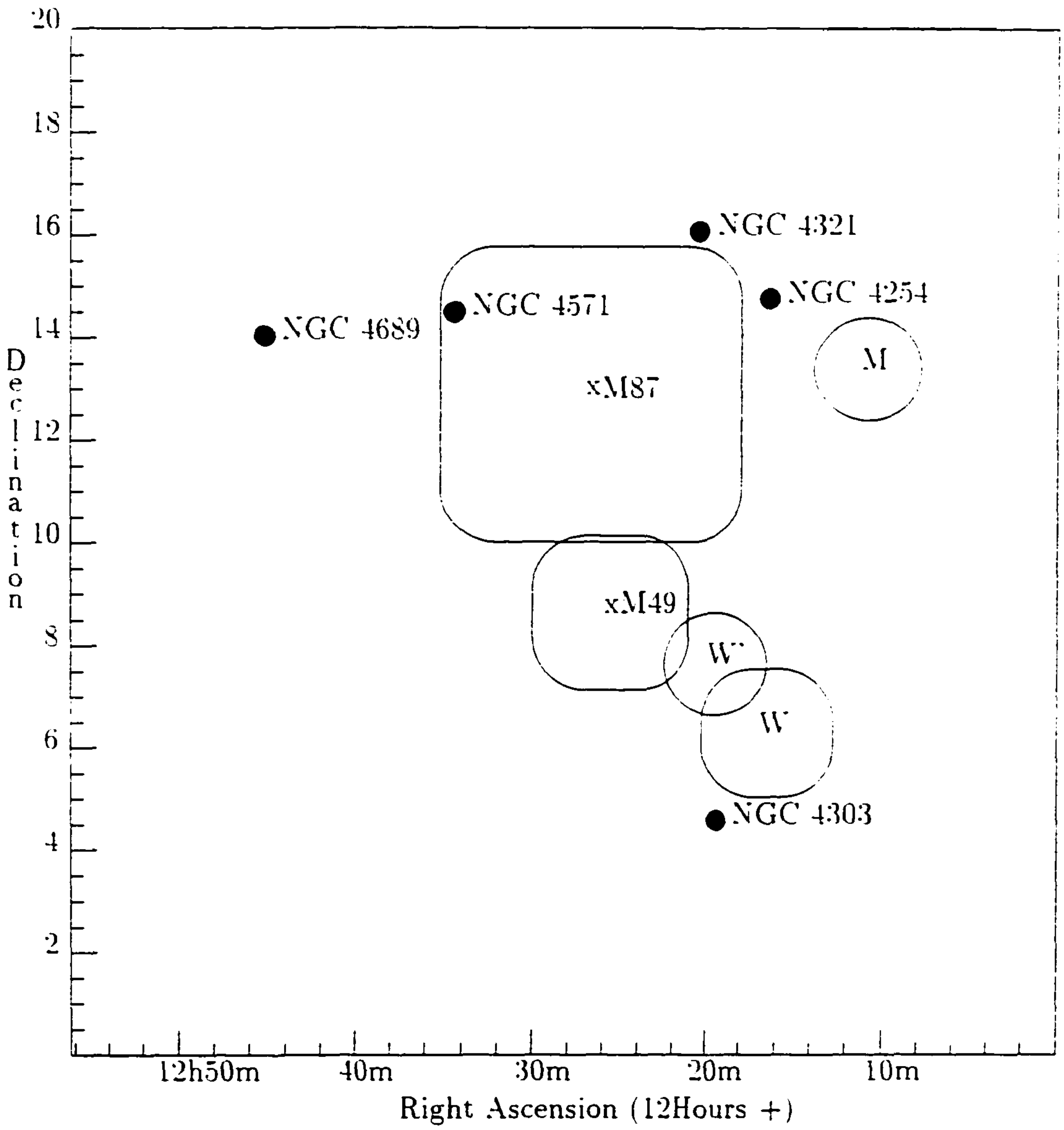

Fig. 3.1.— Map of the positions of the five Virgo spiral galaxies and the structures identified by Binggeli et. al. (1987). The points represent the galaxy positions with major groupings of galaxies within the Virgo cluster marked off by ovaled squares.

2.1. Dark Frames and Standard Stars

Proper data reduction requires accurate solutions for the small additive effects of internal illumination and charge generation from the SQIID device itself (Dark Frames) so as to remove any signal noise introduced to the object signal. The CCD chip will spontaneously emit electrons which are recorded along with the signal from the object light source. The instrument is cooled with liquid nitrogen to help reduce this signal noise. Since the SQIID dark current has both a base level and a time dependent component, a dark frame must be created for each detector for each exposure time. Dark images were taken with the shutter closed and the internal cold dark slide in place at the beginning and the end of each night. Exposure times of 5 seconds and 180 seconds were used in the creation of the dark frames. These are later used with the J,H, and K images to determine proper dark level subtraction. Since dark counts remained stable over a night's observing run, dark frames consisted of 9 images for each exposure per night.

At various times throughout each night, observations were made in each of J, H, & K of standard stars from a standard magnitude table of NIR stars by Elias et. al. (1982) so as to later calibrate the galaxy magnitude determination done during object image reduction. Each observation consisted of making images of the star at the center of the CCD. Multiple observations were made at different airmasses to be used for determining an atmospheric extinction/airmass slope when later converting pixel counts to actual magnitude values.

2.2. Object and Sky Offsets

Object and sky images were taken with equal exposure times of 180 seconds. At first the object or portion of the object image under study was centered on the CCD. The sky images were taken by offsetting the telescope from anywhere from 350 to 1000 arcsec. in a particular direction (N,S,E or W), to obtain relatively 'blank' background sky. The size and direction of the offset from the object was determined by examining the area near each object on the Palomar Observatory Sky Survey (POSS) plates to find a region relatively free of stars or galaxies. After a particular sky image was completed, the telescope was returned to the object galaxy for the next object image, although the object was not centered in the next image, but offset by 10-20 arcsec. either E/W or N/S. This dithering of the image was done to help battle signal lost by non-functioning pixels with each CCD image. This process was repeated until satisfactory object and sky images were obtained.

2.3. Relative Channel Alignment

An image of globular cluster M5 was taken during the observation run. A single 60 second exposure of the core of M5 provided enough information to map the coordinate transformation that was used to align (shift and rotate) the images from two of the IR channels (J,K) so they would overlay the image in the third channel (H) because each CCD is aligned slightly differently within the SQIID device. This process also brought each of the images to a common arcsec to pixel scale.

3. Image Preparation & Reduction Process

3.1. IRAF-SQIID Image Processing

All image reduction and analysis was done and performed by myself using the packages and tasks within the IRAF-SQIID package. The SQIID package is not an officially released nor supported IRAF package; further information on the SQIID package can be obtained from NOAO. The package and all necessary information can be obtained by anonymous ftp at mira.tuc.noao.edu and retrieving a tar file called 'sqiid.tar.' The discussion and processes that will be described are contained in the SQIID-IRAF package. The following procedures for each of the J,H, and K wavelengths is the same, thus the process below was simply repeated for each Near-IR passband.

3.2. Dark, Flat, and Sky Images

DARK frame reduction is accomplished with the IRAF-SQIID task 'sqdark.' The 'sqdark' task was used to combine 9 images of the internal cold dark slide from the beginning and end of each night into a single averaged dark image. This dark frame image was then used for that night's exposures to correct for small additive effects of internal instrument illumination and charge generation from the device's own heat and electrical noise. This was done for both 5 second and 180 second dark exposures.

Near-IR CCD observations are different from optical CCD observations in that dome flats are not really practical for the flatfielding of the former. Rather, by taking the median of a reasonable number of blank sky fields obtained at different times and different locations on the sky, a very precise and satisfactory measure of the detector flatfield can be calculated. Division by flat frame images take into account non-uniform responses to light by each pixel and uniformly normalizes the field of view the instrument records. The 'sqflat' task was used to make the flat frames.

Background illumination in the Near-IR is very unstable with time and location. In the Near-IR, J is very sensitive to cloud scattered moonlight while H and K can be greatly influenced by night sky emission and is variable with prevailing temperature and humidity. To combat this problem a sufficient number of observations were obtained to create sky frames for a proper calibration of these effects. Sky frames are established from observations with the same integration time and near in time and place to the objects, which provides an accurate measure of sky illumination during the individual source object observations. The sky signal, since the sky is between the instrument and object, must be removed from the object images. The sky frames for each object were made using the 'sqsky' task. This task combined the

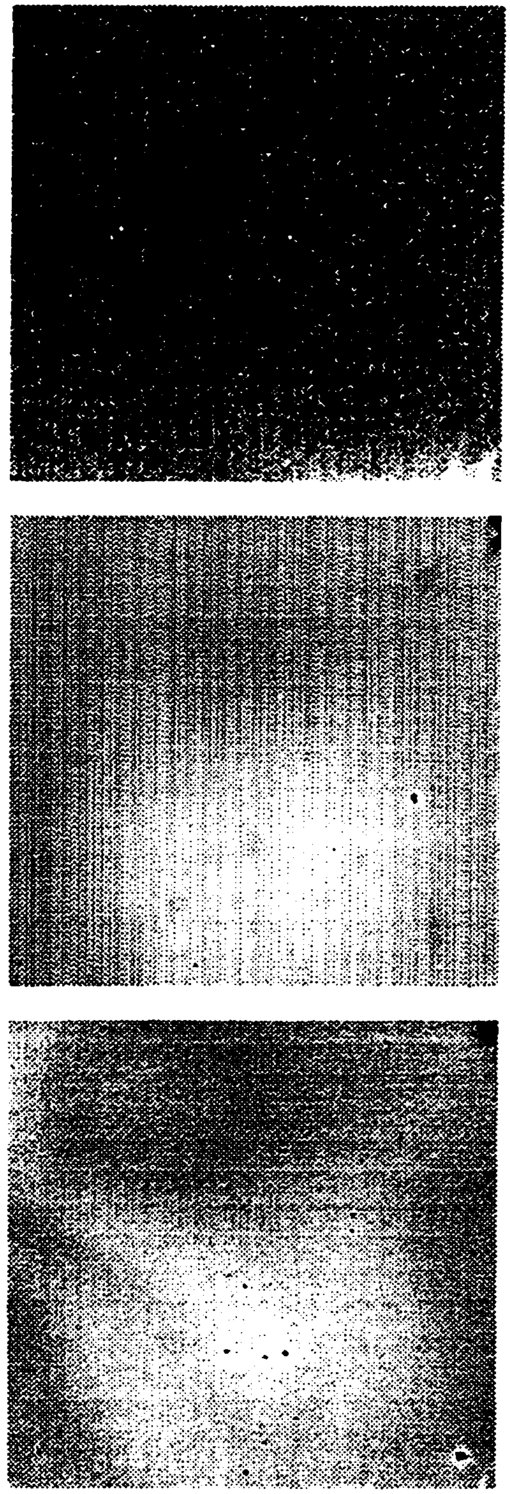

Fig. 3.2a.— Sample corrective image frames. Going top to bottom: dark, flat, and sky frames. Notice that the bad pixels are clearly evident in the sky frame before they are fixed.

sky images taken with each of the object images. This was repeated each night for each individual object.

So as to provide an idea of what these corrective images look like for future researchers, refer to figure 3.2a. The dark, flat, and sky frames shown are typical of types of signal corrections applied to produce more accurate source images.

3.3. Fixing Bad/Non-Functional Pixels

Bad pixels are simply damaged areas on a CCD. The iraf task 'fixpix' either used directly or within other SQIID-IRAF packages can interpolate small broken pixel areas. A separate bad pixel file, Table 3.2, was made for each color where the (x1,x2,y1,y2) CCD coordinates of bad pixels was tabulated. The coordinates x1 and x2 are the first and last columns of the bad region and y1 and y2 are the first and last lines of the bad region. The determination of bad pixels is done by visual inspection of an image in each of the colors. To highlight the bad areas on the CCD the pixel values that were originally greater than an arbitrary value $\sim$ -100.0, (good pixels), were set equal to zero. The good pixels would then all be the same color and the bad pixels would remain black in the resulting image. The (x1,x2,y1,y2) coordinates of the bad pixels could then be read off the image and stored into a file. The sky images are particularly suited to easily find the poor CCD pixels.

The 'fixpix' interpolation of bad pixels is calculated as follows:

- If the bad pixel region spans entire lines then the interpolation is from neighboring lines.
- If the bad region spans entire columns then the interpolation is from the neighboring columns.
- If the bad region contains more lines than columns then the interpolation is from neighboring columns.

- If the bad region contains the same or more columns than lines the interpolation is from neighboring lines.

- If the bad region borders the edge of the image then the interpolation is by replication of the first good pixel in the direction of interpolation and otherwise linear interpolation between the bordering lines or columns is used.

3.4. Producing Fully Processed Images

The first step in processing the many individual galaxy exposures in the individual J, H, and K channels can now proceed. This is done with the SQIID-IRAF 'sqproc' task. The order of the steps applied to the object images in this task is as follows:

1. Subtract the individual SKY images.

2. Normalize by the appropriate FLAT images.

3. Fix any bad pixels for each J, H, & K images.

4. Reorient the image(s) as required.

The DARK images were enabled and subtracted in the creation of the SKY image, so any dark current noise is removed when the SKY image is subtracted to remove any sky bias. The task 'sqproc' uses the raw exposures to create many individually processed J, H, & K object images for each galaxy.

Table 3.2. SQIID CCD Bad Pixels - H,J,K.

H Coordinates				J Coordinates				K Coordinates			
X_1	X_2	Y_1	Y_2	X_1	X_2	Y_1	Y_2	X_1	X_2	Y_1	Y_2
251	254	254	256	198	199	235	235	11	12	237	237
250	254	250	254	222	223	218	219	29	29	227	228
249	250	250	253	252	252	204	205	41	43	177	178
248	249	251	252	253	253	205	205	114	114	235	236
251	254	248	250	206	206	185	187	115	115	236	236
252	254	248	250	205	205	186	186	186	186	235	236
253	254	245	248	182	182	145	145	185	185	237	237
251	252	242	243	181	182	137	137	118	120	146	147
250	254	238	242	182	182	136	136	130	130	125	125
249	250	239	241	128	128	108	109	125	127	32	33
250	253	237	238	129	129	108	108	242	242	94	94
247	248	244	245	118	119	73	74	209	210	3	3
164	165	187	188	139	139	71	71	224	224	4	4
210	212	108	110	149	150	72	74	236	236	10	10
211	231	107	109	129	130	10	11	20	21	66	66
129	131	222	223	154	154	39	39	236	236	26	26
102	103	23	24	235	240	17	21	248	248	28	28
55	56	45	46	156	156	176	176	232	232	146	146
				101	101	19	19	247	247	148	148
				249	254	238	243	248	248	176	176
				22	23	21	22	125	127	32	35
								248	251	246	251
								248	251	234	240
								247	248	147	148

4. Geometrical Image Scales & Orientations

4.1. Image Offsets

The next step in the image reduction is to combine the individual processed object images into a single image of either J.H. or K. The relative spatial differences between individual observations. or offsets. must be determined so that each image can be properly overlayed and produced. Remember these offsets were done intentionally so as to fully receive signal from all portions of the object and not lose anything to physically damaged pixels within the SQIID device. The SQIID-IRAF task 'sqmos' is used to build a database of the various observations of a single object into a mosaic of images each with slightly different spacial orientations. A database of offsets between different images of a single object is used to gain the coordinates needed to bring the individual exposures in each channel together into a final single image and to bring each channel into registration. The task 'sqmos' creates a tiled mosaic of images for a specific object with 1-pixel boundaries between each individual image. To combine the different object images in the database mosaic into a single final image. the relative offsets (Δx. Δy)between the individual images with respect to a reference image. must be determined. The task 'xyget' displays the reference image and then the offsets are interactively determined. The task permits the user to identify a number of point sources (stars) within the reference image. The processed object images are then examined to find a single source that is visible in each of the later sequentially scrolled processed images. The relative offsets. (Δx. Δy). from the reference image. are then determined.

4.2. CCD: Relative Channel Alignment

Images of globular cluster M5 were used with the IRAF task 'geomap' to create a database of stellar objects to compute a spatial transformation function which can be used by its companion task 'geotran' to transform one image to overlay another image. Determining the relative channel alignment was done to compute how the J and K channels translate and overlay upon the H images. In this way, the effects of relative spatial offset, rotation, and magnification can be corrected. In each J,H, & K globular cluster image, 80 common stellar objects that were distributed over the entire J, H, & K M5 exposures were individually tagged with specific (x,y) coordinates for each of the three IR colors. No reference points were chosen near the center of M5 because the stellar density of the cluster center prevents the determination of individual object coordinates. In Figure 3.3 an image in H for M5 is shown with the objects that were used within the exposure that the 'geomap' and 'geotran' combination used to compute the proper overlay of channels. In each J, H, & K color, the IRAF 'imexamine' task was used to determine individual stellar object (x,y) pixel coordinates. The 'geomap' task computes proper image overlay rotation, any shift between images in (x,y) coordinates, and normalizes the images to the same image scale.

Since the relative geometries of the detectors remain constant over an observing run, once the H band relative offsets are known, the offsets in the other passbands can be automatically determined and applied to the other colors using the SQIID-IRAF task 'xyadopt.' This also determines the relative alignment between the H, J, and K CCDs in the SQIID IR instrument. All of the individual processed images can now be combined into a single image, for each passband. When the construction of the dataset files containing the offsets and transformations is complete, the final combined images can be produced with the SQIID-IRAF task 'nircombine.' The final resulting galaxy images, once all the previous reduction has been applied, will be in the respective J, H, & K channels all calibrated to the H channel reference frame. Figure 3.4 is an example schematic for the process.

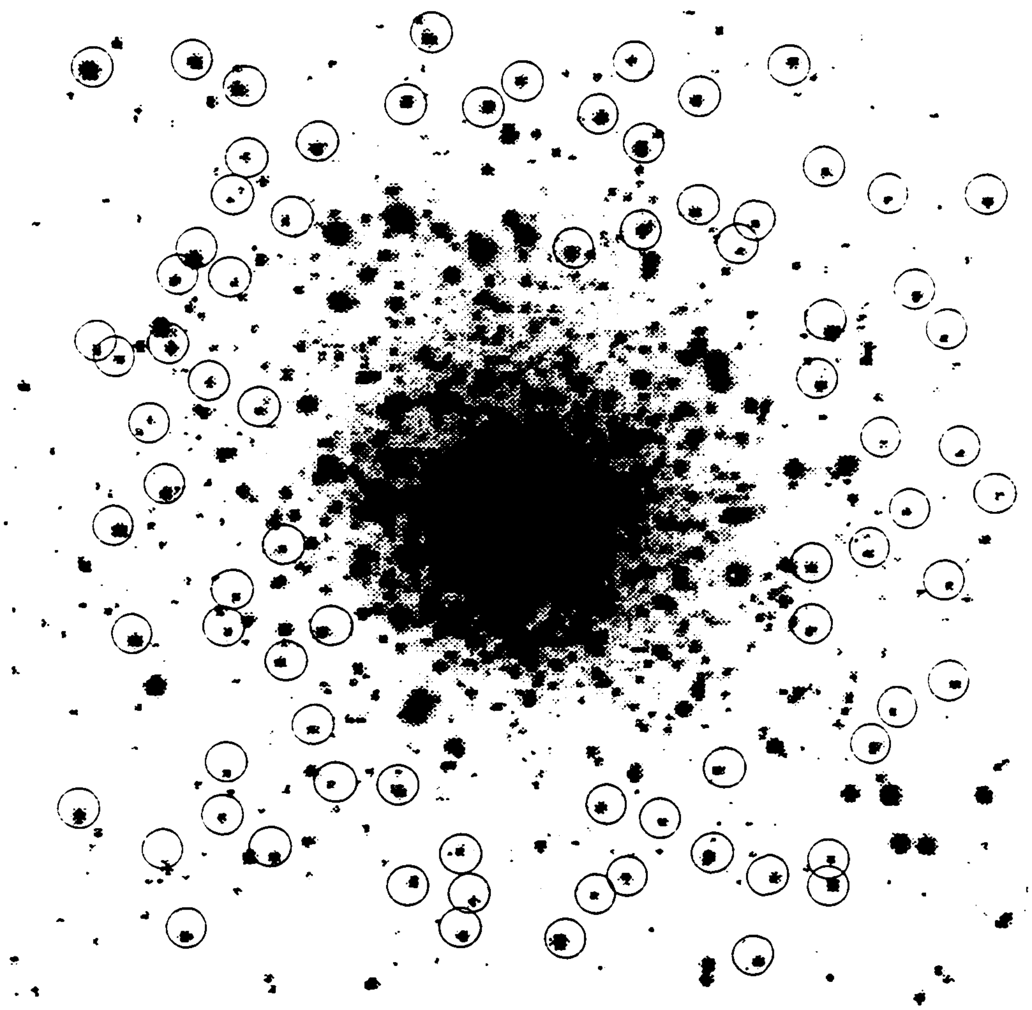

Fig. 3.3.— Globular cluster M5 used to correct for relative spatial offset, rotation, and magnification between J,H, and K channels. The circled stellar point sources were those chosen for relative channel alignment.

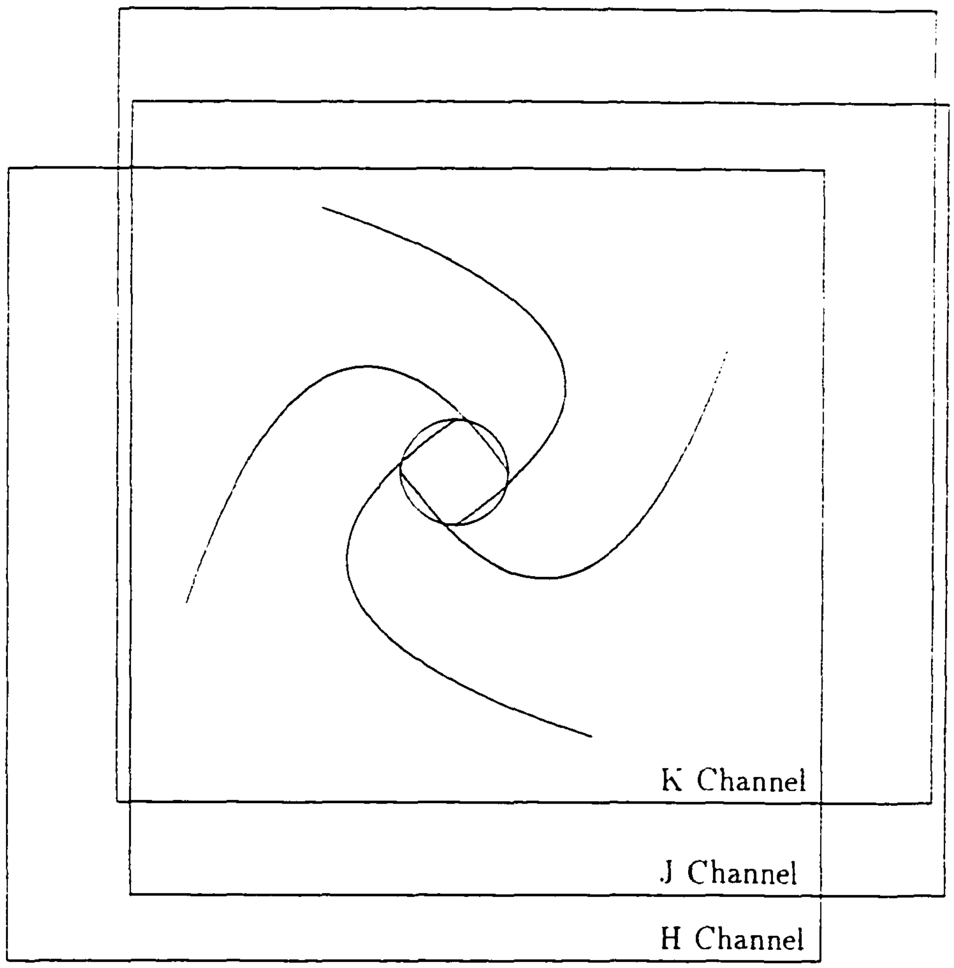

Fig. 3.4.— Schematic of overlay process between channels. The changes are in the individual images with a built-in calibration between the other channels. This allows proper processing between images in the different bands. The offsets in this example are exaggerated.

5. Image Preparation & Analysis

5.1. Extraneous Source Blanking and Image Masking

Before analysis of the combined final images can begin it is necessary to remove any stellar objects *not* associated with the spiral galaxy under study. This must occur because any extraneous light provided by galactic stars, streaks, image edge effects, cosmic rays, and other galaxies can pollute the actual galaxy source. In Figure 3.5 you can see a typical example of a blanked image of NGC4321 where all inappropriate sources and edge effects have been removed from the image.

Blanking is done with the task 'imedit.' This IRAF task is used to replace the extraneous object with circular and/or rectangular apertures of various sizes. Extraneous objects are identified first by eye, foreground stars and streaks are easy to identify in this way. Further extraneous objects were discovered in later image reduction and then removed. For instance, there is a foreground star near, in the images, the bulge of N4303 which could only be found during the surface intensity profiles performed later and noticing a large peak in the signal[2]. To replace (or 'blank') an object means to set the pixel values within the aperture to $-1x10^{10}$. A large negative value was chosen because the program (FAN) that will be used to determine the intensity profile of the galaxy will ignore pixels with such values.

The procedure for making these 'blanked' images is carried out using the following steps.

- Blank out the extra objects in the H image from the object's observation. From this blanked image a 'mask' is made by setting the value of pixels that where not blanked out equal to 0. The mask image then has pixel values of 0 for pixels to keep, and values of -1×10^{10}, for the pixels to be excluded.

[2]Actually, I thought the image had caught a NIR image of a supernovae. I was later able to rule it a foreground star because of its appearance in various optical and other wavelength images of N4303

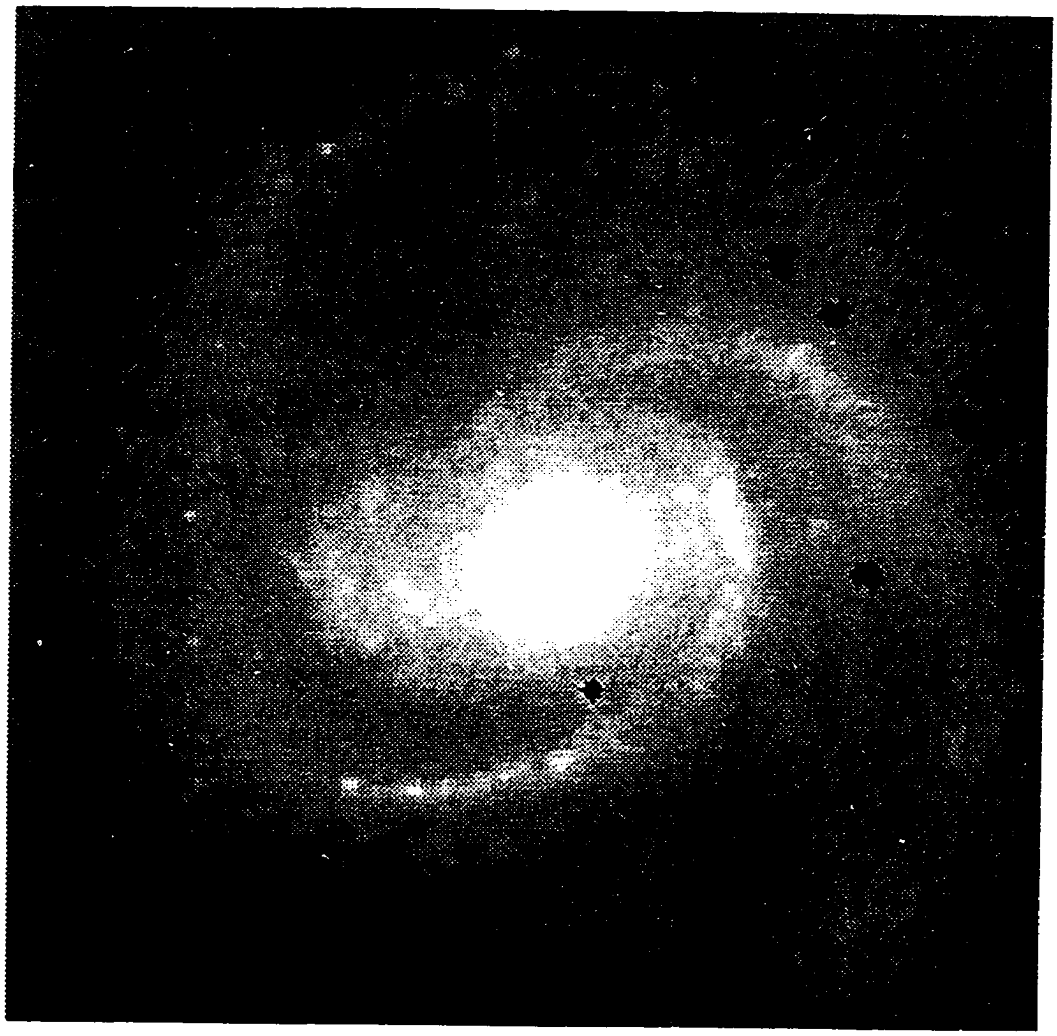

Fig. 3.5.— NGC4321 - An example of a blanked and fully processed galaxy image.

- This mask image is added to the J image from the object's observation. The 'imedit' task is used to remove any objects visible in the J image that are not visible in the H image. A mask is then made from this image.

- This mask is added to the K image from the object's observations, and extra objects are removed as needed. A mask is made from this image.

- The process is repeated for each night the object was observed.

The resulting cumulative mask is used to remove objects from all galaxy images in all colors. A single image mask is the reason all of the images in the different colors and different nights were all shifted to a common coordinate system. Using the same mask on each image also insures the same part of the galaxy would be used to determine each profile and the 'sky' value would also come from nearly the same part of each image.

Cumulative blanking masks for each object in all three passbands can then be applied to the final combined images from each single nightly observation. Once the foreground and background objects are blanked out and removed from the image all the remaining information and light should be that of tne individual galaxy and its stars, structures, and dust contributions. The edges of the individual images were also carefully analyzed for any fringing effects in the intensity signals. It was important to check the pixels at the edge of the images because the sky determination is extremely sensitive to the pixel values and signal sensitivity at increasing distance from the galaxy's central regions. Thus, the edges were often further trimmed abit to help allevaite this problem.

6. Azimuthally Averaged Magnitude Intensity Profiles

6.1. Pixel Count Intensity Profiles

Once a fully reduced, edge-trimmed, blanked, and satisfactory final image is produced the number count intensity profiles can be calculated. A specially designed fortran program entitled "FAN" originally written by Dr. W. Romanishin was used upon the J,H, and K images to determine the intensity profiles. The program was altered from its original form to run on computer machines using the LINUX floating point architecture. The program is written so as to employ IRAF reduction and image routines to properly determine the intensities from given input parameters in conjuction with the final images. The program must be compiled inside the IRAF 'cl' command structure so as to properly link with the IRAF packages that the program utilizes. The intensity program FAN needs the following initial data:

- The (x,y) fractional pixel coordinates of the galaxy center.
- Position angle of the galaxy, $PA°$
- Ellipticity - b/a minor/major axis ratio.
- Image pixel scale in arcsec/pixel ("/pixel).

The (x,y) center coordinates of each image's galaxy were found with the 'imexamine' task with image display (SAOimage) set so that the image contrast only displayed the brightest pixel values of the inner central bulge. This effectively marked the pixels containing the highest counts which were assumed to represent the exact (x,y) center of the galaxy. The IRAF 'imexamine' task, which uses a gaussian fit to the peak intensity level, could then calculate the coordinates of the galaxy center within the image that FAN needs to start any profiling. The gaussian fit returns values which are the fractional pixel (x,y) coordinates of the galaxy center.

The position angle and the b/a ratio were determined in multiple variations of a similar proceedure. A couple of ellipse fitting techniques as well as using predetermined values from RC3 catalog (de Vaucouleurs et al. 1991) were used to arrive at acceptible b/a values. First, the direct approach of displaying differing elliptical functions directly overlaid on the central bulge of the galaxy images was employed. The position angle and b/a ratio of the overlaid ellipses were iterated, by inspection, until there was a satisfactory composite match with the galaxy image. This result was then compared to another obtained by using the IRAF task 'ellipse.' The 'ellipse' task fits elliptical isophotes to galaxy images and determines levels of common brightness contours as a function of radius. It can then be used to help refine the values adopted for the galaxy position angle and b/a (Jedrzejewski 1987). So using previously published position angle and b/a ratio, those derived by inspection, and those derived by isophotal fitting, best values for each galaxy's position angle and minor to major axis ratio were determined. The values used in the rest of this analysis are include in Table 3.3.

Galaxy	$P.A.^{\circ}$	b/a
NGC4321	75.0	0.85
NGC4303	90.0	0.89
NGC4571	320.0	0.89
NGC4689	60.0	0.81
NGC4254	330.0	0.85

Table 3.3: Adopted values for the position angle and ellipticity for each galaxy.

The original pixel scales for each image in each of J, H, and K were 1.395, 1.366, 1.361 in arcsec/pixel repectively. However, during the reduction process all the images were transformed in scale to overlay the H image of the nightly individual galaxy observation and the same image scale of 1.366 arcsec/pixel (for H). All images in each color could be easily profiled and compared within the same scale.

The process of producing pixel number count intensity profiles can proceed now that the (x,y) coordinate center, position angle, ellipticity, and scale of the images have been deteremined for each galaxy. Using the values above as input along with the specific image, FAN reads each image pixel by pixel using for the spiral galaxy radius a geometrical average of $\sqrt{ab}$, determined from the b/a ratios given in Table 3.3. At a particular radius the program proceeds to bin pixels within $r = \sqrt{ab} \pm 0.5$. FAN then computes the pixel counts in each elliptical annulus bin which should have approximately the same surface brightness along that elliptical annulus around the galaxy at that radius. FAN will make some assumptions in the profiling of the image. Any data from a bin that is greater than three standard deviations (3σ) from the other data are excluded to reduce the risk of cosmic ray artifacts and/or any other extra artifacts missed in the earlier processing. The number of data points that FAN removes at this time will be very small due to the previous work of blanking all extraneous sources. FAN treats the already blanked pixel areas by assuming the values in the blanked pixels are the average value of all the other unblanked pixels along that particular elliptical annulus. The next step is to determine the residual sky subtraction for each profile. This is the most challenging part of the reduction process.

6.2. Finding the Residual Sky Values: Complete Sky Signal Correction

Determining a reasonable and sound value for any residual sky signal is the most arduous task of the reduction process in dealing with the CCD images of spiral galaxies. The galaxies in this sample are fairly close and large. However, images were acquired in such a way as to hopefully contain the maximum extent of the galaxies all within the image. Although steps were taken to consider the radial size of the galaxies within the images so as to include contributions of the sky to the pixel fluxes, not all galaxy images (particularly NGC4303) offered complete and obvious ways to faithfully represent the sky. Because of the difficulty of the process, nearly all systematic errors are a consequence of the residual sky calculation and its subtraction from the intensity profiles.

The process of residual sky determination can take place once FAN creates intensity profiles for each night and each color. The sky frame images dealt with earlier only do a partial job of removing the sky illumination contributions from the object images. The images are still left with some residual sky flux that must be removed above and beyond that determined from just the sky frames. Ideally the intensity measure beyond the outer radius of the spiral galaxy would be that of an absolutely flat profile. In practice, the point where the change in slope from steep to nearly flat of the number count intensity profile is located. This point is usually obvious in the profile, and thus when the slope becomes very shallow we have begun to reach a fairly accurate, yet tentative, value for the sky. The profiles for a particular galaxy in all three passbands were compared to one another to determine a suitable portion of the profile that corresponded to the area over which the profile's slope became very shallow, nearly flat. This area of the intensity profile is used to estimate a reasonable sky level. Two radial values were chosen, the inner radius which corresponded to the sudden lowering of the intensity gradient in the image, and the outer radius which would relate to the maximum range over which the intensity profile remained reasonably very flat. The outer range was chosen simply as the largest available radius before the edge and corners began to reduce the information of the image and had to be in common to all the images of an object. These values were chosen such that they were consistent with each of the galaxy's nightly observations as well as for each color. A simple AWK computer language routine was written to calculate between these two radii the average sky intensity and standard deviation

(σ_{sky}) of the pixel data over the selected range. The true galaxy radius can be found between these values and all the errors of sky subtraction are determined from the standard deviation of the points between these radii. Table 3.3 gives the values adopted for R_{min} and R_{max}, in arcsec for each sky calculation.

Galaxy	R''_{min}	R''_{max}
NGC4321	205	225
NGC4303	195	220
NGC4571	150	195
NGC4689	175	220
NGC4254	210	240

Table 3.3: Adopted Sky Minimum/Maximum Virgo Spiral Radii: The minimun radius is the where the intensity profiles started to become very shallow, while the maximum radius denotes the largest possible radius of the galaxy. The real Near-IR radius is somewhere between these values. These are the radial values over which sky background source signal intensity was determined.

A sample of this procedure has been shown in Figure 3.6. Only the tail end of the number count intensity profile is displayed in order to show in detail the area over which the sky subtraction was determined as well as to indicate the locations of the two radial values R_{min} and R_{max}. Notice that the profile stays nearly flat beyond R_{min} As much as was possible, R_{max} was chosen to be common to all the separate images and not completely to the edge of the image so FAN would be profiling as many pixels as possible. The squared image corners of the elliptical profile are not given as much weight in the sky determination as the inner image.

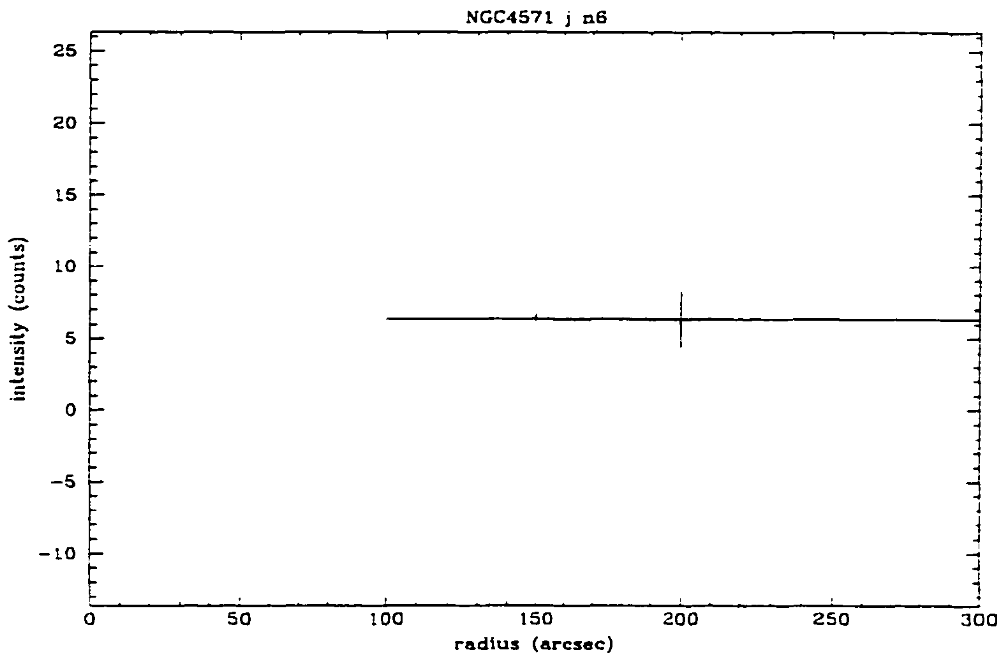

Fig. 3.6.— N4571 - A sample profile range over which the sky subtraction was determined. Any scatter in the counts over the range was used to calculate uncertainty, standard deviation, in the sky value.

7. Standard Stars - Magnitude Calibration

7.1. Observations & Calculations

CCD images are calibrated by using a list of previously observed standard stars and their respective standardized magnitudes. Elias (1982) produced a list of infrared standard stars which were also imaged during this observating run so as to calibrate the J, H, and K magnitudes of the object images. The standard star magnitudes are used to calibrate and properly assign magnitudes to the number count intensity profiles that FAN calculates for wach spiral galaxy. The standard stars are observed several times during every nightly observation run for this determination and are listed in Table 3.4 with the stars designation and standardized infrared magnitude listed in each column. Processing of the standard star images was carried out using the same techniques discussed earlier for the object images. Standard star instrument magnitudes are determined from the IRAF 'phot' package using the 'qphot' task. The IRAF task 'qphot' computes accurate magnitudes from the SQIID standard star processed images once the (x,y) position of the star in the image is known. The 'qphot' task uses the standard star position within the image to calculate the instrument magnitude of the star. The SQIID registered intrument magnitude can then be used to determined the surface magnitude of the standard star for each of the J, H, & K bands. In this way, the galaxy number count intensities can later be converted to actual surface brightness profiles.

7.2. Airmass Extinction and Zero Points

The observed surface brightness magnitude of the standard stars can be calculated via Equation 3.1 converting instrument magnitudes, determined by the 'qphot' task, to apparent magnitudes.

$$\mu_{ss_{jhk}} = \mu_{zp_{jhk}} - 2.5log(\frac{I_{ss_{jhk}}}{T_i}) - E_{x_{jhk}}(A_{m_{jhk}} - 1). \qquad (3.1)$$

where

$\mu_{ss_{jhk}}$ is the standard star apparent magnitude.

$\mu_{zp_{jhk}}$ is the zero-point of photometric calibration.

$I_{ss_{jhk}}$ is the total number of counts of the standard star minus sky counts.

T_i is the image integration time.

$E_{x_{jhk}}$ is the the airmass extinction in magnitudes/airmass.

$A_{m_{jhk}}$ is the airmass at the time observation.

The JHK subscripts indicate that this is done for each standard star in each passband. The zero point and the airmass extinction terms are determined from the standard star observations. The last airmass correction is to correct the intensity for comparison purposes to an airmass of 1, where A_m is the actual observed airmass during which the image was being collected.

The airmass extinction terms, $E_{x_{jhk}}$, are calculated from plots of instrument magnitude verses airmass so as to determined the slope of magnitude extinction per airmass in its respective channel. This was accomplished by making multiple observations of the same standard star at various airmass values during the same nightly observing run. Table 3.5 lists the calculated zero-point magnitudes from Equation. 3.1 by using the previously published calibrating magnitudes from Elias (1982) with the respective instrument magnitude and the observational airmass of the image. It also lists the extinction slope values in magnitudes per airmass increment.

8. Infrared Magnitude and Color Profiles

The calculations in the previous sections lead to the production of surface brightness profiles. The galaxy intensity (counts per pixel) profiles can now be converted into magnitude profiles via the following formula

Standard Star	m_j	m_h	m_k
GL299	8.380	7.915	7.640
HD162208	7.215	7.145	7.110
HD129653	6.980	6.940	6.920
HD161903	7.170	7.055	7.020
HD77281	7.105	7.050	7.030
HD129655	6.815	6.720	6.690
HD106965	7.375	7.335	7.315
HD84800	7.560	7.530	7.530

Table 3.4: The standard stars used to calibrate magnitudes with respective magnitudes from Elias (1982).

BAND	μ_{zp}	Error	E_x	Error
J	16.675	∓ 0.02	0.142	± 0.025
H	16.313	∓ 0.02	0.086	± 0.025
K	15.240	∓ 0.01	0.098	± 0.020

Table 3.5: Zeropoint magnitudes and extinction slopes.

$$\mu_{jhk}(R) = \mu_o - 2.5log(\frac{I(R)_{g_{jhk}} - I_{s_{jhk}}}{T_i}) - E_{x_{jhk}}(A_{m_{jhk}} - 1) \tag{3.2}$$

$$\mu_o = \mu_{zp_{jhk}} + 2.5log[(1.366)^2] \tag{3.3}$$

Where:

$\mu_{jhk}(R)$ is the galaxy's surface brightness ($mag/arcsec^2$) at radius R.

$\mu_{zp_{jhk}}$ is the zero-point of photometric calibration.

μ_o accounts for the pixel size of 1.366×1.366 $arcsec^2$.

$I(R)_{g_{jhk}}$ is the average count in a pixel width annulus at R.

$I_{s_{jhk}}$ is the sky value in its repective passband.

T_i is the image integration time.

$E_{x_{jhk}}$ is the the airmass extinction in magnitudes/airmass.

$A_{m_{jhk}}$ is the airmass at the time observation.

The starting point for this is Equation 3.1. Equation 3.3 is what is used to produce the magnitude profiles from the intensity profiles as a function of radius, $r = \sqrt{ab}$. Figures 3.7a to 3.7e show the calculated magnitude profiles for each of the five Virgo spirals. One must also calculate a magnitude uncertainty value for each point along the profiles from an estimate of error inherent to the noise in the signal at large galaxy radii as the signal to noise ratio decreases. Estimates of the minimum error due to uncertainty in the sky values were calculated between the individual R_{min} and R_{max} radii for each galaxy to arrive at a standard deviation (σ_{sky}) about the mean sky value via Equation 3.4.

$$\sigma_{sky} = \sqrt{\frac{\sum(\bar{x} - x_i)^2}{(N - 1)}} \tag{3.4}$$

The pixel values between R_{min} and R_{max} are the data points x_i over which the uncertainty is calculated for the background sky determination. This uncertainty is represented by the error bars in the magnitude plots. At each radius, magnitudes were calculated using eq. 3.3, with,

$$I(R)_{jhk} = I(R)_{g_{jhk}} - I_{s_{jhk}} \tag{3.5}$$

$$I(R)_{jhk} = I(R)_{g_{jhk}} - I_{s_{jhk}} \pm \sigma_{sky} \tag{3.6}$$

where σ_{sky} represents our uncertainty in the mean sky that was subtracted from the galaxy's intensity. The final determined magnitude profiles for J, H, & K are displayed in Figures 3.7a through 3.7e.

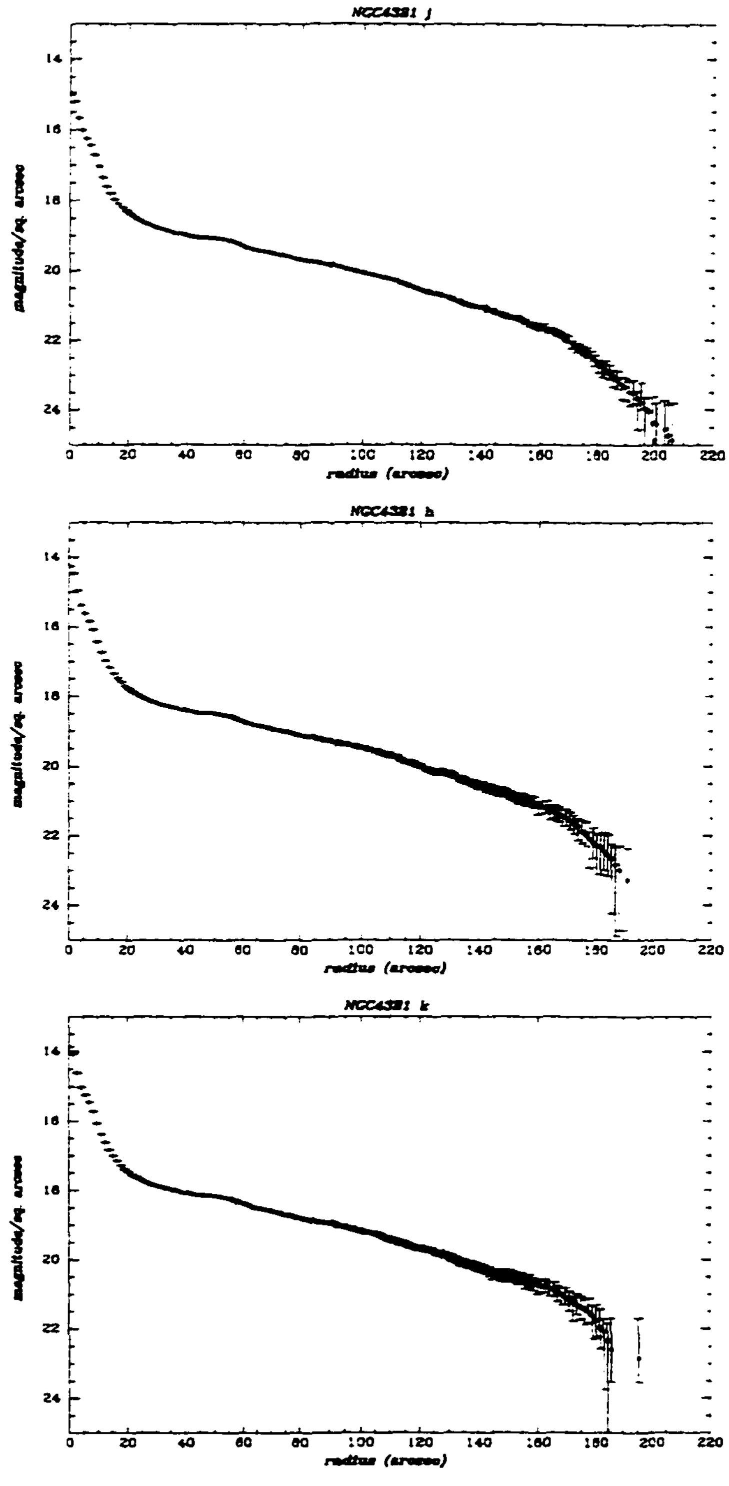

Fig. 3.7a.— NGC4321 - J, H, and K magnitude profiles.

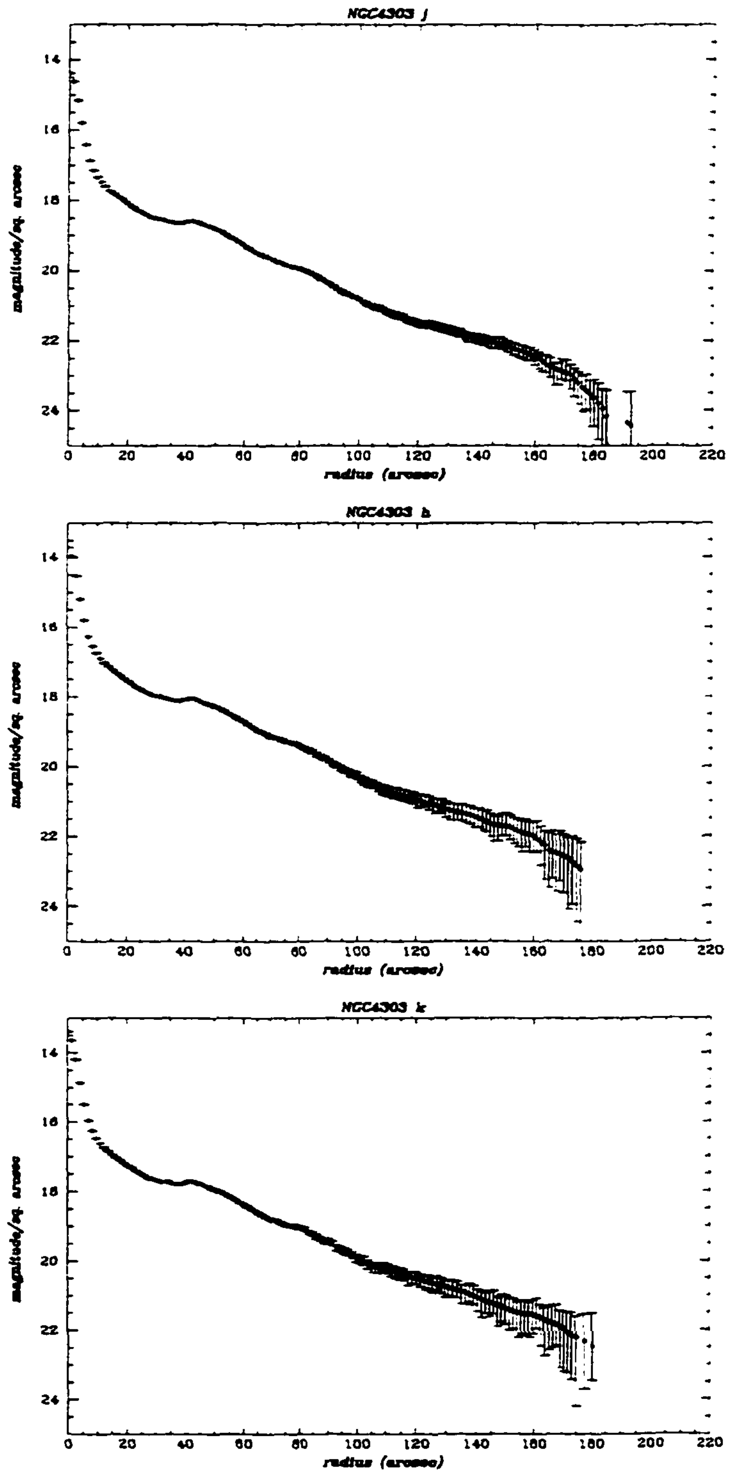

Fig. 3.7b.— NGC4303 - J, H, and K magnitude profiles.

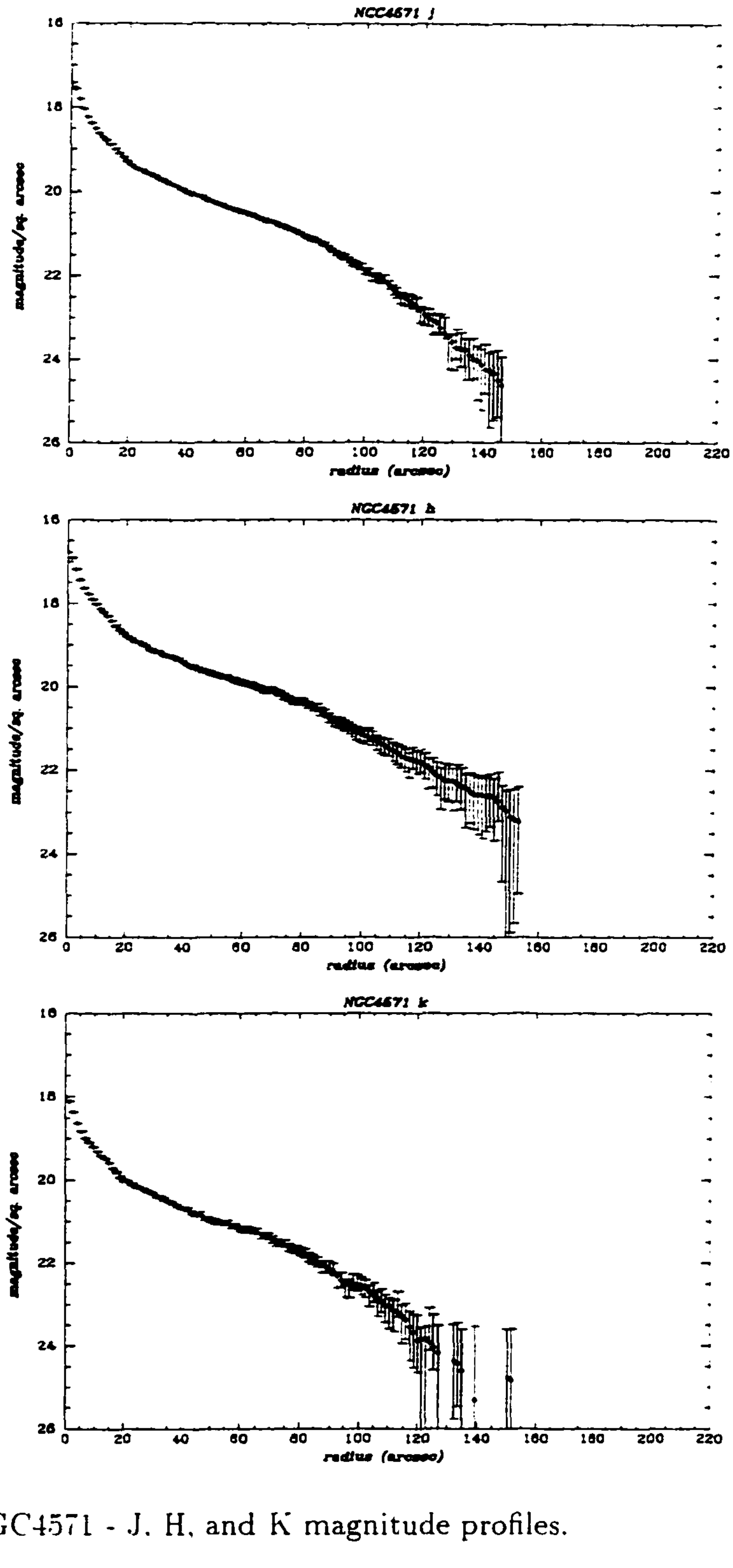

Fig. 3.7c.— NGC4571 - J, H, and K magnitude profiles.

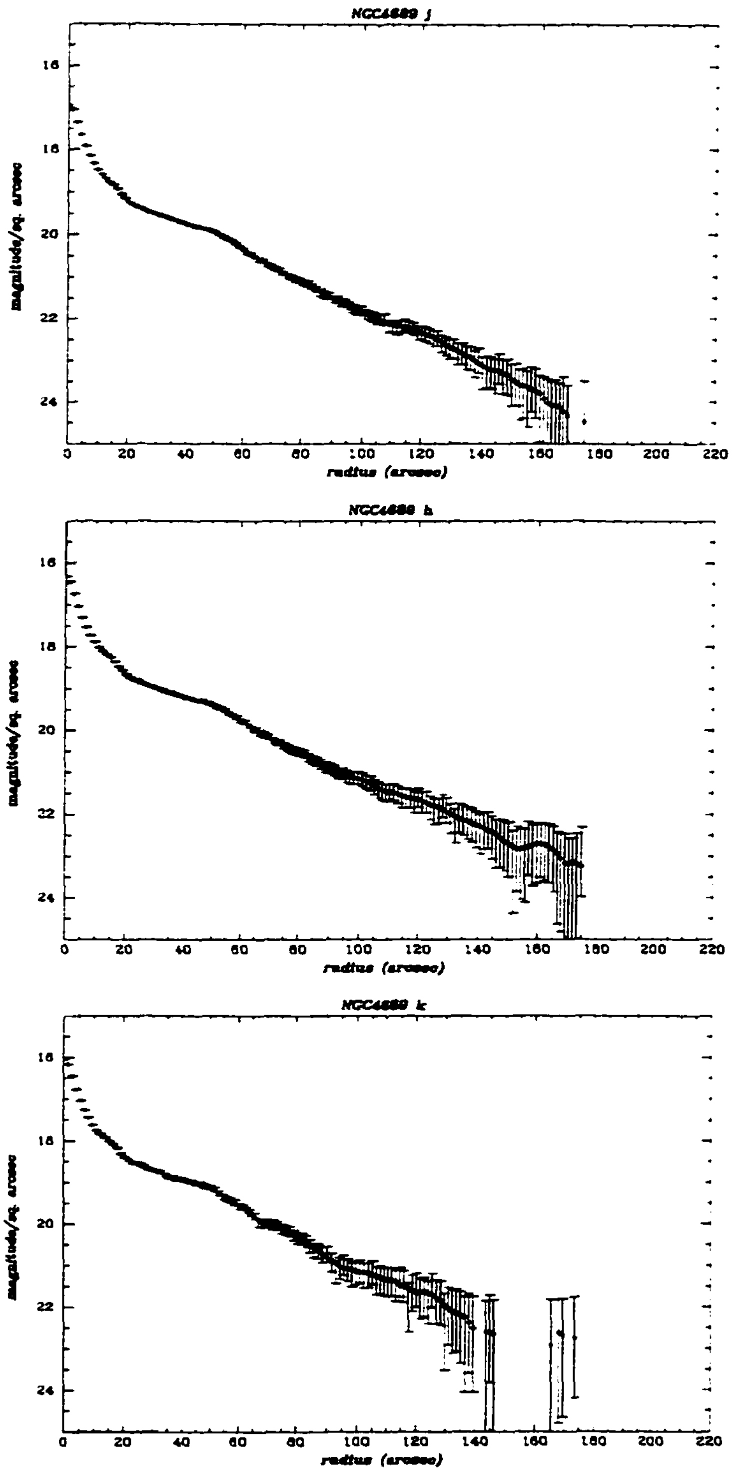

Fig. 3.7d.— NGC4689 - J, H, and K magnitude profiles.

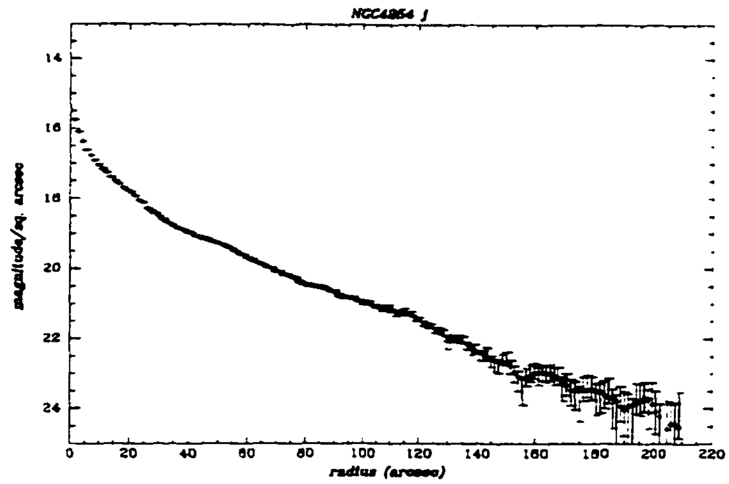

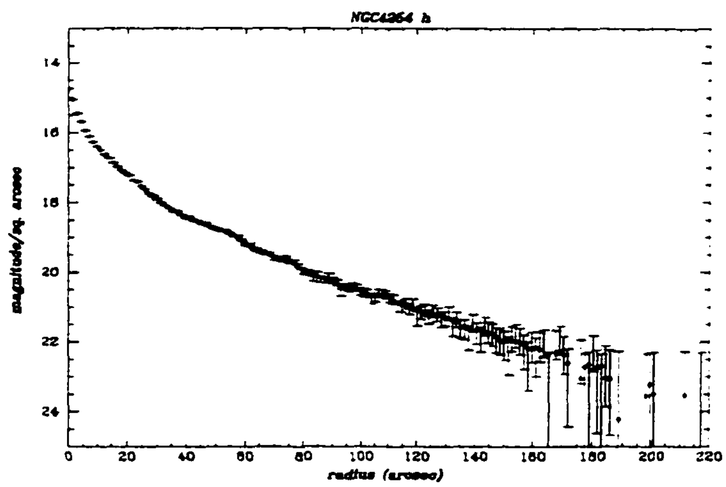

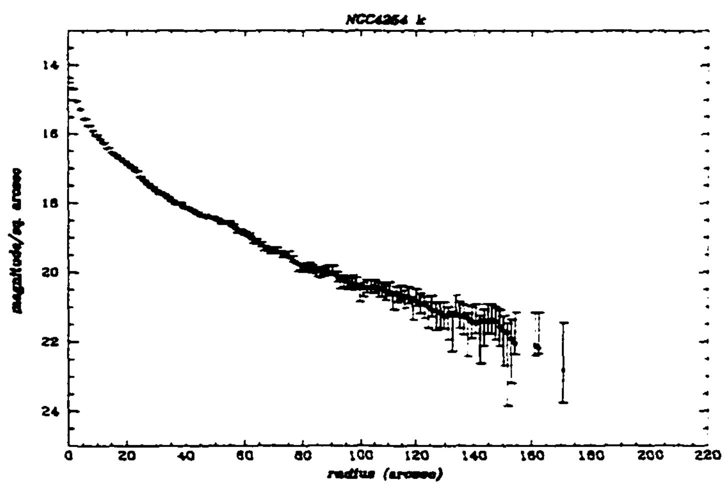

Fig. 3.7e.— NGC4254 - J, H, and K magnitude profiles.

Chapter 4

IR Image Analysis: Physical Parameter & Colors

1. Galaxy Bulge/Disk Decompositions

Finding a way to explore the physical and chemical properties implied by the J, H, and K magnitude profiles and any NIR colors is the goal of this chapter. It is also hoped that by using previous studies of the chemical compositions of structures within these galaxies that some correlation can be drawn between metallicity and the NIR colors. The advantages of studying spiral galaxies in the near infrared (NIR) have long been established from stellar population models and measurements: 1). Cool red giants and dwarfs in normal stellar populations dominate the energy output and the bolometric luminosity of a galaxy around $1\mu m$. This effectively allows the probing of a nearly homogeneous set of stars which share many similar properties and is one of the largest populations within a galaxy. 2). Extinction from dust is substantially reduced in the NIR. The obscuration and reddening of signal by dust is largly reduced and will help remove any behaviors in galaxy colors caused by dust alone. This is an extremely useful observation for tracing and studying the old cool stellar population mass distribution in spiral galaxies. In addition, since the NIR suffers less from extinction because the attenuation over the wavelengths considered goes as $1/\lambda$ (Thronson et al. 1990), the J, H, and K profiles can reveal significant structural features which are not as easily viewable in the visible wavelengths.

The intensity at any point along the radial profile of a spiral galaxy is the sum of contributions from all the luminous material from the galactic bulge, spiral disk, and halo which may lie along the line of sight. The distribution of this light can be deconvolved into separate and distinct bulge and disk components. In doing so, it is assumed that the disk and bulge are nearly physically and dynamically independent and the contribution from the halo is minimal when compared to the much more brilliant bulge and disk.

To fit radial profiles such as those reduced in Chapter 3, assumptions are made about the mathematical form of the intensity profile of each galaxy component (bulge, disk). These component profiles are then summed in an attempt to fit the observed profiles. The disk component is often treated as a flat exponential system of stars governed by rotational properties while the bulge is modeled as a much hotter system with a spherical distribution under rotational dynamics.

Many different mathematical forms of the light distribution have been attempted in previous works, for example, the Hubble-Reynolds law (Hubble 1930), the $r^{1/4}$ law (de Vaucouleurs 1948), and the King Law (King 1966). Since spiral bulges resemble the structure and light distribution of elliptical galaxies, the most commonly used model for the bulge intensity profile is the well-known de Vaucouluers $r^{1/4}$ law (de Vaucouleurs 1948, de Vaucouleurs 1958) which has been applied very successfully to the luminosity profiles of elliptical galaxies. However, the dynamical and structural properties of spiral bulges and elliptical galaxies are certainly distinct from one another. The presence of a considerable disk will definitely affect the historical properties of a spiral bulge. The spherical distribution of stars in a spiral's bulge is much more rotationally supported against gravity as opposed to the largely pressure supported dynamics of elliptical galaxy structure (Kormendy & Illingworth 1982, Kormendy 1993). The similar treatment and functional forms of the light distributions of spherical central spiral bulges and spherical elliptical galaxies is without question from the ideas linking structural and evolutional properties of the systems. However, as the amount of observations has grown, more significant deviations from the $r^{1/4}$ law have brought into question this practice (Jensen & Thuan, Shaw & Gilmore 1989, Wainscoat et al. 1989). It has become apparent that it is necessary to try alternate fitting forms and parameters for late-type spirals where the bulge is much less elliptical-like in its properties.

As observations have grown in quality and quantity the evidence for modeling the spiral bulge profiles more accurately using exponential spheroids has increased (Bahcall & Kylafis 1985, Kent et al. 1991, Andredakis & Sanders 1994). Thus, exponential fitting of spiral bulges has gained favor.

There is less controversy on fitting the light distribution of the disk component. The use of an exponential to model the outer intensity structure of spirals is common to all fitting algorithms (Kormendy 1977).

The disk/bulge decomposition was done using the IRAF-STSDAS task NFIT1D and assuming exponential radial light distributions for J, H, & K with the two spiral components as follows:

$$I(r) = I_b exp(-r/r_b) + I_d exp(-r/r_d) \quad (4.1)$$

Where:

r_b is the bulge scale length in arcsec

r_d is the disk scale length in arcsec

I_b is the bulge central surface brightness in $mag/arcsec^2$ at r_b

I_d is the disk surface brightness in $mag/arcsec^2$ at r_d

$I(r)$ is the line of sight surface brightness at radial distance r

The observed profiles derived in Chapter 3 and decomposed with Equation 4.1

are shown in Figs. 4.1a to 4.1o with the fitting coefficients in Table 4.1. These figures show the raw observational data by the solid line, the bulge contribution is the dashed line, the disk is designated with the dash-dot line, while the best fit combination of both empirical functions is the dotted line. Fits were only obtained inward from the arrow, because of error ranges considered later for derived color gradients in these NIR bands. The best fit represents the combination of the bulge and disk empirical fits that follow the observed raw data profiles with the least error. The data for positions beyond the arrow exceeded an assumed error tolerance of 0.2 mag for the colors and were thus not empirically fit.

There are some interesting behaviors to note in the individual magnitude profiles in 4.1a to 4.1o. NGC4254, NGC4303, and NGC4689 remain fairly close to an exponential disk while NGC4321 and NGC4571 seem to trail off a great deal as large galactocentric distances are reached. This might imply some variation in the stellar populations and or environmental effects from the cluster arising from the closer proximity of NGC4321 and NGC4571 to the dominate galaxy in the Virgo cluster, M87. These two galaxies, while being close to M87 have been classified in different HI classes, NGC4321 is intermediate while NGC4571 is clearly HI deficient(Skillman et al. 1996). Also, it is clear from the profiles that NGC4303 and NGC4321 are big and very bright galaxies as compared to the others in both their bulges and disks.

Another feature that NGC4689, NGC4303, and less obviously NGC4321 share is a bump in the inner portion of the profiles. These features are often indicative of bar structures in the spiral galaxies that optical observations fail to yield (Rauscher 1995).

I should remind the reader that the profile for NGC4254 is highly suspect because of the paucity of good clear observations. Only one poorly centered image was able to be created from the observations. The rise in signal that the NGC4254 profiles seem to show in J, H, & K away from an exponential decline are probably a result of not

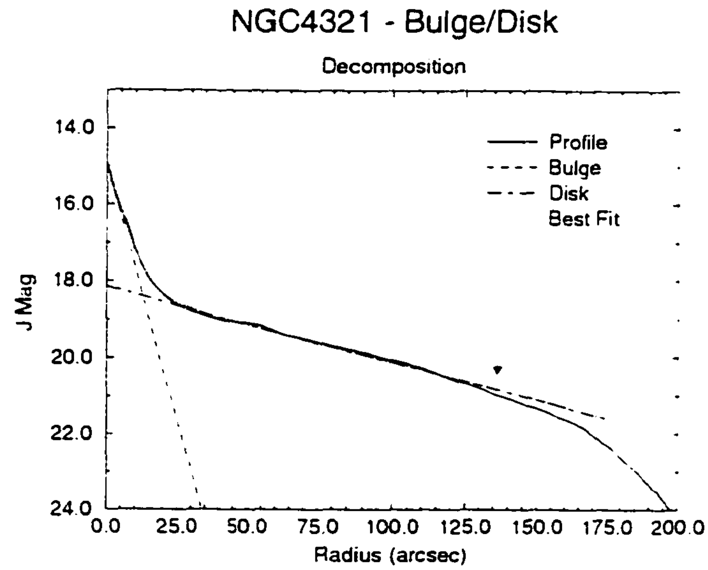

Fig. 4.1a.— NGC4321: J Band surface brightness profiles and resulting fits. The dashed line represents the bulge contribution and the dash-dot line represents the disk contribution. The dotted line is the best fit from Table 4.1

enough good observations of the galaxy. However, since NGC4254 is often described as undergoing extreme amounts of active star formation this magnitude rise mainly in H and K may be an actual feature and should be explored in the future (Binggeli et al. 1987, Rauscher 1995).

Upon careful inspection, the profiles also loosely follow the spiral arm stucture. This can be easily verfied by perusal of three-dimensional magnitude profiles created for Appendix A, figs. A.1b to A.5b. The NIR tracing the structure of the galaxy is directly related to the density of stars that are found in the spiral arms as opposed to the intra-arms. Clearly, the older stars highlighted by the NIR observations also correlate with the basic spiral structures within a galaxy and are not independent of them.

It is useful to note, as previously stated, what stars contribute at what wavelengths. The fitting parameters in Table 4.1 also point to the form of fractional contributions of different stellar populations. J, H, & K fluxes are dominated by the K and M giant branch stars and the contribution to that flux is seen in Table 4.1

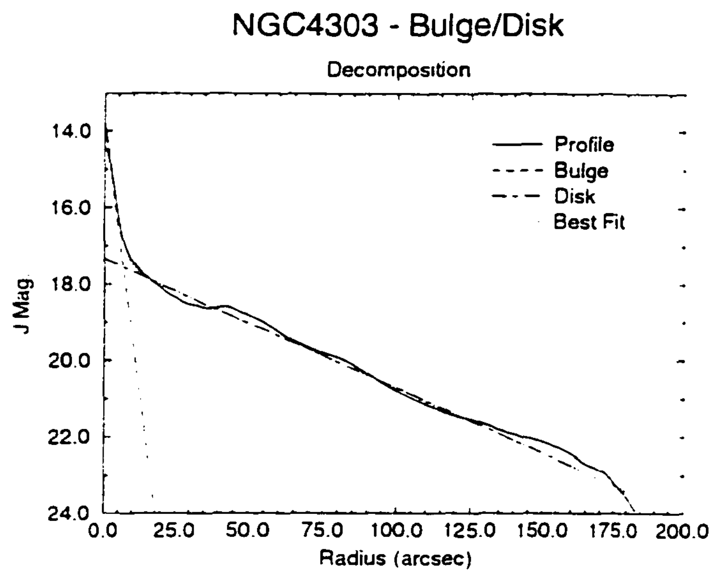

Fig. 4.1b.— NGC4303: J Band surface brightness profiles and resulting fits. Symbols defined same as Figure 4.1a.

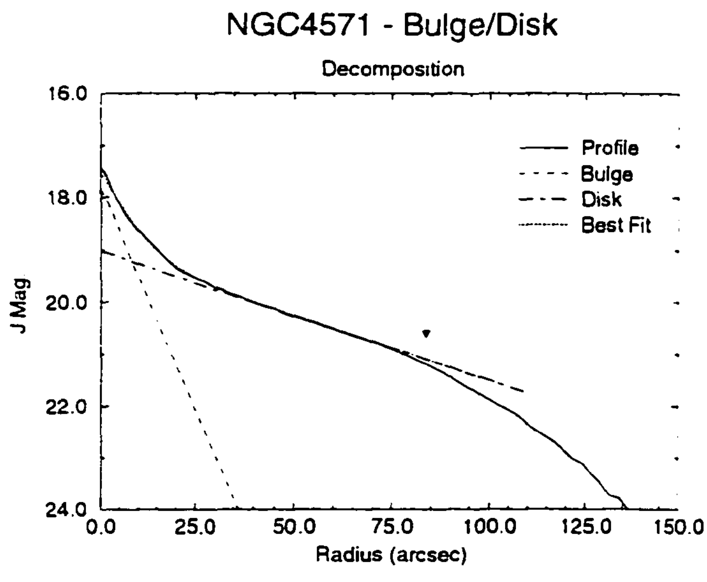

Fig. 4.1c.— NGC4571: J Band surface brightness profiles and resulting fits. Symbols defined same as Figure 4.1a.

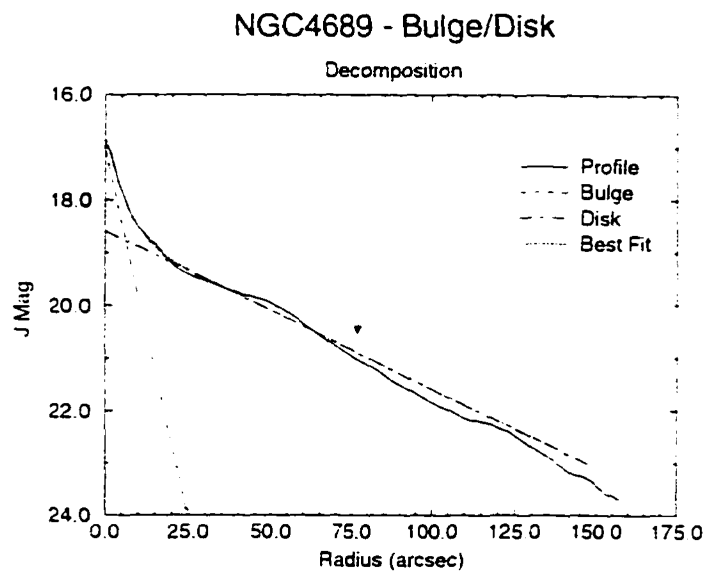

Fig. 4.1d.— NGC4689: J Band surface brightness profiles and resulting fits. Symbols defined same as Figure 4.1a.

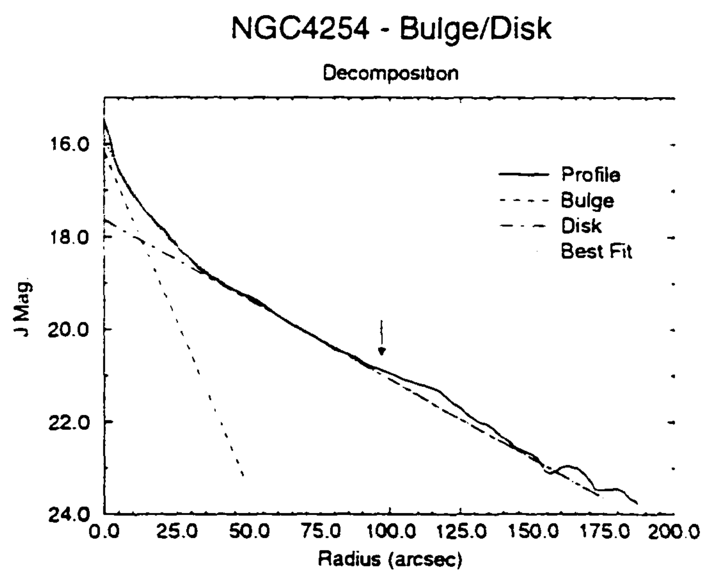

Fig. 4.1e.— NGC4254: J Band surface brightness profiles and resulting fits. Symbols defined same as Figure 4.1a.

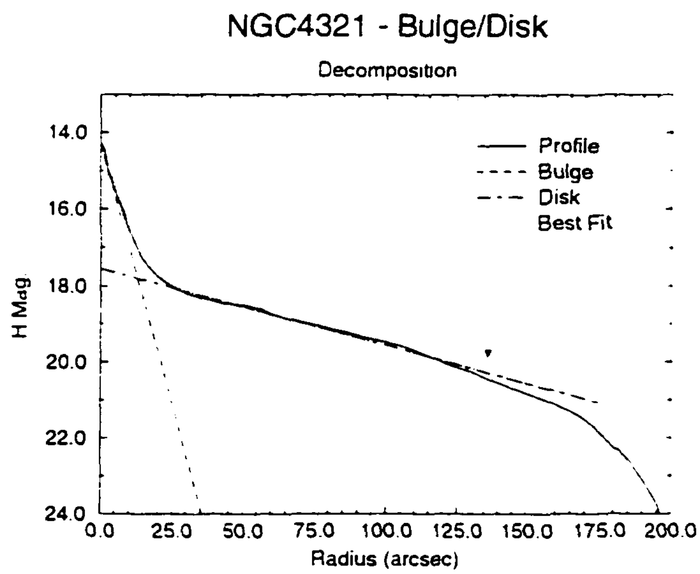

Fig. 4.1f.— NGC4321: H Band surface brightness profiles and resulting fits. The dashed line represents the bulge contribution and the dash-dot line represents the disk contribution. The dotted line is the best fit from 4.1

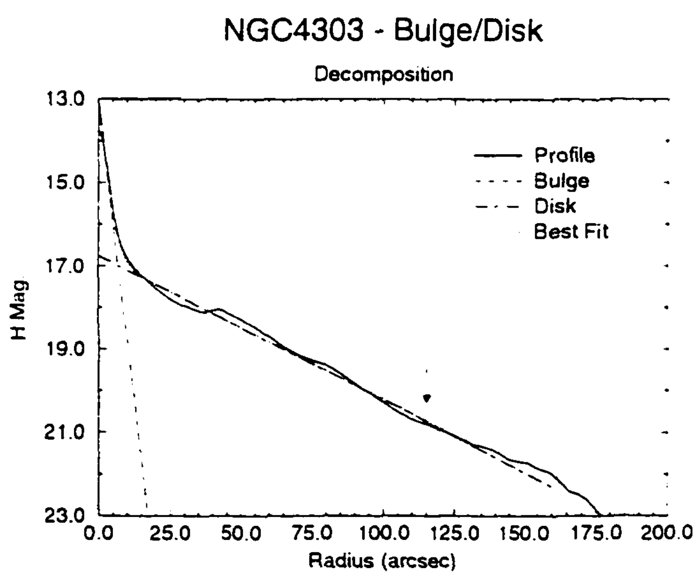

Fig. 4.1g.— NGC4303: H Band surface brightness profiles and resulting fits. Symbols defined same as Figure 4.1f.

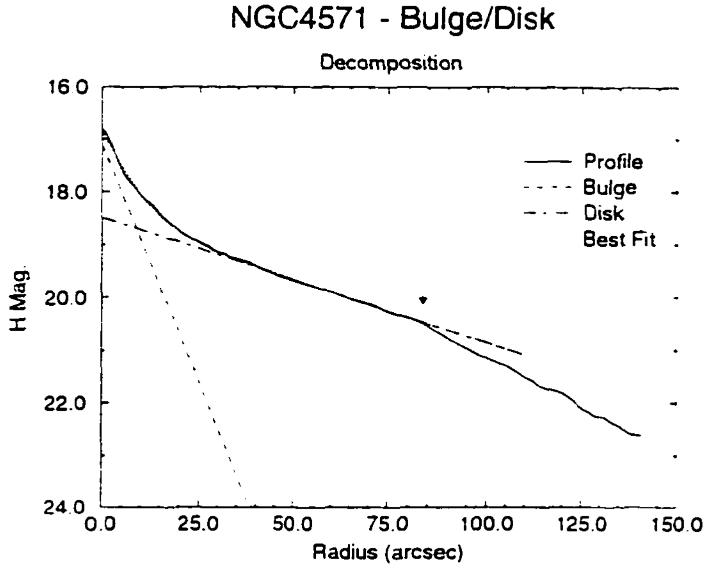

Fig. 4.1h.— NGC4571: H Band surface brightness profiles and resulting fits. Symbols defined same as Figure 4.1f.

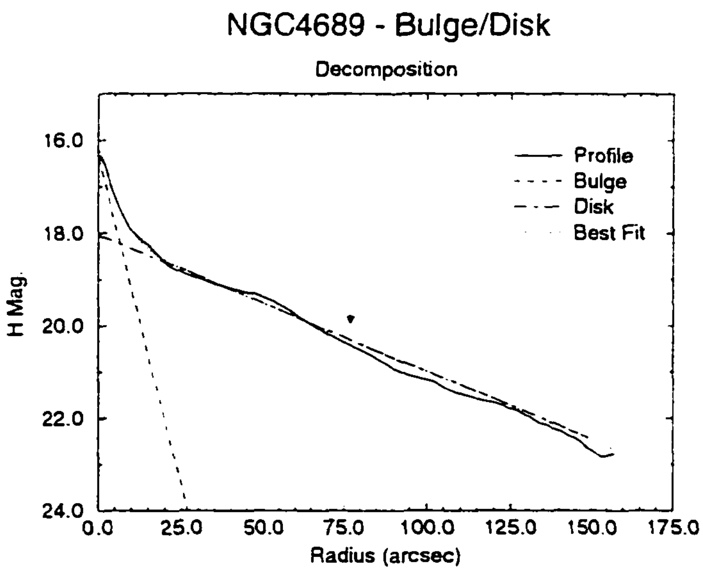

Fig. 4.1i.— NGC4689: H Band surface brightness profiles and resulting fits. Symbols defined same as Figure 4.1f.

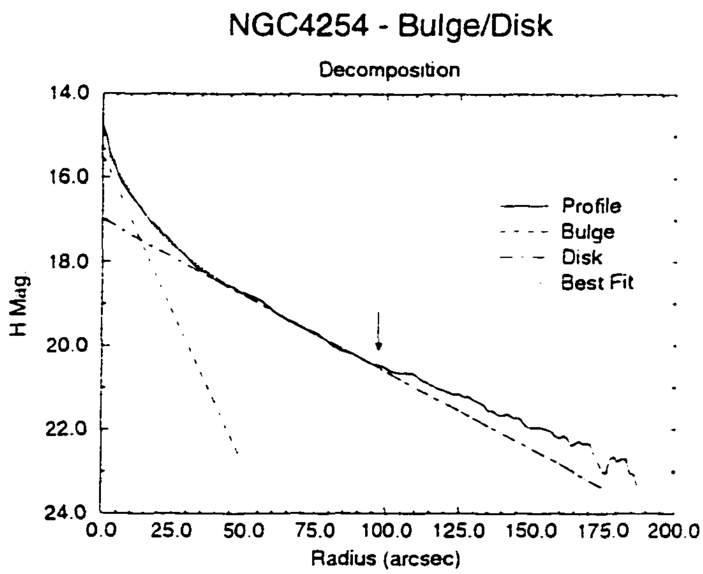

Fig. 4.1j.— NGC4254: H Band surface brightness profiles and resulting fits. Symbols defined same as Figure 4.1f.

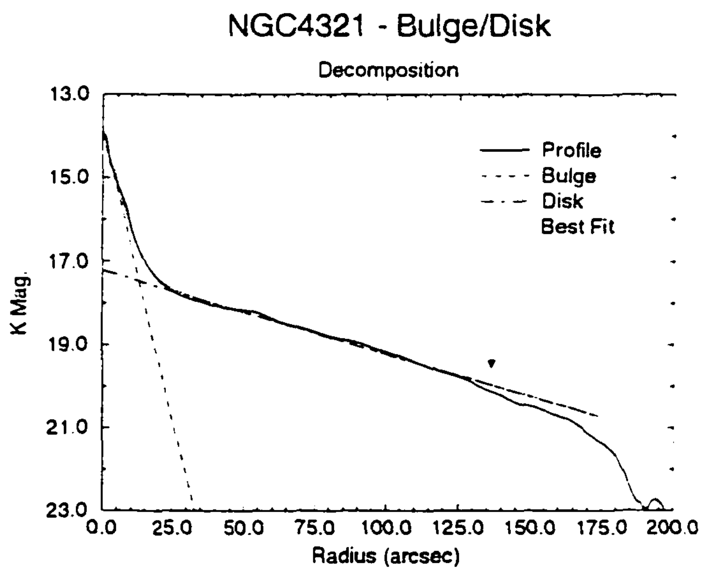

Fig. 4.1k.— NGC4321: K Band surface brightness profiles and resulting fits. The dashed line represents the bulge contribution and the dash-dot line represents the disk contribution. The dotted line is the best fit from 4.1

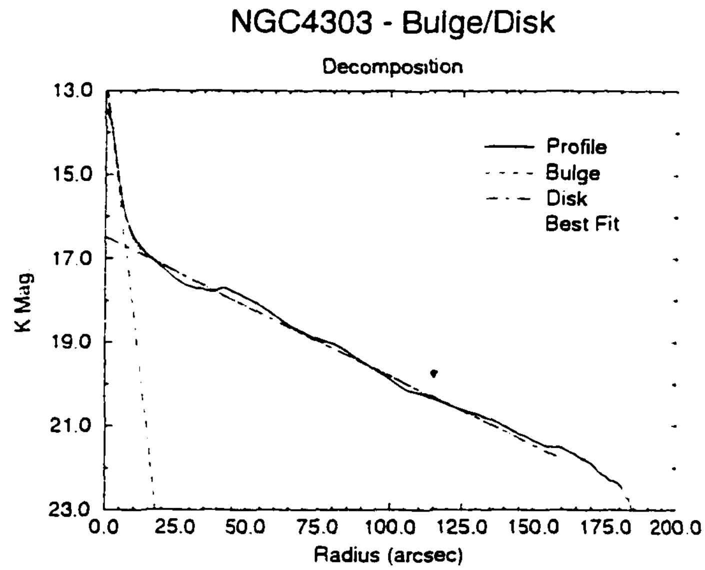

Fig. 4.1l.— NGC4303: K Band surface brightness profiles and resulting fits. Symbols defined same as Figure 4.1k.

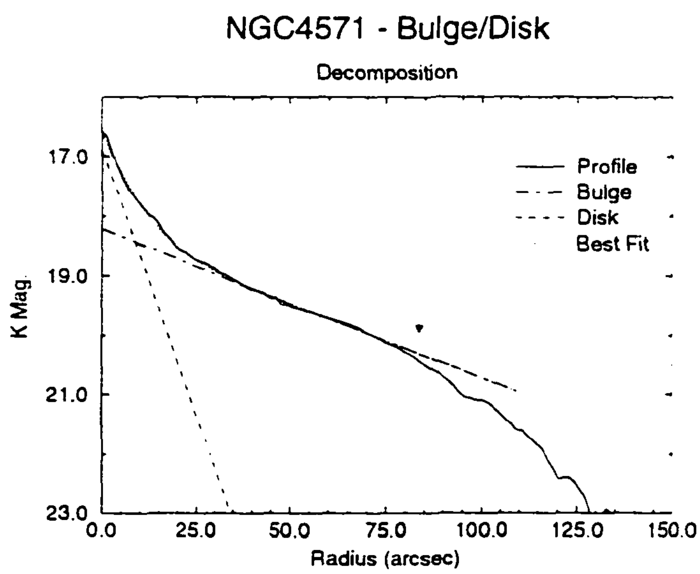

Fig. 4.1m.— NGC4571: K Band surface brightness profiles and resulting fits. Symbols defined same as Figure 4.1k.

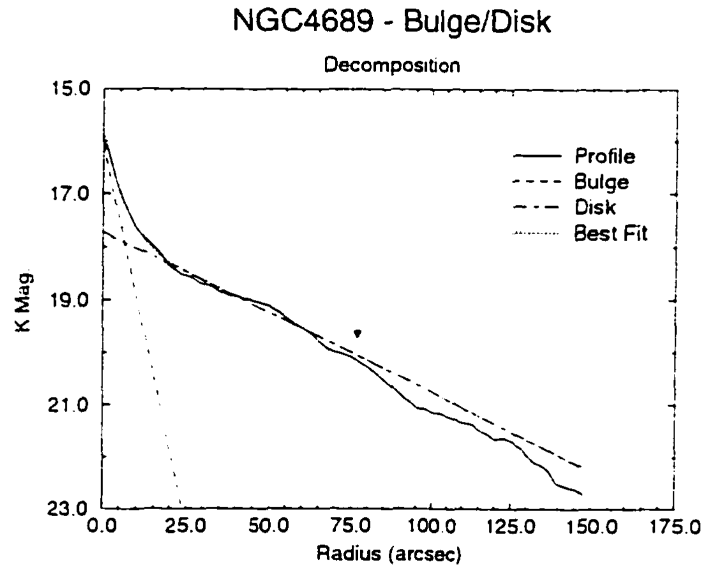

Fig. 4.1n.— NGC4689: K Band surface brightness profiles and resulting fits. Symbols defined same as Figure 4.1k.

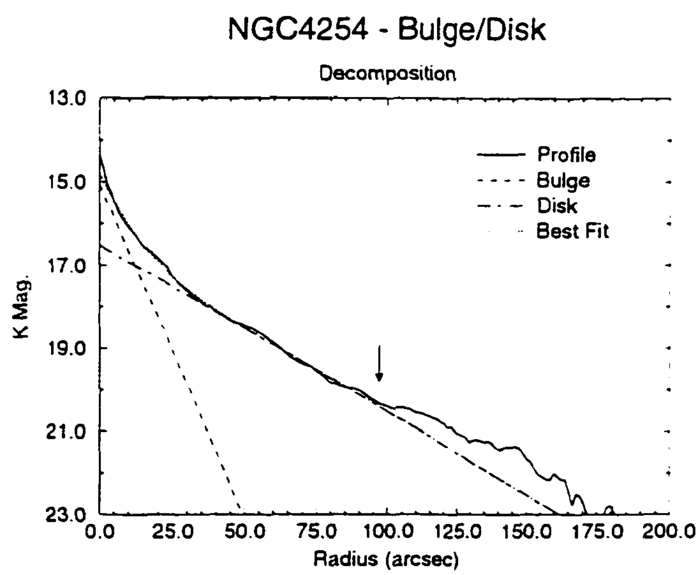

Fig. 4.1o.— NGC4254: K Band surface brightness profiles and resulting fits. Symbols defined same as Figure 4.1k.

as rising from J to K. Notice that the J luminosity is the faintest. The population synthesis models of Worthey (1994) theoretically confirm this result, specifically his Figures 41, show that the integrated J, H, & K fluxes are by far dominated by the giant stars with increasing influence through the NIR passbands. The behavior of the stellar contributions through J, H, and K helps explain the slight variation between the scale lengths in the various NIR wavelengths. Specifically, the scale lengths for each band must be different for there to be any possible color gradients. If the population mix of stars providing luminosity across J, H, and K were identical with identical scale lengths then no color gradients would be possible. Thus, color

Bulge & Disk Luminosity Profile Fitting Parameters

Galaxy		I_b ($mag./arcsec^2$)	R_b ($arcsec$)	I_d ($mag./arcsec^2$)	R_d ($arcsec$)
NGC4321	J	14.99	4.08	18.15	54.99
	H	14.31	4.00	17.55	54.06
	K	13.91	3.95	17.21	53.69
NGC4303	J	13.76	1.94	17.33	32.00
	H	13.12	1.91	16.76	31.36
	K	12.75	1.89	16.49	32.66
NGC4571	J	17.82	6.36	19.01	43.51
	H	17.10	6.03	18.49	45.80
	K	16.88	6.09	18.22	43.43
NGC4689	J	17.03	3.86	18.59	36.16
	H	16.36	3.79	18.04	36.91
	K	16.05	3.70	17.73	35.80
NGC4254	J	16.17	7.49	17.64	31.50
	H	15.48	7.36	16.99	29.73
	K	15.06	6.75	16.52	27.13

Table 4.1: The resulting fitting coefficients from the bulge/disk decompositions.

gradients must result from a slightly different mix of stars either in metallicity or age, or some other external mechanism such as a color variation caused by dust extinction (Worthey 1994). It is solely the difference in the scalelengths between J, H, and K that will result in any color gradients that are being looked for in this study.

2. Galaxy Calculations: Mass Distribution & Luminosities

At present the distribution and characteristics of stars responsible for NIR emission in late-type spirals is not very well quantified. The best that can be done in this regard is to compare the chemo-evolutionary population synthesis models of Charlot & Bruzual (1991), Worthey (1994), and Vazdekis et al. (1996) to spirals as best as one can. This study provides an opportunity to calculate and explore some of the physical dynamics of stellar mass in the disks and bulges of spiral galaxies. There are some good reasons to explore the mass and light distribution in galaxies. First, often the M/L ratio for a galaxy has some dependence on morphology which links the luminous structure of a galaxy to the distribution of mass within the galaxy. The M/L ratio is then a wonderful way to explore luminosity behaviors of the stars in contrast to the overall mass that drives the evolution of galaxies. Second, the mass-to-light ratio is also a metallicity sensitive parameter and can help lend credence to other metallicity calibrations (Worthey 1994). Finally, since the NIR light is dominated by the galaxy's expected largest stellar population of late-type stars one is exploring the largest stellar distribution within the galaxy.

There is also reason to investigate how the mass to light ratios vary from bulge to disk within a galaxy. For instance, Devereux et al. (1987) found that for a sample of elliptical galaxies, SO, and spiral bulges, all had very similar mass to light ratios. This would imply that the stars dominating the NIR luminosity are similar between the types of galaxies and some of their respective structures. Also, since spirals can have various styles of disks and different overall structures between galaxy types, clues about and differences between the star populations in these late-type spiral structures can be explored.

2.1. Bulge: Mass

There are a couple of standard methods for estimating the mass in the central bulge regions of spiral galaxies: 1) rotation curve function fitting assuming the luminosity traces mass in a similar mathematical form: and 2) using velocity dispersion measurements (Devereux et al. 1987). Previous studies have concluded that fitting rotation curves are less reliable for calculating the spiral bulge mass distribution because these fits often lead to the erroneous prediction of flat rotation curves for the inner regions, while in fact the velocity is observed to increase with radius in the inner regions of galaxies (Faber & Gallager 1979). Also, insufficient angular resolution and any non-circular motions can make rotation curve data very suseptible to error of interpretation (Devereux et al. 1987).

Nuclear velocity dispersion measurements of sample galaxies have been gathered from Devereux et al. (1987) and Whitmore et al. (1985). The methods by which spiral bulge mass estimates have been determined are described in detail by Binney (1982) and Rauscher (1995). For a spherically symmetric stellar distribution of stars, the Jean's mass equation takes the form;

$$\frac{d}{dr}[\rho(r)\sigma_r^2] + \frac{\rho(r)}{r}[2\sigma_r^2 - (\sigma_\theta^2 + \sigma_\phi^2)] = -\rho(r)\frac{d\Phi(r)}{dr} \tag{4.2}$$

$$\frac{d\Phi(r)}{dr} = \frac{GM(r)\rho(r)}{r^2} \tag{4.3}$$

Where:

σ_r is the velocity dispersion with various components σ_θ and σ_ϕ.

$\rho(r)$ is a luminosity distribution function for a spherical bulge.

$\Phi(r)$ is the gravitational potential at some distance r.

$M(r)$ is the radial mass function to be solved.

For the exponential bulge profiles considered here, $\rho(r)$ takes the form:

$$\rho(r) = \frac{I_b}{\pi r_b} K_0(r/r_b) \tag{4.4}$$

where K_0 is the modified Bessel function of order zero (Arfken & Weber 1995)

Making the substitution of Equation 4.4 into Equation 4.3 and solving for $M(r)$ we can write an expression for the mass distribution of the spiral central bulge as a function of radius.

$$M(r) = -\frac{r^2}{G\rho(r)} \sigma_r^2 \frac{d\rho(r)}{dr} \tag{4.5}$$

$$\rho(r) = \frac{I_b}{\pi r_b} K_0(r/r_b) \tag{4.6}$$

By assumption, $\sigma_r^2 = \sigma_\theta^2 = \sigma_\phi^2$, all velocity dispersion gradients are of similar extent and form. Using the series expansion approximation for the modified Bessel function K_ν with $\nu = 0$:

$$K_\nu(z) = \left(\frac{\pi}{2z}\right)^{1/2} e^{-z}[1 + \frac{(4\nu^2 - 1^2)}{1!(8z)} + \frac{(4\nu^2 - 1^2)(4\nu^2 - 3^2)}{2!(8z)^2} + ...] \tag{4.7}$$

The spiral bulge can then finally be approximated via equation 4.8 where Θ represents higher order terms of $(1/r)$.

$$M(r) \simeq \frac{r\sigma_r^2}{G}\left(\frac{1}{2} + \frac{r}{r_b} + \Theta(\frac{1}{r} terms)\right) \tag{4.8}$$

Calculating the mass adds additional assumptions (Rauscher 1995, Binney 1982):

- The system does not rotate.
- The bulge velocity dispersion is homogeneous and isotropic.
- Any mass-luminosity ratio is constant over the bulge.
- The disk potential can be neglected in a sufficiently small nuclear region.

Since no data exist in the literature for the bulge velocity dispersion for NGC4571 and NGC4689, σ_r, a value was approximated by comparing results of similar galaxies and adopting a representative average. The value adopted for both NGC4571 and NGC4689 was $50 km/s$. All other dispersion measurements are from Whitmore et al. (1985) and Devereaux et al. (1987).

2.2. Bulge: Luminosity

The luminosity of the bulge can also be approximated assuming the mass and light follow the same functional density form (Rauscher 1995) and the bulge system is taken to be completely transparent.

$$L(r) = \int_0^r \int_0^\pi \int_0^{2\pi} \rho(r) r'^2 dr' \sin \phi d\phi d\theta \tag{4.9}$$

$$= \int_0^r \int_0^\pi \int_0^{2\pi} \frac{I_b}{\pi r_b} K_0(\frac{r'}{r_b}) r'^2 dr' \sin \phi d\phi d\theta \tag{4.10}$$

$$= 4 I_b r_b^2 \int_0^{r/r_b} x^2 K_0(x) dx \tag{4.11}$$

For these galaxies in the Virgo cluster the assumption of negligble extinction is probably reasonable.

2.3. Disk: Mass

To approximate the mass of the disk we can use a rather modest approach once we have our bulge masses. We can consider a simple model in which the galaxy is spherical. The spherical model is much simpler than flattened disk models, and flattening generally has only a small effect upon the mass calculation (Binney & Tremaine 1987). Using the basic formulae:

$$F = \frac{GM(r)m}{r^2} \tag{4.12}$$

$$a = \frac{GM(r)}{r^2} \quad (4.13)$$

$$\frac{v^2}{r} = \frac{GM(r)}{r^2} \quad (4.14)$$

$$M(r) = \frac{rv^2}{G} \quad (4.15)$$

Equation 4.15 will be the mass of material within some radius (r) which will be the bulge mass plus any disk mass out to some radius beyond the spiral bulge. First, we need a rotation curve for the galaxies. Figure 4.2 contains the rotation curves for the galaxies taken from Guhathakurta et al. (1988).

Disk masses have been calculated out to where the rotation curves peak (V_{max}). The Formula 4.15 then becomes:

$$M_{disk} = M(r) - M_{bulge} \quad (4.16)$$

$$M_{disk} = \frac{rV_{max}^2}{G} - M_{bulge} \quad (4.17)$$

2.4. Disk: Luminosity

Once the functional form of the bulge is determined through decomposition, the calculation of disk luminosity is rather straightforward.

$$L(r) = \int_0^r \int_0^{2\pi} I(r')r'dr'd\theta \quad (4.18)$$

$$= \int_0^r \int_0^{2\pi} I_d exp(\frac{-r'}{r_d})r'dr'd\theta \quad (4.19)$$

$$= 2\pi I_d \int_0^r r'exp(\frac{-r'}{r_d})dr' \quad (4.20)$$

The results of these calculations are in Tables 4.2 and 4.3. You can see the relatively good agreement between the calculated masses and luminosities with

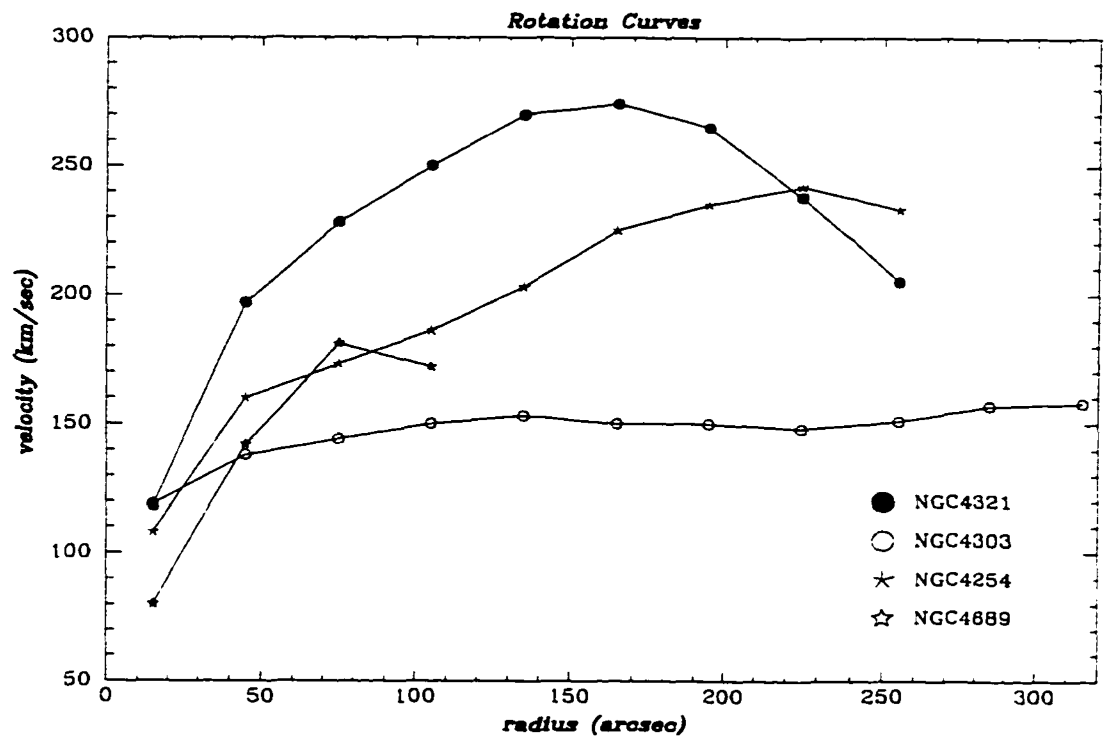

Fig. 4.2.— Available rotation curves used in the approximate determination of disk masses taken from Guhathakurta et al. (1988).

Virgo Spiral Galaxies: Inner Bulge Masses & Luminosity

Galaxy		$[\frac{L}{L_\odot}]$	$[\frac{M}{M_\odot}]$	$[\frac{M}{L}]$	$[\frac{L}{L_\odot}]$	$[\frac{M}{M_\odot}]$	$[\frac{L}{L_\odot}]$	$[\frac{M}{M_\odot}]$
NGC4321	J	9.25	8.98	0.54	...	...	...	...
	H	9.40	8.98	0.38	9.5	9.0	...	...
	K	9.54	8.98	0.28	...	...	9.2	9.2
NGC4303	J	9.45	9.12	0.47	...	...	...	...
	H	9.59	9.13	0.35	9.7	9.0	...	...
	K	9.71	9.13	0.26	...	...	9.5	8.9
NGC4254	J	8.99	9.51	3.31	...	...	...	...
	H	9.15	9.50	2.23	9.3	9.4	...	...
	K	9.26	9.48	1.66	...	...	8.9	9.4
NGC4571	J	8.27	8.54	1.86	...	...	...	...
	H	8.42	8.52	1.26	...	...	...	...
	K	8.49	8.53	1.10	...	...	...	...
NGC4689	J	8.42	8.46	1.10	...	...	...	...
	H	8.57	8.46	0.78	...	...	...	...
	K	8.66	8.46	0.63	...	...	...	...
	(2)	(3)	(4)	(5)	(6)	(7)	(8)	(9)

Table 4.2: Bulge luminosity, mass and M/L ratios calculated out to r=250pc to compare to previous literature results. Masses and luminosity are given in log form. Columns (6), (7) are similar results by Devereux (1988) at r=250pc. Columns (8), (9) are results by Rauscher (1995) at r $\simeq$ 214pc. The calculations were done for each of the passbands so as to compare results derived for different wavelengths. Luminosities were calculated using the solar luminosity in J,H, and K being +3.93, +3.65, and +3.59 respectively. The Virgo distance used was 16.8 Mpc, except for NGC4303 which was 15.2 Mpc. No velocity dispersion data, σ, was available for NGC4571 nor NGC4689 so an estimate of 50 km/s was adopted for analysis purposes.

previous published values. Table 4.2 only gives the results for the bulges of the galaxy sample.

Table 4.2 shows the resultant inner bulge masses and luminosities. The masses and luminosities were all calculated out to the same galactocentric distance of 250 parsecs so as to compare to the previous determinations of Devereux et al. (1987) in the H band. Also, similar masses and luminosities were done by Rauscher (1995) in K but only to approximately 214 parsecs. This study has used all J, H, & K bands to estimate the luminosity, mass, and mass to light ratios so as to compare how the various NIR wavelengths can help verify theoretical predictions for the relative

Virgo Spiral Galaxies. Full Bulge/Disk Masses & Luminosity

Galaxy		Radius(″)	$[\frac{L_{bulge}}{L_\odot}]$	$[\frac{M_{bulge}}{M_\odot}]$	$[\frac{L_{disk}}{L_\odot}]$	$[\frac{M_{disk}}{M_\odot}]$	$[\frac{M}{L}]_{bulge}$	$[\frac{M}{L}]_{disk}$
NGC4321	J	12.81	10.03	9.87	10.95	11.36	0.69	2.57
	H	12.89	10.17	9.88	11.06	11.36	0.51	2.00
	K	12.92	10.30	9.89	11.17	11.36	0.39	1.55
NGC4303	J	6.78	9.81	9.65	10.81	11.07	0.69	1.82
	H	6.82	9.96	9.65	10.91	11.07	0.49	1.45
	K	6.90	10.07	9.66	11.03	11.07	0.39	1.10
NGC4254	J	13.28	9.81	10.13	10.76	11.38	2.09	4.17
	H	13.55	9.98	10.15	10.86	11.38	1.48	3.31
	K	12.20	10.04	10.10	10.94	11.38	1.15	2.75
NGC4571	J	8.22	8.83	8.92	...	...	1.23	...
	H	8.88	9.04	8.98	...	...	0.87	...
	K	8.71	9.09	8.97	...	...	0.78	...
NGC4689	J	6.18	8.84	8.89	10.29	< 10.67	< 1.12	< 2.39
	H	6.56	9.02	8.89	10.41	< 10.67	< 0.74	< 1.82
	K	6.37	9.10	8.88	10.50	< 10.67	< 0.60	< 1.48
	(2)	(3)	(4)	(5)	(6)	(7)	(8)	(9)

Table 4.3: Full bulge and disk mass and luminosity results. The radius of adopted bulge size, where the fitted bulge and disk profiles are equal, is in column (3). Column (4) and (5) is the adopted full bulge luminosity and mass in logs. (6) and (7) are the disk mass and luminosity calculated out to r for V_{max} and finally (8) and (9) contain the M/L ratio for the disk and full bulge. No rotation curve information was available for NGC4571.

contributions of different stellar types to the NIR. The agreement between studies is quite good.

To estimate the masses of the spiral disks of the galaxies a slightly different method was applied. Using the decompositions of the light distribution in the respective J, H, and K bands an assumed full bulge mass was calculated out to where the disk and bulge decompositions were equal. In other words, the end of the region where the bulge mass dominated the galaxy to where the disk mass began to dominate was defined as the point where the separate components distributions were equal. This point was used in this study to *define* a full bulge size rather than just some smaller portion as was done earlier in this chapter for comparison purposes to Devereux et al.

(1987) and Rauscher (1995). Once a mass for the bulge was determined, an estimate for the disk mass out to r for V_{max} could be approximated by subtracting the bulge mass via Equation 4.17.

The results show that the M/L decreases going from J to K for both the bulge and disk. The NIR luminosities are dominated by old giant stars and their contributions in flux increase going from J to K (Worthey 1994). The dynamical mass derived for each spiral component stays relatively the same as the luminosity increases across the NIR thus the M/L ratio is driven down.

Mass to light (M/L) ratios are also metallicity sensitive parameters (Vazdekis et al. 1996, Worthey 1994). Lower M/L means brighter populations. Worthey (1994) has shown that, while M/L in optical wavelengths increases with metallicity, around 1μm the trend reverses and in the NIR M/L decreases with metallicity. That is, more metal rich populations are dimmer in U, B, & V but brighter in J, H, & K. Consequently, the values derived above for the M/L ratios can suggest which galaxies and their structures when compared to one another are more metal rich. Thus, this would imply that the stellar component of NGC4321 and NGC4303 bulges may tend to be more metal rich than the other three galaxies, likewise for their respective disks. Additionally, by comparing the change in NIR M/L ratio between the bulge and disk of an individual galaxy an idea about how much change in metallicity, and any gradients, between the bulge and disk can be estimated if one assumes that the difference is not related to any change in stellar population. Specifically, in looking at NGC4321 as compared to NGC4303 there is a larger M/L increase between bulge and disk for NGC4321 which may imply a larger difference in metallicity. If, in fact, J-K is a sensitive measure of metallicity then it should show more variation in color for NGC4321. Giovanardi & Hunt (1996) also determined that metallicity and J-K seem to correlate with mass more strongly than with Hubble Type. The centers of galaxies with the more massive bulges are also more metal rich. In this sample this would imply that NGC4254, having the most massive bulge, may have some of the reddest colors, due to the high metallicity, and because the M/L ratio difference between bulge and disk is one of the largest may consequently have a strong metallicity gradient in the NIR. So, the M/L behaviors further lead to the hope the NIR can be used as a probe of the metal contents of the stars within the galaxies.

3. Color Abundance Analysis

Colors have long been used as a tool to study various physical and chemical characteristics of stellar populations of galaxies (Tinsley 1980, Frogel 1985, Terndrup et al.1994, Peletier 1989, Balcells & Peletier 1994, Héraudeau et al. 1996). Colors are often used as probes of dust, stellar age, and metallicity, but because of the similarity in effects that each can have on the integrated light of stellar populations, it is often a very hard task to disentangle their separate effects. For instance, if one assumes that dust is more concentrated towards the center of spiral galaxies and their bulges, the higher extinction can contribute to a color gradient that makes the galaxy redder closer to the bulge. Similarly, a gradient or mix in stellar population and/or metallicity can produce color gradients that may or may not be physically or chemically indicative of the stars in the galaxy but closely mimic any observed color gradients (Vazdekis et al. 1996, Worthey 1994, Charlot & Bruzual 1991).

Near-Infrared (NIR) wavelengths have a distinct advantage over optical wavelengths when it comes to minimizing the effects of extinction by dust. J, H, and K are much less attenuated than their U, V, and B cousins because extinction, over the wavelengths considered, goes as $1/\lambda$ (Thronson et al. 1990). Thus, the NIR can penetrate areas that may have higher dust content than the visual wavelengths and can peer more accurately into areas that have higher dust concentrations, such as those expected in the nuclear regions of spiral galaxies. However, one can not explicitly rule out any contribution to the colors from dust even in the NIR. For instance, de Jong (1996) has found that dust can produce color gradients in face-on galaxies, even in the NIR, but that it would require quite high central optical depths and extra long dust scale lengths.

The analysis of color profiles begins with Figures 4.3a to 4.3e and attempts to separate the contributions to colors of the spiral bulge and disk, analogous to what was done earlier to approximate the masses and luminosities of each component.

Once we are certain of the magnitude profiles for each of J, H, and K created in Chapter 3 it becomes a simple matter to produce the azimuthally averaged color profiles for J-K, J-H, and H-K from the raw data points. Any errors in the determined colors are a direct result of the standard deviation in signal of the residual sky determination of Chapter 3. The error bars in the color profiles were determined by combining the errors, in quadrature, from each separate intensity profile before they are converted to log based numbers for a galaxy's set of observations, as shown in the following equations:

$$(J-K)_{err} = \sqrt{(J_{err})^2 + (K_{err})^2} \tag{4.21}$$

$$(J-H)_{err} = \sqrt{(J_{err})^2 + (H_{err})^2} \tag{4.22}$$

$$(H-K)_{err} = \sqrt{(H_{err})^2 + (K_{err})^2} \tag{4.23}$$

Where:

J_{err} is the J intensity error introduced by residual sky error.

H_{err} is the H intensity error introduced by residual sky error.

K_{err} is the K intensity error introduced by residual sky error.

$(Color)_{err}$ is the error introduced by residual sky standard deviation.

Many of the complexities of the profiles are, for the moment, overlooked because we are considering the mean behaviors in the color plots. For instance, a careful

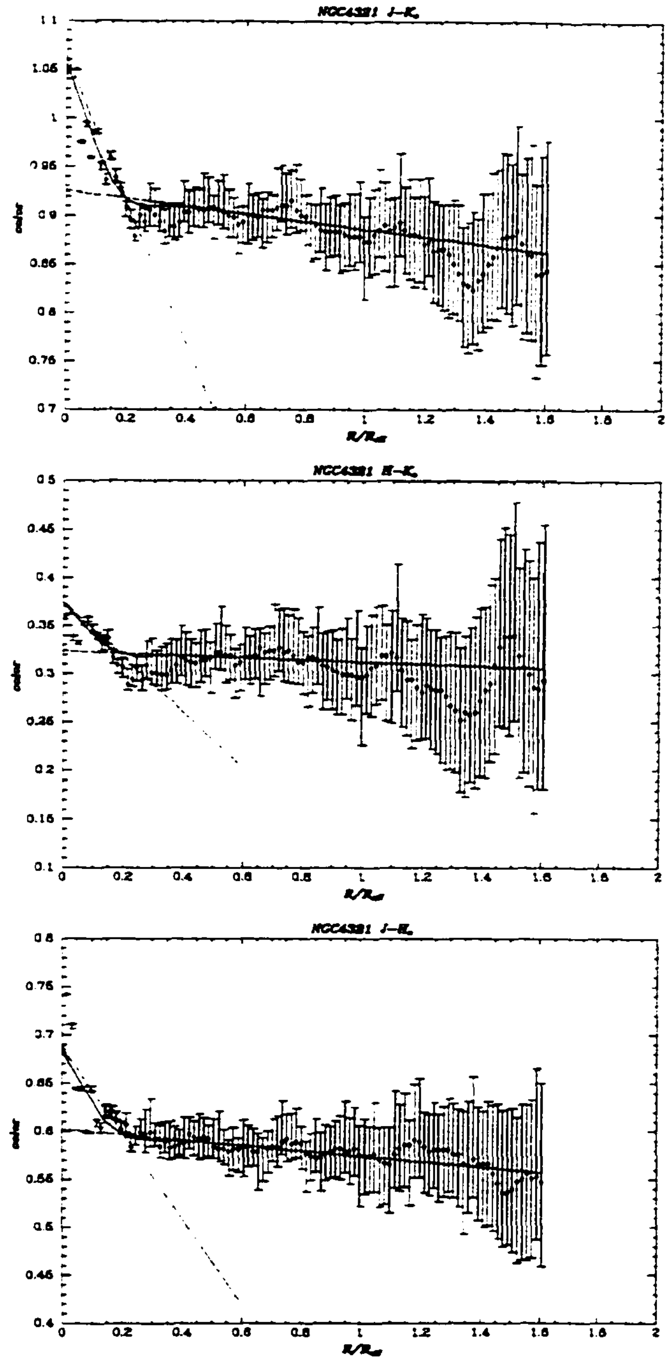

Fig. 4.3a.— NGC4321 - J-K, H-K, & J-H Color profiles. The filled circles represent the raw data points along the profile with the appropriate error bars introduced from the uncertainty in the sky subtraction. The dotted line follows the bulge color profile intensity fit while the dashed line follows the decomposed disk color fit. The combined color fits are the solid line. The effective radius, R_{eff} is as defined in Table 3.1. Only those points with error bars less than about 0.2 magnitudes are plotted for only those really can definitively show any color behavior on this fine color scale.

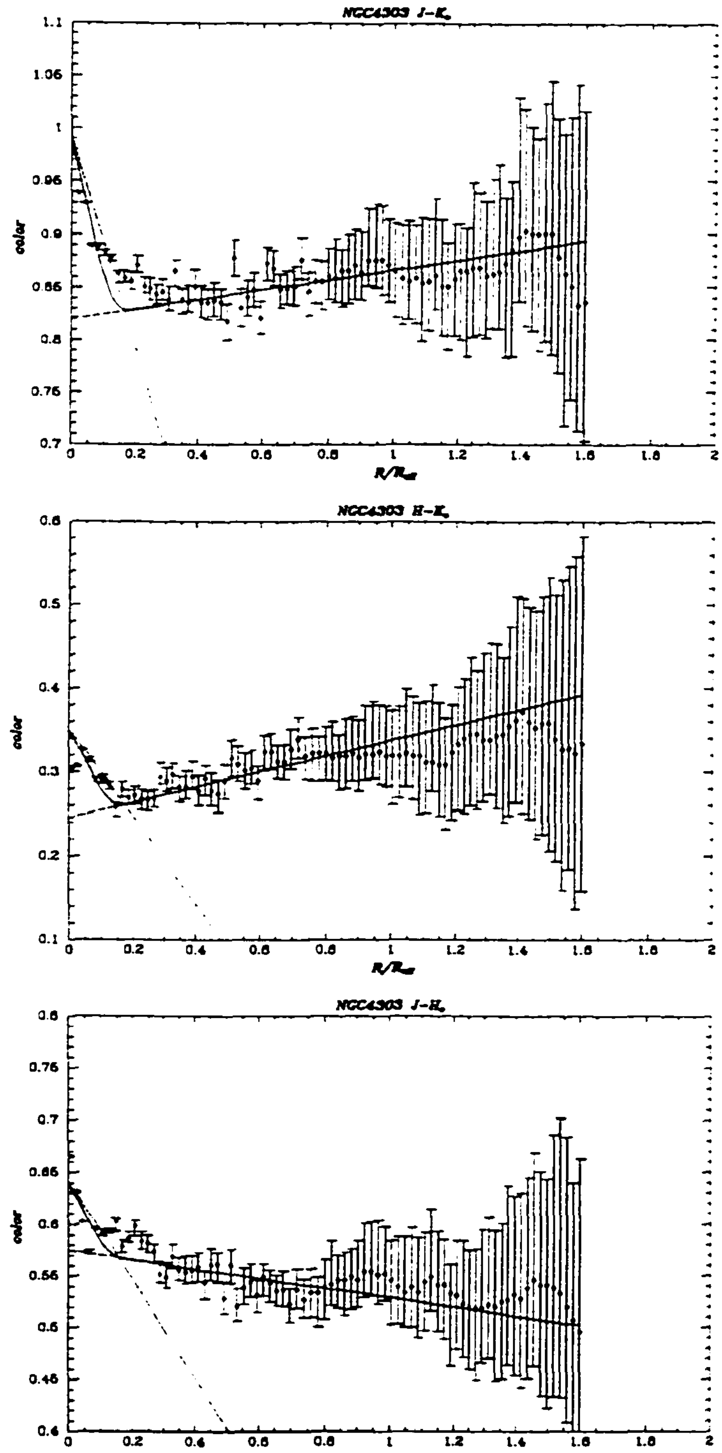

Fig. 4.3b.— NGC4303 - J-K, H-K, & J-H Color profiles. Description the same as Figure 4.3a.

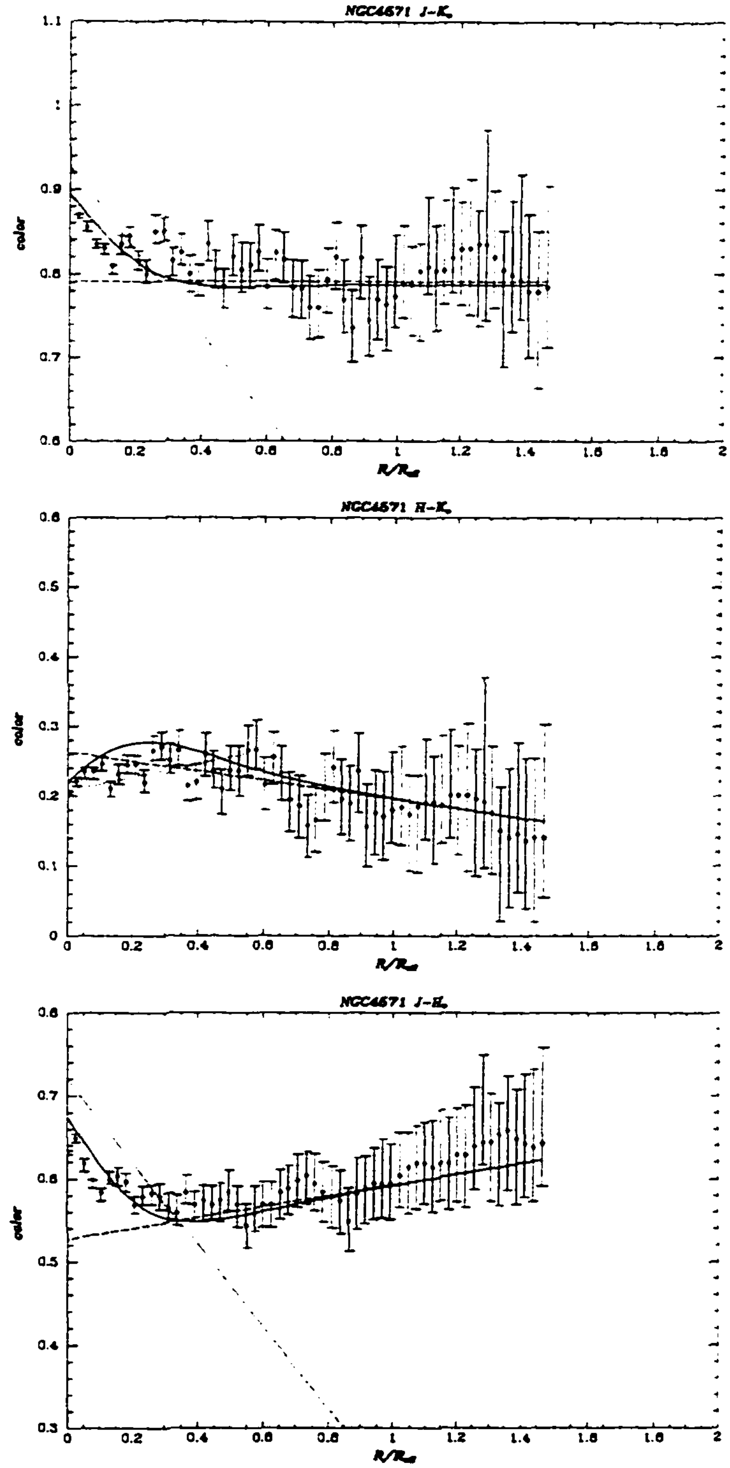

Fig. 4.3c.— NGC4571 - J-K, H-K, & J-H Color profiles. Description the same as Figure 4.3a.

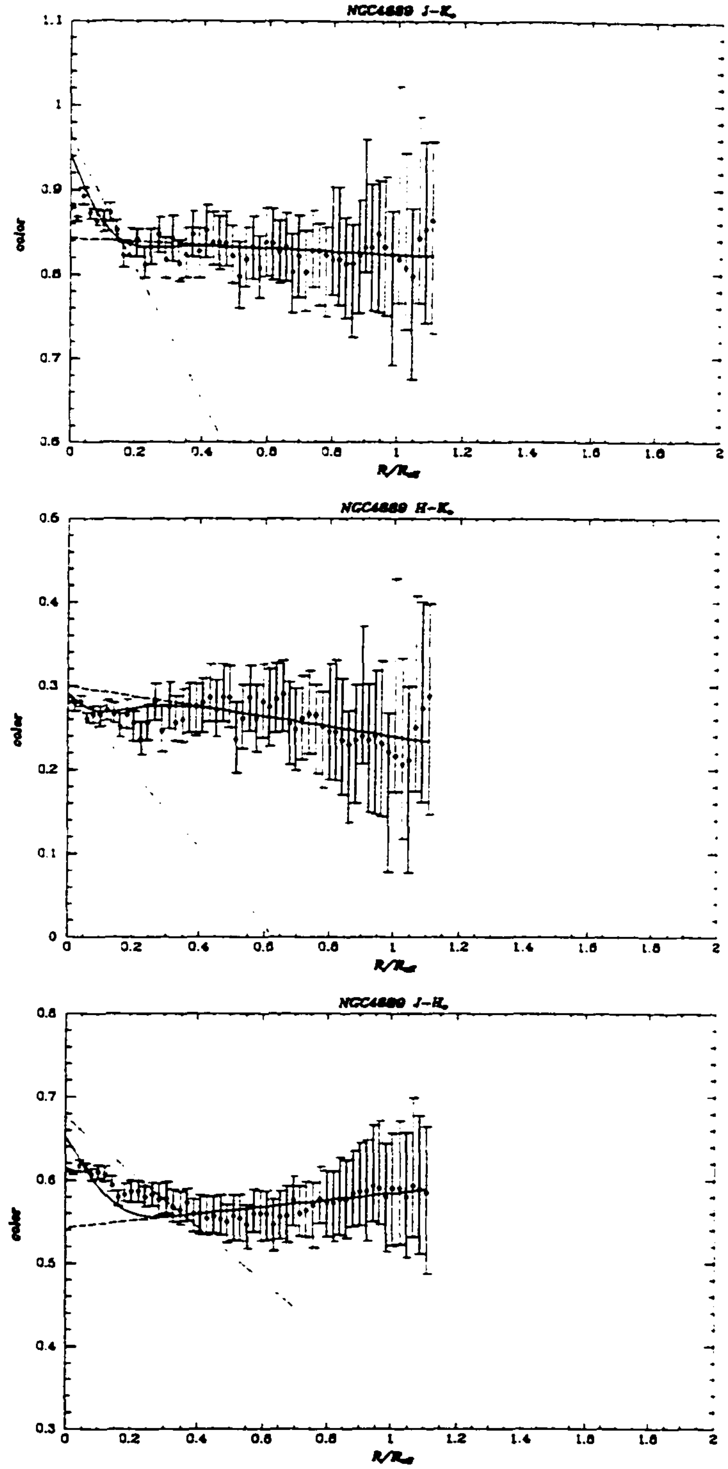

Fig. 4.3d.— NGC4689 - J-K, H-K, & J-H Color profiles. Description the same as Figure 4.3a.

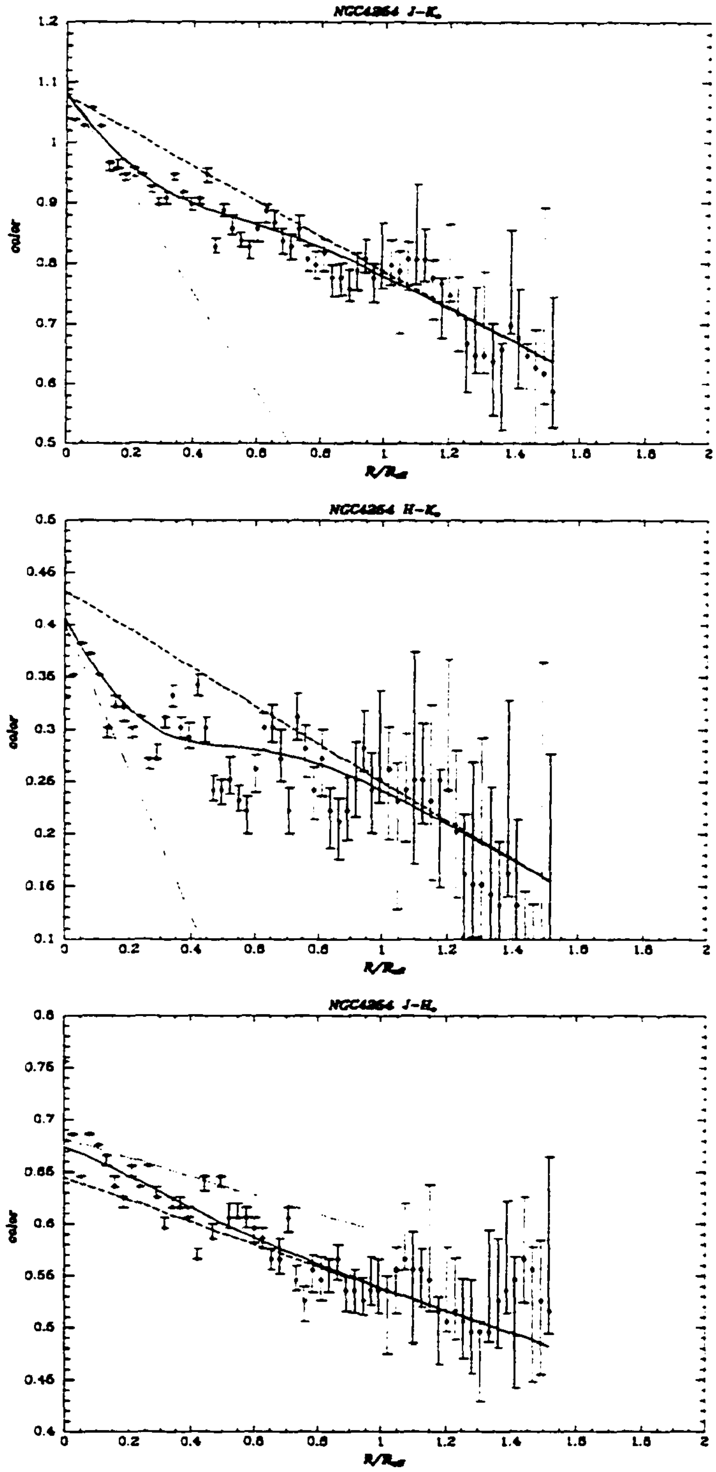

Fig. 4.3e.— NGC4254 - J-K, H-K, & J-H Color profiles. Description the same as Figure 4.3a.

examination of the galaxy images presented in figures A.1a to A.5a along with a comparison of the average profiles will allude to the contributions of the spiral arms and/or other structures to the 'bumpiness' of the profiles. The aim now is to discuss and probe the mean color behaviors rather than the intricate details. The intricate details of the NIR profiles can be explicitly seen in the 3-D magnitude plots. A.1b to A.5b. shown later where direct image to profile structures are clearly evident.

Another more interesting way to explore the color behaviors hidden within the profiles is to use the decompositions derived earlier to separate out the bulge and disk from one another and discover how they behave with color. Using Equation 4.1 for each of the separate J. H. & K channels we can derive analytical formulae from the deconvolved fits to give the fitted color behaviors of the separate spiral galaxy's structures. For instance. the fits derived for the bulge can lead to the following empirical color formulae for the bulge and disk which can then be compared to the observed data:

$$J - K = 1.44 + 2.5log\left(\frac{I_k}{I_j}\right) + 1.086r\left(\frac{1}{r_j} - \frac{1}{r_k}\right) + K_{j-k} \quad (4.24)$$

$$J - H = 0.36 + 2.5log\left(\frac{I_h}{I_j}\right) + 1.086r\left(\frac{1}{r_j} - \frac{1}{r_h}\right) + K_{j-h} \quad (4.25)$$

$$H - K = 1.08 + 2.5log\left(\frac{I_k}{I_h}\right) + 1.086r\left(\frac{1}{r_h} - \frac{1}{r_k}\right) + K_{h-k} \quad (4.26)$$

Where:

I_{jhk} is the respective bulge or disk central surface brightness fitting parameter.

r_{jhk} is the respective bulge or disk scale length fitting parameter.

K_{color} is the redshift K-correction for the NIR colors for each individual galaxy.

The redshift K-corrections are given by $K_{j-k} = -4.0z$, $K_{j-h} = -0.5z$, and $K_{h-k} = -3.5z$ with z being the galaxy's redshift. Even though the Virgo Cluster is nearby and any redshift correction will be small, it was deemed necessary to include the redshift color correction because of the small scale over which the color behaviors occur. The inclusion of the redshift correction also helped reduce the scatter of data points between the different galaxies because of the slightly different recessional velocities.

When looking at Figures 4.3a-4.3e it becomes apparent that there are two color behaviors, one of the bulge, the other the disk. Thus, the color behaviors of each galaxy component will be explored separately. The results of this color decomposition for the bulge and disk are given in Tables 4.4a and 4.4b.

Bulge Color Gradients

Galaxy	$\delta(J-K)$	$Int(J-K)$	$\delta(J-H)$	$Int(J-H)$	$\delta(H-K)$	$Int(H-K)$
NGC4321	-0.71	1.06	-0.45	0.69	-0.29	0.38
NGC4303	-1.00	0.99	-0.47	0.64	-0.53	0.35
NGC4571	-0.40	0.93	-0.50	0.72	+0.10	0.21
NGC4689	-0.79	0.97	-0.33	0.68	-0.46	0.29
NGC4254	-0.83	1.08	-0.13	0.68	-0.69	0.40

Slope given per R/R_{eff}

Table 4.4a: Bulge gradients with the associated intercept giving reddest bulge central color.

Disk Color Gradients

Galaxy	$\delta(J-K)$	$Int(J-K)$	$\delta(J-H)$	$Int(J-H)$	$\delta(H-K)$	$Int(H-K)$
NGC4321	-0.040	0.93	-0.037	0.60	-0.012	0.32
NGC4303	+0.046	0.82	-0.046	0.58	+0.092	0.25
NGC4571	-0.002	0.79	+0.065	0.53	-0.065	0.26
NGC4689	-0.020	0.84	+0.040	0.54	-0.061	0.30
NGC4254	-0.275	1.08	-0.107	0.65	-0.183	0.43

Slope given per R/R_{eff}

Table 4.4b: Disk gradients with the associated intercept giving reddest disk central color.

The fits to the color profiles derived above have been added to the color plots of the raw data, 4.3a to 4.3e. The filled circles represent the raw observed data points along the profile with the appropriate error bars introduced from the uncertainty in the residual sky subtraction. The dotted line follows the bulge color profile intensity fit while the dashed line follows the decomposed disk color fit. The combined color fits are the solid line. The effective radius, R_{eff}, is as defined in Table 3.1 (Kodaira 1986). Only those points with error bars less than about 0.2 magnitudes are plotted for only those really can definitively show any color behavior on this fine color scale.

It becomes fairly obvious in figures 4.3a to 4.3e that the color gradients of the bulge and disk are different. The disks have shallow color gradients that show nearly no color change while the bulges certainly show a gradient that does gets bluer radially outward. Individual gradients in the spirals are still both small enough however that no extreme changes in metallicity nor age is likely between the disk and bulge components of these late-type spirals. One can also notice that the overall color differences between spiral disks and bulges are small by inspecting Figures 4.3a to 4.3e. Only at the very central most regions of the bulge are the colors redder. Indeed this is at odds with what one expects if disks are largely bluer than bulges because there are no easily separable color behaviors between the individual disks and bulges, at least for the Near-IR observations in this study.

Color-color plots have been used to show as much information as possible in the plots, i.e. Figures 4.4a-4.4c. The plots also show colors internal and external to the full bulge radius from Table 4.3. In this way one can follow the separate color behaviors of bulges and disks as a group. Only by inspecting color-color plots can the general behavior of the all the bulge and disk colors between all of the spirals in J-K can be seen.

There are previous observations in the NIR for E, SO, and Sc galaxies with which to compare results. In Figure 4.4a, are the current results plus, for comparison, regions marked for aperture-photometry of globular clusters and Sc nuclei (Frogel 1985), elliptical galaxies (de Vaucouleurs & Longo 1988) and non-AGN spirals

(Véron-Cetty & Véron 1993). Regions occupied by field Sc bulges, ellipticals, and globular clusters are subjugated by dashed, dot-dashed, and dotted lines, respectively. The areas all represent integrated colors for the individual objects. The filled data points for the galaxy bulges represent the local colors internal to the bulge radius given in Table 4.3 while open data points represent the disk colors beyond those values. The plot shows that as a group these galaxy bulges do have a slightly tighter color behavior than the disk colors. However, there is no large scale separation between the colors, and no individual color behaviors of the individual galaxies can be seen. These Virgo spiral galaxies all seem to have somewhat bluer J-H colors while rather redder H-K than the field Sc bulges, ellipticals. The J-H colors are similar to the globular cluster values while much more red in H-K.

How do we interpret the implications of Figure 4.4a? Hunt et al. (1997) (and references therein) have nicely tabulated various theoretical mixtures of galaxy colors and nonstellar emission processes including HII regions, thermal dust emission, as well as intermediate age stellar A-type star populations, the effects of extinction, and the implications of various strengths of aged star burst colors upon the overall NIR colors. These models are also included in Figure 4.4a. The non-stellar effects of HII region emission on the NIR colors of galaxies are from Willner et al. (1972), Thuan (1983), and Sibille et al. (1974). The HII nebular emission line in Figure 4.4a shows tick marks which indicate fractional contribution to the K band in units of 0.2 relative to the galaxies contribution (Hunt et al. 1997). The line emission contribution from HII regions is negligible (Thuan 1983). NIR HII region colors arise principally from free-free emission of electrons in the Coulomb field of hydrogen and helium ions, the free-bound emission resulting from recombination of electrons onto excited states of hydrogen and helium ions, and from two-photon emission from transitions in HI. Extinction curves of Cardelli et al. (1989) along with the assumption that extinction behaves as an external screen are used to show the influence upon NIR colors with tick marks corresponding to unit increments of A_v. Hot dust was assumed to be optically thin and monochromatically approximated at 600 K by Wilson et al. (1972). Additional populations of any intermediate age A stars were assumed to have colors of 0.0. The stellar aged-burst line contains tick marks corresponding to order-of-magnitude increments in fractional contribution of the starburst component relative to the galaxy's and represents varying strengths of a starburst component at a post-starburst age of $3 \times 10^8 yr$ (Hunt et al. 1997). Finally, the dotted line beginning with the starred point represents a single post-starburst age of $10^7 yr$ of stars and the curve ends at $3 \times 10^8 yr$ where it coincides with the aged-burst line dominated by the starburst (Leitherer & Heckman 1995, Hunt et al. 1997). The placement of the theoretical tracks in the plot is arbitrary, they are only there to show the possible effects and influences on the galaxy colors from the respective structures.

Clearly, most of the local bulge and disk colors for the galaxy sample are bluer in J-H and redder in H-K than the integrated aperture photometry of the area marked for field Sc bulges from Frogel et al. (1985). Roughly constant J-H colors, together with red H-K, indicate hot dust while bluer than normal J-H and red H-K suggest nebular emission probably from HII regions (Hunt et al. 1997). Color-color diagrams enable us to discern colors associated with an intermediate-age population arising from a past star burst formation. Hunt et al. (1997) attribute H-K excess to hot dust in the system from recent and/or on going star formation. Virgo galaxies are often described as being redder than field galaxies (Kennicutt 1985) leading many to conclude that Virgo galaxies are more metal rich. NGC4254, NGC4321, and NGC4303 are often described as undergoing "prodigous" amounts of star formation in the spiral arms (Arsenault et al. 1988, Martin & Roy 1992, & Rauscher 1995) providing ample flux from large hot blue stars to light-up and create vigorous and bright HII regions. Cayatte et al. (1994) have classified the HI deficiency of NGC4303, NGC4254, NGC4321, NGC4571, and NGC4689 by 0.08, 0.17, 0.42, 0.44, 0.75, respectively.

The data points of Figure 4.4a have been size scaled inversely by HI deficiency. By careful consideration, the HI deficiency trend is captured in the color-color plot. As HI abundance increases from one galaxy to the next, all the data points of the bulge and disk for the respective galaxy moves blueward in J-H and redward in H-K paralleling the theoretical HII region contribution to the NIR line. Thus, it would seem that the prodigious star formation, especially in NGC4321 and NGC4303, are leading to some NIR contribution from HII region nebular emission, and that the near normal HI distribution in NGC4303 makes its disk points the bluest in J-H and reddest in H-K. Finally, since NGC4571 and NGC4689 have undergone the most HI stripping and have not experienced large scale star formation, they have nearly the most field Sc bulge-like colors.

Figure 4.4a includes the J-H and H-K colors of NGC4303's bulge, an average of some bright HII region colors, along with likewise average colors found in the intra-arm regions of the NIR images as a test to there being color dilution by nebular emission from HII regions and/or other mechanisms (three data points with error bars). HII region emission will increase with the amount of HI gas within the galaxy and from the greater availability of stars from star formation to photoionize the clouds. NGC4303's bulge colors show up as the reddest in J-H. The far left data point represents an average of a few intra-arm colors while the lower right is an average for some bright HII regions within NGC4303. Although the error bars are large, the same sense of blueward J-H and redward H-K is followed as HI abundance increases and NIR emission from HII regions becomes more important. Thus, it seems that HII region emission will produce a measureable and large enough shift in the overall NIR colors to skew stellar NIR colors. Likewise the colors of the bulge are reddened in the same sense as by either hot dust or greater extinction.

Some of the inner most bulge points in the galaxy may be redder because of hot thermal dust and an increase in extinction as alluded to in Figure 4.4a. These galaxies often get dustier as galactocentric distance decreases (Vila-Costas & Edmunds 1992. de Jong 1996. Balcells & Peletier 1994). Some of the NGC4321, NGC4303, and NGC4254 bulge points show this behavior by trailing up to the right in the figure. The inner most colors of the bulge points are most probably reddened by a combination of dust and metallicity.

Figure 4.4b includes the colors predicted by the single burst models of Worthey (1994). The points along each metallicity represent population ages of 8, 12, and 17 gigayears and the metallicities stretch from $[Fe/H] = -1.50$ to $[Fe/H] = -0.25$. The results for the galaxies are bluer in J-H, but run along to nearly the same extent over the J-K colors. It should be noted that the high metallicities models are needed to show the same range in J-K. This probably results because Worthey's single burst stellar models are attempting to model the stars of elliptical galaxy populations rather than disks and bulges of spiral Sc galaxies. It can also be noted that as a whole the bulge data points (filled) of these Virgo galaxies are redder in J-K than the disk data points (open). This plot also shows how NGC4571 and NGC4689 and, to some extent, NGC4254 colors are more like the Worthey (1994) single burst models for elliptical stellar distributions. These two galaxies are classified in this group as the most HI deficient and it seems that as the HI becomes more depleted at greater distances from the bulge the colors become more like those of ellipticals (also refer back to Figure 4.4a). It is interesting to note that both NGC4571 and NGC4689 also show a redward J-H profile, Table 4.4b and Figures 4.3c and 4.3d. Likewise, NGC4303 and NGC4254 have blueward J-H values in the Figures 4.3b and 4.3e as galactocentric distance increase and are the least HI deficient as well. This kind of J-H behavior in other galaxies may signal similar HI deficiency behaviors. The addition of significant HII region emission may be diluting the NIR color gradients in the stars of normal field galaxies. In fact, NGC 4303 which is the most like spirals in the field has a very shallow J-K gradient that moves redward far from the bulge.

The density of stars decreases outward from the galactic bulge so it is possible that the HII region emission may be contributing more than the stars in outskirsts of the spiral disks with vigorous star formation.

Finally. Figure 4.4c clearly shows that as a group the bulge points do appear redder in J-K than the disks. while in H-K the colors remain similar between bulge and disk. Any individual gradients for a respective galaxy that could even be seen in these plots if the behavior was large enough are lost in the general scatter of data. The delimited areas represent the galaxy bulge and disk colors with dashed and dotted lines. respectively. Most all the disk points are found below the dotted line while the bulge colors are above the dashed line. There is also a fairly large and broad area of comingled colors. so a large fraction of bulge and disk colors are very similar. It is only in the inner most regions of the bulges that some of the galaxies are redder in J-K than their individual respective disks (NGC4321. NGC4254) while others show very similar colors (NGC4303) on average. The figure shows that generally the bulges of the sample of spirals are in fact somewhat redder and the disks are bluer in J-K. while the other color plots reveal very similar J-H. H-K colors. Individual gradients in the respective galaxies are not large but the bulges as a whole have a steeper gradient than disks between all the observations. At least as a group. the bulges do appear redder in J-K than the disks. not by a tremendous amount. but which does imply some color behavior in J-K comparatively between spiral disks and bulges as a class. Perhaps this indicates that there is some NIR color sensitivity with metallicity implying that spiral bulges may be somewhat higher in metallicity than disks as a group of objects. but it is probably a combination of metallicity and dust.

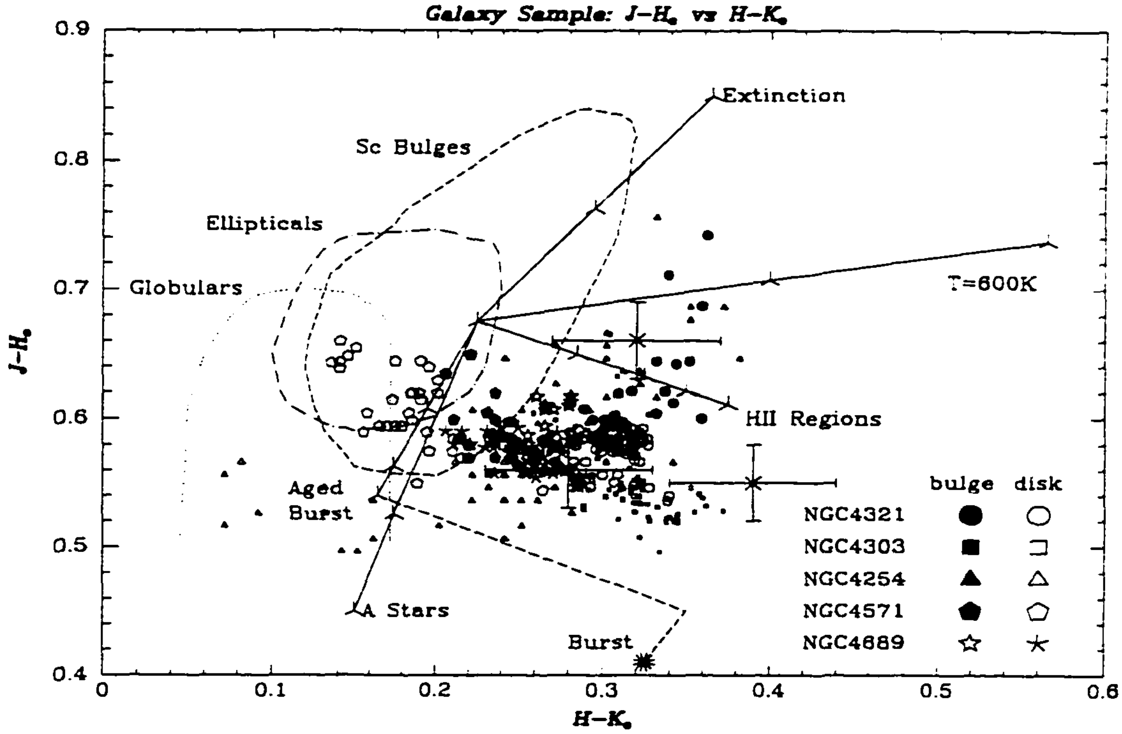

Fig. 4.4a.— (J-H) vs.(H-K). The dotted region marks integrated NIR aperture photometry of globular clusters, the dot-dashed marks the colors for ellipticals, while the dashed line region is integrated aperture photometry of Sc Type spiral bulges from Frogel (1985). All are field galaxy samples. The data points are the local NIR colors of the Virgo galaxy sample plotted versus each other and also denote galactocentric distance. Various theoretical mixes of galaxy colors and nonstellar emissions processes such as HII regions, hot thermal dust, extinction, a population of intermediate age A stars, and aged bursts from Hunt et al. (1997) where the tick marks along the lines mark the increasing contribution to the colors in addition to the galaxy's. Additionally, the sizes of the data points are scaled inversely to HI deficiency of the given galaxy as given by Cayette (1994). An average of a specific few NGC4303 intra-arm, bulge, and bright HII region colors are denoted by the data points with error bars. The lower right are specific HII region colors, upper central is representative of the bulge color, while the far left is a sample of intra-arm colors.

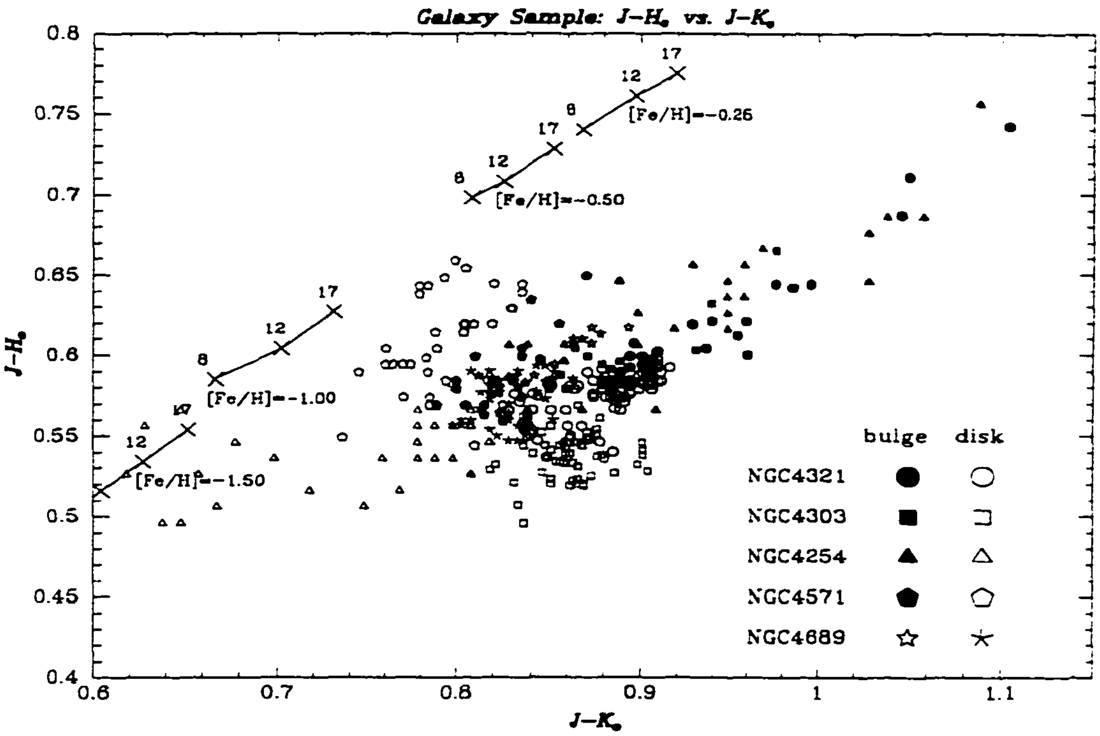

Fig. 4.4b.— (J-H) vs (J-K) plot. Single burst stellar models from Worthey (1994) with metallicities from [Fe/H]=-1.50 to [Fe/H]=-0.25 of single star formation bursts aged from 8 to 17 gigayears are included.

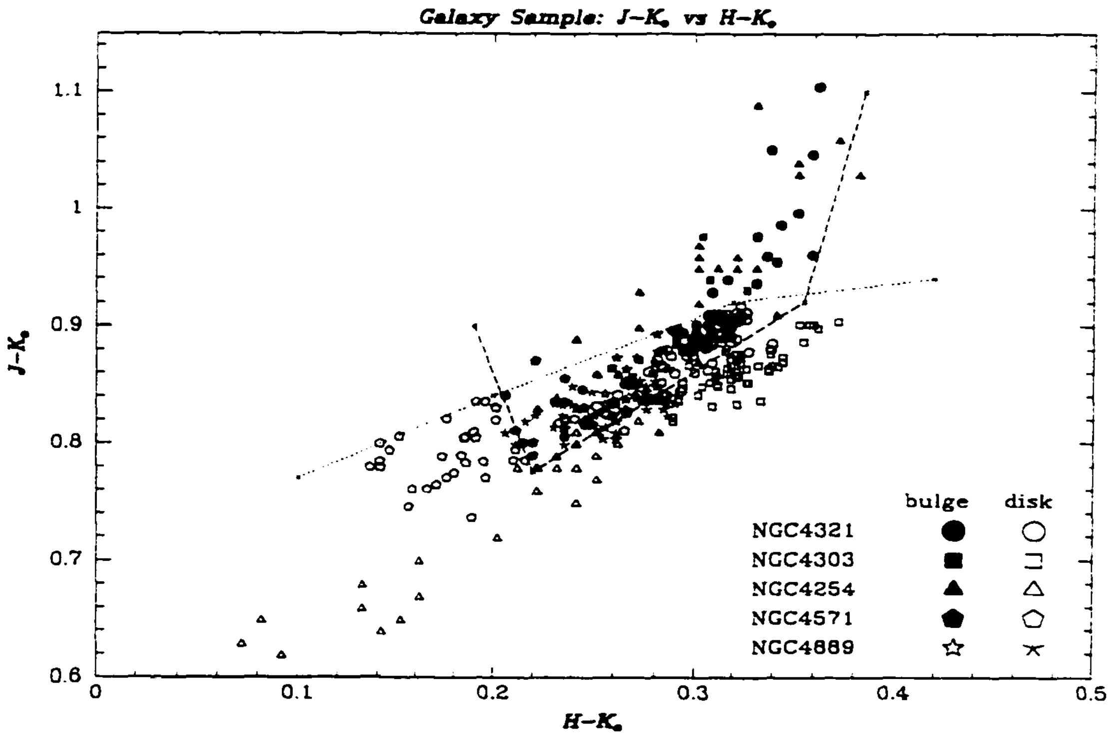

Fig. 4.4c.— (J-K) vs. (H-K) Plots. Notice that most bulge colors of the sample galaxies are redder in J-K and have a slightly steeper distribution while all the disk colors appear bluer with a more shallow distribution of points. The delimited areas represent the galaxy bulge and disk colors with dashed and dotted lines, respectively. Most all the disk points are found below the dotted line while the bulge colors are above the dashed line.

4. Virgo HII Region Abundance Gradients & J-K Color

Direct physical interpretation of color gradients within spiral galaxies can be based on two sets of observations: 1). The current star formation rate (SFR) as measured by the $H\alpha$ flux has a larger scale length than the underlying older stellar population (Ryder & Dopita 1994). There are relatively more young stars in the outer regions of spiral galaxies where active star forming regions are apparent in the bright spiral arms than in the central regions where large scale star formation has greatly slowed. This difference in stellar population should also be reflected in the color profile of spiral galaxies. 2). From metallicity measurements of HII regions it is known that there are abundance gradients as a function of galactocentric distance within the disks of spiral galaxies. Radial abundance gradients are a well known property of spiral galaxy disks (Searle 1971, Pagel & Edmunds 1981, Diaz 1989, Zaritsky et al. 1989, Scowen et al. 1992, and Henry & Howard 1995). Specifically, oxygen abundance decreases as galactocentric radius increases. If the metallicity gradients in the gas are also partly present in the stellar components, the effects might be observable in the NIR colors. Stellar population synthesis models incorporating both age, dust, and metallicity effects are needed in the comparisions with observations of radial color (de Jong 1996).

Using (J-K) as a metallicity indicator has been proposed by Aaronson et al. (1978), Frogel et al. (1985), and Worthey (1994) because the observed (J-K) index seems to increase in mean color with increasing metallicity while remaining somewhat insensitive to contributions from young stellar populations (Bothun et al. 1984, Vazdekis et al. 1996). To test the efficacy of using infrared (J-K) to approximately place boundaries on the stellar abundance gradients across spiral galaxies we are armed with the current color profiles found in this work as well as many previously calculated HII region gas abundance gradients of the same set of spirals (Henry et al. 1992, Henry et al. 1994, Skillman et al. 1996, Vila-Costas & Edmunds 1992). The following plots are an attempt to compare this work's observational results and HII region radial abundances with some theoretical stellar population models that predict similar color-metallicity (age) relationships.

Characteristic Oxygen Abundances and Gradients

Galaxy	Slope	Intercept	R_{eff}	Ref.
NGC4321	-0.17	9.27	83.4	(1)
NGC4321	-0.14	9.39	83.4	(2)
NGC4321	-0.27	9.26	83.4	(3)
NGC4303	-0.29	9.27	66.6	(1)
NGC4303	-0.39	9.54	66.6	(2)
NGC4303	-0.45	9.42	66.6	(3)
NGC4254	-0.26	9.35	52.2	(1)
NGC4254	-0.20	9.43	52.2	(2)
NGC4254	-0.22	9.33	52.2	(3)
NGC4571	-0.06	9.29	52.2	(2)
NGC4689	-0.19	9.42	66.6	(2)

Slope in dex per R/R_{eff}
(1). Vila-Costas & Edmunds (1992)
(2). Skillman et. al (1996)
(3). Henry et al. (1992)

Table 4.5: Abundance gradients from HII Regions over which the gradients were calculated.

Many models and theories on galaxy formation and their continued evolution predict gradients in metallicity abundances and in stellar populations, or some combination thereof (Matteucci 1989, Matteucci 1992, Kennicutt 1989, Dopita & Ryder 1994). Accordingly these gradients might lead to gradients in the colors of the stellar component in galaxies. Stellar effective temperatures are sensitive to metallicity because metals become dominant electron donors in the envelopes of stars and as a consequence the overall outer envelope opacity (Romanishin 1991). The envelope opacity determines the stellar radius and effective surface temperature, thus higher metallicity stars will have a lower (redder) surface temperature while lower metallicity stars will have a higher (bluer) surface temperature for a given luminosity (Bothun et al. 1984). So understanding the color structure and behaviors in galaxies may also be probing their metal content and stellar populations. The question is hard to decode, for both age and metallicity gradients can produce very similar color gradients. The color structure of the galaxy must also follow current ideas about how much colors are affected by either parameter.

What kind of color behavior might be expected? Spiral galaxies have two distinct components: the disk and the bulge. The stellar populations in these structures are also different. The bulge is dominated by older Population II stars and the disk is dominated by younger bluer Population I stars (Peletier & Balcells 1996). One must explore these differences to discover over what extent various population mixes can vary the color dynamics of the structure. There is also the variation on metallicity that can create color differences. Many galaxy evolution models have gradients that produce larger metallicities in the bulges of galaxies than in the outskirts. It is the subtleties of observation and theory that need to determine just how much more metal rich the bulges of spiral galaxies are compared to the disks. If dust is more concentrated inwardly then the bulge is also redder than the disk (de Jong 1996). At first hand, these ideas can lead to the decision that colors get bluer radially outward from the nucleus of a spiral galaxy without, necessarily, any conclusion on just how large the effects might be in any particular area of the spectrum and which parameter is affecting the colors the most or at all.

How can we attempt to untangle these behaviors? Large all-inclusive stellar population synthesis models have been used to investigate the effects of star formation history, stellar population age differences, dust content, and metallicity on the integrated colors of galaxies. (Tinsley 1980, Thuan 1983, Frogel 1985, Peletier 1989, Worthey 1994, Vazdekis et al. 1996, Peletier et al. 1994). What one needs are models that combine the effects on integrated light of the evolution of a stellar population with age and metallicity. Models such as these make use of standard isochrones of various metallicities and can help decipher the chemo-evolutionary changes of the stellar population as well as the intergrated light (Arimoto & Yoshii 1986, Worthey 1994, Vazdekis et al. 1996). The modeling techniques must start with some knowledge of, or assumptions about, initial mass functions (IMF): the initial distribution of stellar masses within the model galaxy, star formation history (SFH): the functional form if stars formed in the past, and the star formation rate (SFR) since that time. Finally, if one wants to produce a final spectrum for a model galaxy that has evolved in time, metallicity, and population mix, it must integrate over the isochrones in time the light of all the stars living at the current moment (Worthey 1994).

This study provides the unique opportunity to compare theoretical predictions of stellar population synthesis studies, the observations of stellar colors and their radial dependence in face-on spiral galaxies, and the radial abundance gradients in HII regions. Table 4.5 lists HII region abundance gradients found in the literature from Vila-Costas and Edmunds (1992), Henry (1992), and Skillman et al. (1996) showing the variation of $log(O/H) + 12$ verses radius with the associated gradient slope and maximum abundance intercept. These data can be used in unison with the data derived earlier for J-K versus radius for the same set of Virgo spirals to produce an observed J-K versus metallicity plot. Using $log(Z) = 1.42 + log(O/H)$ as described by Vila-Costas & Edmunds (1992) the J-K radial observations can be approximately calibrated. Remember that the HII abundances represent the gas component of the galaxy while the J-K measurements indicate primarily the old stellar population within the galaxy. Also, using $log(O/H)_{\odot} \simeq -3.08$ (Grevesse & Anders 1989) along with $[O/Fe] \simeq 0.3$ from stellar Population II studies (Wyse & Gilmore 1988) the O/H values can be transformed to [Fe/H] values.

Figures 4.6a to 4.6c show the results of this linking of HII oxygen abundance gradients (metallicity) to J-K colors in the stars. Figures 4.6a through 4.6c reflect the derived abundance gradients of Vila-Costas & Edmunds (1992), Skillman et al. (1996), and Henry (1992) respectively.

Why make such a comparison? One hopes that the abundances and metallicity that are indicative of the gas within a galaxy can give clues about the metallicity and possibly any gradients associated with the stars within the galaxy. All standard closed box models of spiral galaxies predict more metallicity within the gas of a galaxy than in the stars (Tinsley 1980). The gas is simply the more processed material in the galaxy while stars still hold onto more of the primordial mix of materials. This will especially be true for the older stellar population that dominates the NIR (Vazdekis et al. 1996, Worthey 1994). So by making this comparison one can deduce the maximum extent to which J-K colors may be linked to the metallicity within the stars and how the colors behave with abundance. However, if we are unlucky, it must be realized that the current gas metallicities in HII regions, and any functional form they might have, may be completely different from the underlying stellar component because processes such as metal enhanced star formation or infall of low abundance gas into the galaxy can dilute and/or reverse how J-K in the stars may scale with metallicity in the gas phase (Romanishin 1991).

This study is also a rare opportunity to compare theoretical stellar population synthesis models. The models of Worthey (1994) are based on a amalgamation of stellar evolutionary isochrones by VandenBerg (1995) and the Revised Yale Isochrones (Green et al. 1987) and use flux distribution libraries from theoretical stellar atmospheres. The models are calculated using the standard Salpeter IMF (Salpeter 1955), with lower mass cut off at $0.1M_{\odot}$ and upper limit of $2.0M_{\odot}$. The models are single-burst stellar populations of an initial metallicity, [Fe/H], that are then aged. The models of Vazdekis et al. (1996) also have single-age, single-metallicity stellar population models built in much the same way as Worthey (1994).

Metallicity	Z=0.008					I.M.F	I.M.F. Type
Color/Age (Gyr)	1	4	8	12	17	μ	Modes
(J-K)	0.83	0.85	0.87	0.85	0.84	1.35	Unimodal
	0.80	0.85	0.86	0.85	0.85	2.35	
(J-K)	0.83	0.85	0.87	0.93	0.82	1.35	Bimodal
	0.79	0.83	0.85	0.83	0.82	2.35	
	Z=0.02						
(J-K)	0.91	0.93	0.93	0.93	0.92	1.35	Unimodal
	0.87	0.91	0.92	0.92	0.91	2.35	
(J-K)	0.91	0.93	0.93	0.93	0.92	1.35	Bimodal
	0.86	0.91	0.91	0.92	0.91	2.35	
	Z=0.05						
(J-K)	0.97	1.04	1.00	0.98	0.95	1.35	Unimodal
	0.92	1.01	0.97	0.96	0.94	2.35	
(J-K)	0.98	1.05	1.00	0.98	0.95	1.35	Bimodal
	0.92	1.00	0.98	0.96	0.94	2.35	

Table 4.6a: Predicted J-K observables for single burst stellar population synthesis models by Vazdekis et al. (1996).

The models include a unimodal, Salpeter, IMF and a bimodal IMF that varies the initial masses of stellar types on different assumptions on the distribution of stars. Vazdekis et al. (1996) also includes models that combine evolutionary populations predictions with considerations of chemical evolution. These models follow the evolution of the gas and stars and make use of isochrones of more than one metallicity and assumptions about SFH, chemical yields, SNR, and SFR (Arimoto & Yoshii 1986).

SFR		$\nu = 1$		I.M.F. Type
Color/Age (Gyr)	4	10	17	Modes
Z	0.007	0.019	0.030	Unimodal
(J-K)	0.82	0.92	0.92	
Z	0.011	0.025	0.042	Bimodal
(J-K)	0.82	0.92	0.95	
		$\nu = 5$		
Z	0.036	0.076	0.084	Unimodal
(J-K)	0.94	0.95	0.93	
Z	0.049	0.102	0.121	Bimodal
(J-K)	0.95	0.97	0.94	
		$\nu = 10$		
Z	0.066	0.057	0.053	Unimodal
(J-K)	0.94	0.93	0.91	
Z	0.088	0.094	0.087	Bimodal
(J-K)	0.97	0.95	0.92	
		$\nu = 20$		
Z	0.075	0.058	0.042	Unimodal
(J-K)	0.94	0.92	0.91	
Z	0.106	0.088	0.068	Bimodal
(J-K)	0.96	0.94	0.91	
		$\nu = 50$		
Z	0.063	0.100	0.022	Unimodal
(J-K)	0.92	0.91	0.90	
Z	0.091	0.134	0.042	Bimodal
(J-K)	0.95	0.92	0.90	

Table 4.6b: Predicted J-K observables for a full stellar population synthesis models by Vazdekis et al. (1996). The model observables are for constant unimodel and bimodal IMF with $\mu = 1.35$. The SFR coefficient ν is in units of $10^{-4} M yr^{-1}$, while the age is in Gyr. Z indicates the metallicity obtained at the assumed populations age.

Color	Age (Gyr)			Metallicity
	8	12	17	Z
(J-K)	0.565	0.587	0.604	0.01
(J-K)	0.604	0.627	0.652	0.03
(J-K)	0.677	0.702	0.731	0.10

Table 4.6c: Predicted J-K observables for single burst stellar population synthesis models by Worthey et al. (1994).

Figures 4.6a to 4.6c include the various results of the single age-metallicity stellar population models of Worthey(1994) and the single burst and full chemo-evolutionary models of Vazdekis et al. (1996). The dotted boxed area marks all the models by Vazdekis et al. (1996) for single-burst populations while the dashed region is that of the Worthey (1994) synthesis models while Tables 4.6a to 4.6c have the range of the two different studies in J-K, Age, and Z. The full evolutionary models of Vazdekis et al. (1996) that follow a population with varying star formation rates are denoted by the dash-dot along with the appropriate values of age and star formation rate coefficient, ν, listed on the plots. The SFR coefficient, ν, will be large when the rate is vigorous. The galaxy surface NIR color data points follow the legends of Figure 4.4a. It is clear that there are definite differences between the color predictions for J-K of both models. Color and metallicity are partially untangled in the models of Vazdekis et al. (1996), but degenerate in those of Worthey (1994). The results of this study drive along slightly blueward of the two theoretical models of similar metallicity but show nearly the same behavior in J-K color and metallicity as the trends in the data and the theoretical models are similar. The oxygen abundance and gradients calculated by Vila-Costas & Edmunds match the best in color to the theoretical predictions while those of Skillman et al. (1996) being the most metal rich are the most blueward of the thoretical predictions for a given metallicity and observational color. However, the chemo-evolutionary synthesis models of Vazdekis et al. (1996) (marked in Figures 4.6a to 4.6c with dot-dashed lines) with a moderate star formation coefficient, $\nu = 10$, begin to match the colors and abundances predicted for the galaxies by Henry et al. (1992) and Vila-Costas & Edmunds (1992).

For comparison purposes, blue compact dwarf galaxies (BCDG) have been added to the $(J - K)$ vs.$log(O/H) + 12$ plots. The BCDG are all extremely metal deficient with respect to the solar neighborhood. Using the integrated NIR colors and metallicities from Thuan (1983), we can use the J-K BCDG colors and their respective low metallicities to see if the sense of the J-K trend with metallicity is similar. Figures 4.6a show that most of the BCDG colors, shown as half-filled circles with errorbars of 0.2 mag, are redder than the models of Worthey (1994) but that they again follow a similar trend of increasing metallicity and J-K in both stellar synthesis models and the NIR surface color data points for the Virgo cluster galaxy sample.

If the J-K index is truly sampling the same stellar population of K and M giants that are expected to dominate the NIR wavelengths then it is possible to calibrate the oxyen abundance gradients from HII regions within the disk to the J-K disk color gradients. Cautions do exist for this assertion. The NIR bands are thought to be sampling a mix of stars without large differences in ages. From the Worthey's (1994) models Giovanardi & Hunt (1996) have estimated that the stars will be no more than about 3 Gyr different in age for a change of .11 in J-K. Also, we must assume that any dust or HII region NIR color pollution is not a large enough factor to greatly alter any conclusions about the trends of metallicities contained within the galaxy disks from their respective J-K color profiles. So, we wish to use J-K as a nearly constant age, hopefully dust free, calibration of metallicity. It is unfortunate that

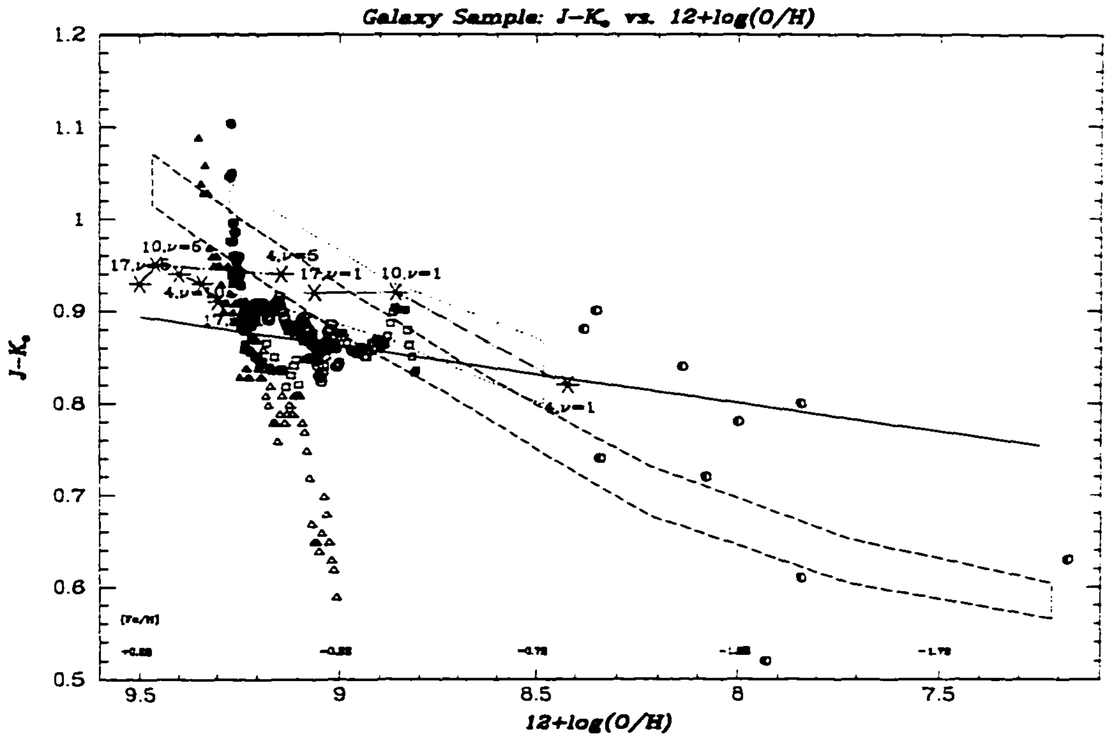

Fig. 4.6a.— (J-K) Color vs. 12+Log[O/H] Plot. The colors are those determined for the stars within the galaxy while the oxygen data are the HII region abundance gradients calculated by Vila-Costas & Edmunds (1992). The region delimited by the dotted area encompass the whole of Vazdekis et al. (1996) single burst stellar synthesis models while those of Worthey (1994) of 8-17Gyr is the region marked by dashes. Full chemo-evolutionary models produced by Vazdekis et al. (1996) are marked with dot-dashed lines with the appropriate ages in gigayears and the SFR coefficient listed. The larger the value for ν the more vigorous the rate of star formation. Filled data points are bulge points while open are disk values. In addition, NIR data for extremely metal poor blue compact dwarf galaxies (Thuan 1983) are represented by the half-moon data points. Typical errors for the local galaxy color data is less than 0.2mag in J-K, while for the BCDGs is on order of 0.2mag. The solid line is the best fit J-K to metallicity calibration of the disk color gradients to HII region oxygen abundance gradients for all galaxies.

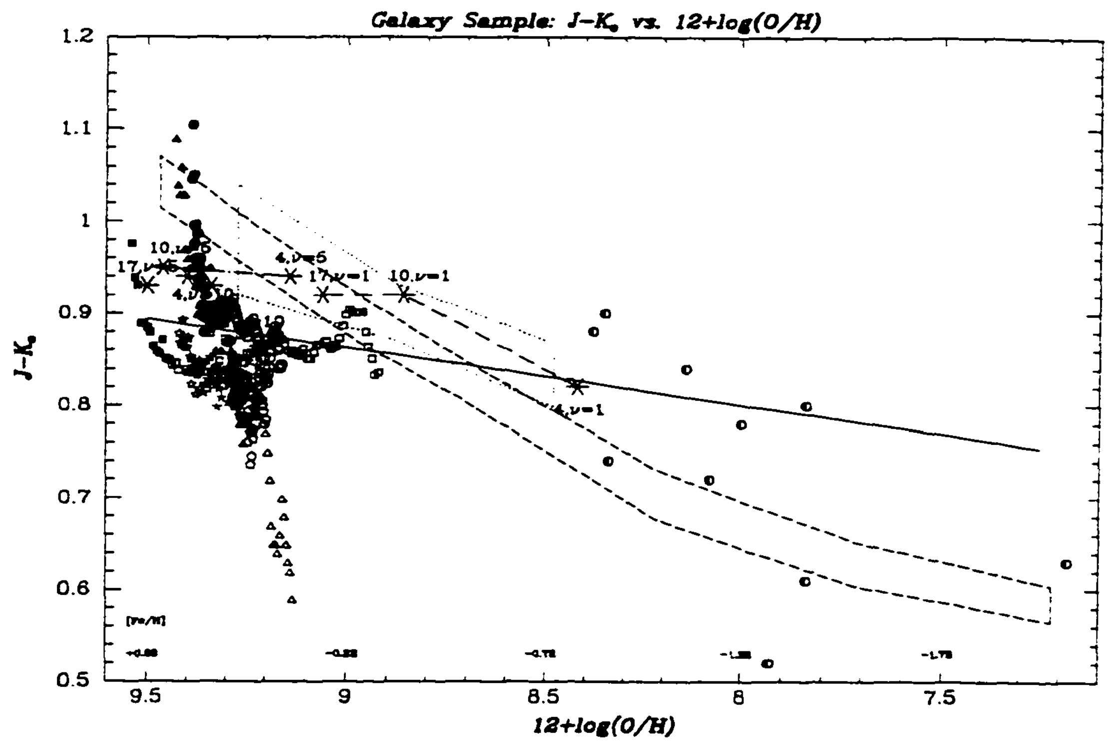

Fig. 4.6b.— (J-K) Color vs. 12+Log[O/H] Plot. The colors are those determined for the stars within the galaxy while the oxygen data are the HII region abundance gradients calculated by Skillman et al. (1996). Data point description is the same as Firgure 4.6a.

the scale of the J-K color gradients is rather shallow making the untangling of these degenerate effects a very desperate problem (Vazdekis et al. 1996).

The HII region abundance gradients in Table 4.5 and the disk J-K color gradients in Table 4.4b can be used to fit the observed trend of somewhat redder J-K with increasing oxygen abundance. Already there is a hint that an empirical calibration might be possible because the oxygen gradient for NGC4571 and NGC4689 are among the shallowest as is their respective J-K gradients in the disk component. The fits for the individual galaxies applying the NIR disk J-K gradients and oxygen abundance yields:

$$NGC4321 : (J-K) = +0.223(\pm0.06)(log(O/H)+12) - 1.15(\pm0.54) \quad (4.27)$$

$$NGC4303 : (J-K) = -0.126(\pm0.03)(log(O/H)+12) + 2.12(\pm0.22) \quad (4.28)$$

$$NGC4571 : (J-K) = +0.035(\pm0.07)(log(O/H)+12) + 0.62(\pm0.50) \quad (4.29)$$

$$NGC4689 : (J-K) = +0.108(\pm0.07)(log(O/H)+12) - 0.06(\pm0.50) \quad (4.30)$$

$$NGC4254 : (J-K) = +1.23(\pm0.15)(log(O/H)+12) - 10.58(\pm1.26) \quad (4.31)$$

with a fairly large scatter of slopes and the very large slope calculated for NGC4254. The slope for NGC4254 is very uncertain because of poor data aquisition of one poor image. Further calculations do not include NGC4254 until such a time that more data can be obtained and the large gradient can be verified, but the data points up until now have been included for comparison purposes. The fits of NGC4321, NGC4303, and NGC4254 are averages of the three different HII region oxygen abundance results of Skillman et al. (1996), Vila-Costas & Edmunds (1992) and Henry et al. (1992) while those of NGC4689 and NGC4571 are derived solely from Skillman et al (1996). It is obvious at this point that the individual calibrations of stellar J-K to spiral disk oxygen abundance in HII regions for each respective galaxy are widely scattered with varying trends and intercepts. The large scatter in the fits only adds more

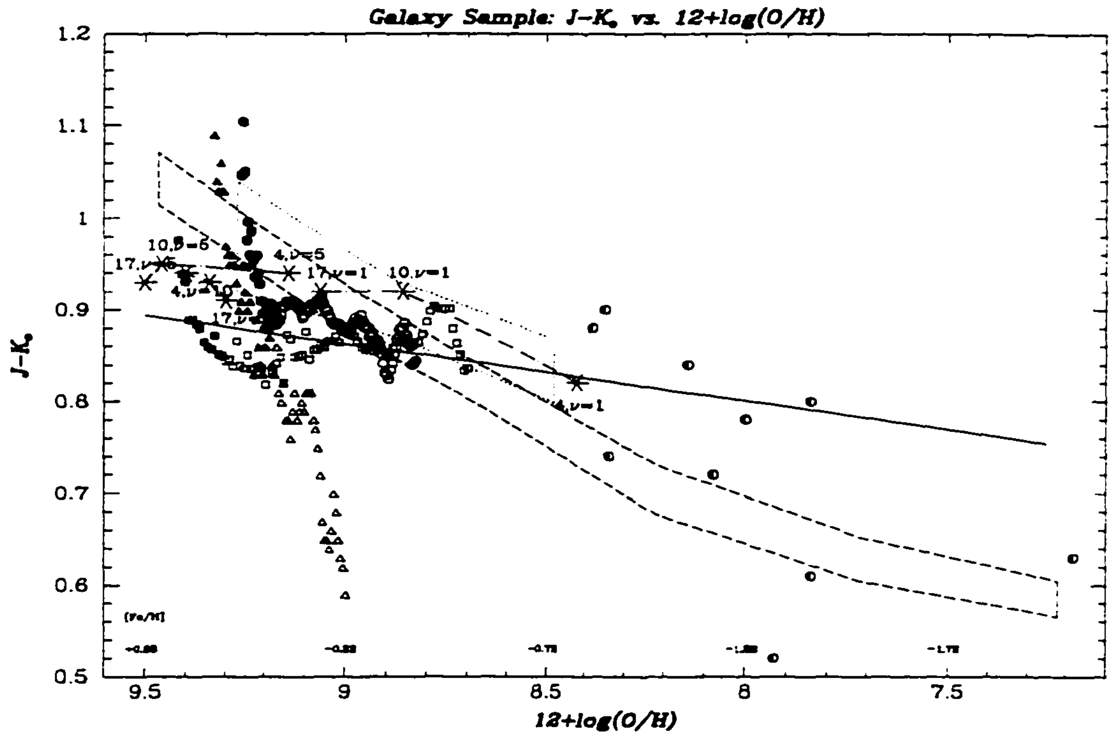

Fig. 4.6c.— (J-K) Color vs. 12+Log[O/H] Plot. The colors are those determined for the stars within the galaxy while the oxygen data are the HII region abundance gradients calculated by Henry et al. (1996). The areas are marked off the same as described in Fig. 4.6a.

complication and casts doubt upon a firm metallicity calibration. However, using the various slopes and intercepts of the galaxies as a group the averaged fit (excluding NGC4254) to the data gives:

$$(J - K) = 0.06(\pm 0.12)(log(O/H) + 12) + 0.32(\pm 1.2) \tag{4.32}$$

And if we use $log(O/H)_{\odot} \simeq -3.08$ along with $[O/Fe] \simeq 0.3$ the O/H values can be transformed to [Fe/H] values and a similar relations for [Fe/H] can be obtained.

$$(J - K) = 0.06(\pm 0.12)([Fe/H]) + 0.88(\pm 1.2) \tag{4.33}$$

The fit to Equation 4.32 has been added to the plots of 4.6a to 4.6c with a solid line in each plot showing the calibration. The fit is more shallow than the theoretical population synthesis models but follows the spiral galaxy disk J-K colors well. The line also follows the reddest and most metal rich BCDGs well. The fit does not match the bluest BCDGs. Clearly, the errors for the calibration are larger than the calibration values which is a strong indication that J-K is not a strong metallicity indicator over the observed abudances within the HII regions of the repective disks, so this calibration should be regarded as highly suspect. The large scatter in J-K color gradients must be coming from a host of influences and not just metallicity.

How can we compare this empirical calibration? The NIR BCDGs observations by Thuan (1983) that are shown in the figures have a similar calibration of integrated colors of $(J - K) = 0.20(\pm 0.07)([Fe/H]) + 0.92(\pm 0.10)$ and Aaronson et al. (1978) arrive at a similar result for globular clusters and early-type galaxies of $(J - K) = 0.14(\pm 0.02)([Fe/H]) + 0.85(\pm 0.04)$. In fact, if the BCDG NIR colors are included with the disk J-K gradients of the Virgo galaxy sample then it yields a very close $(J - K) = 0.13([Fe/H]) + 0.88$ emipircal calibration. Unfortunately, the error bars for all the BCDG data points are large, 0.2 mag, compared to the

J-K gradients that may be revealed, so these calibrations also have a large enough scatter that a color calibration can be lost. Again, J-K fails to show a strong enough influence to definitively state that it scales well enough with abundance.

Author	Calibrating Relation	Held Constant
Vazdekis	$\delta(J-K)/\delta(log(z)) = 0.17$	Age
Vazdekis	$\delta(J-K)/\delta(log(t)) = -0.06$	Z
Worthey	$\delta(J-K)/\delta(log(z)) = 0.29$	Age
Worthey	$\delta(J-K)/\delta(log(t)) = 0.16$	Z

Table 4.7: Chemo-evolutionary stellar population model results trying to separate the effects upon the integrated colors of galaxies by metallicity and stellar age mixes (Vazdekis et al. 1996 and Worthey et al. 1994).

We can also compare the J-K verses metallicity calibration results of the theoretical stellar population synthesis models of Worthey (1994) and Vazdekis et al. (1996). Table 4.7 has the results of how J-K varies with metallicity for each theoretical model if the age of the population of stars is held constant and likewise shows the variation of stellar ages if one assumes a constant metallicity. Unfortunately, the theoretical models show that J-K can vary with metallicity and age within nearly the same scales, thus one influence can mask the other in NIR colors. The models reveal that J-K is not immune to changes in the stellar age differences between stars. In the calibration of this paper we have assumed that the stars the NIR picks out in the disk are close enough (same) in age that they would not influence the J-K adequately to wash-out the metallicity determinations, but this is not entirely the case. Additionally, the color-color plots reveal that the inner-most bulge points redden a great deal. This reddening is a probable consequence of increased dustiness and/or metallicity of the bulge, thus driving the colors red as compared to the bulge. HII region continuum emission may shift the NIR colors depending on the amount of star formation and amount of HI deficiency, refer back to figure 4.4a. The NIR J-K color index in these spiral galaxies does not appear to correlate strongly enough to singly separate out only the metallicity in the stellar component as the only influence in color or any associated gradients. The effect is just too small and possible complications too large.

5. NIR Color Summary

Observed J-K color gradients have been obtained for a handful of five Virgo cluster late-type spirals and compared to theoretical predictions for NIR colors from stellar population synthesis models in an attempt to test the efficacy of using the J-K index as a strong stellar metallicity indicator as has been proposed by Bothun et al. (1984). For the most part, variations in the mechanisms that can lead to the production of NIR colors gradients such as stellar age mixes, a variation in dust, and the possible dilution of stellar colors by other non-stellar emission processes, make the firm calibration of J-K to metallicity impossible. This is in agreement with studies done by Hunt et al. (1997) and Peletier & Balcells (1996) which found very small color differences in and between spiral bulges and disks, but disagrees with Bothun & Gregg (1990) who found larger color variation.

Specifically, results show that, the amount of HI stripping correlates with observed NIR colors. Nebular emission from bright HII regions in the spiral galaxies has a measureable effect on the overall observed colors, which will tend to partially interfere with any NIR stellar colors. It appears that when there is more gas (NGC4303,NGC4254,NGC4321), there is more star formation, which in turn can produce colors that are not entirely related to the old stellar component that was expected to more strongly dominate the NIR wavelengths. This result is also more likely the case in the complex environment of spiral disks than in elliptical galaxies where the NIR may be more free of other NIR sources. In addition, the colors in the bulges are altered further most likely because of higher dust concentration thus higher extinction in the bulges. It is interesting to note that in the galaxies that are described as the most HI stripped (NGC4571,NGC4689), thus more elliptical like in gas content, the NIR colors become more similar. Bulge NIR color differences are probably a result of some metallicity difference between it and the spiral disk, along with increased extinction and reddening from dust and/or hot thermal emission. The spiral disk does have a shallow J-K gradient that can probably best be explained by a combination of metallicity and age gradients based on observational and theoretical colors which in turn itself may be further influenced by the amount of HI deficiency and vigorous star formation that is occuring in the disk. Since we can not be sure as to the specific source of NIR luminosity, especially in the spiral disks where a color to abundance linkage is attempted, a strong calibration between J-K and mean stellar metallicity is lost.

The main conclusion of this section is that, consistently from the color-color and the HII region oxygen abundance comparisons, the J-K NIR index can not be confidently used by itself as a stellar metallicity measure in these late-type Virgo spirals. The J-K index does not have enough wavelength leverage to separate out the influence of metallicity caused stellar NIR colors from the similar effects upon these colors by other physical processes and population variations within these late-type spiral galaxies.

Chapter 5

Conclusions & Summary

This thesis came in two distinct flavors: 1). The study of HPNe and their respective physical and chemical properties, and 2). The exploration of spiral galaxy properties and chemistry using NIR surface photometry and HII region abundance gradients in the disks. The major conclusions of this work are:

1. Halo Planetary Nebulae

1. Relative to the sun, all nine HPNe objects show subsolar O/H, most show enhanced C/O (except DdDm-1 & Pn243.8-37.1) and N/O (except NGC2242 & K648), and seven of the nine show a relatively constant value for Ne/O.

2. The HPNe Ar/O hints at the possibility of two differing groups. There are those HPNe that are extremely Ar poor (H4-1, K468, & BB-1) and those which are not.

3. All chemical trends are reasonably consistent with current nucleosynthesis ideas relevant to intermediate mass stars.

4. The results of the photoionization models for the HPNe show that nebular emission line strengths are relatively *insensitive* to the atmospheric details of the central white drawf star. Thus, using a blackbody spectrum is quite suitable and representative of the central stars continuum.

HPNe show more abundance scatter than disk PNe, implying that abundances were less homogeneous in the halo at the time of the progenitor formation and/or possibly less thorough mixing occured in the galaxy halo.

2. NIR Photometry of Virgo Spiral Galaxies

1. There is good agreement between the masses and luminosities that the intensity decomposition techniques determine in this study to previous results. Plus, physical parameters have been calculated for two galaxies for the first time (NGC4571 and NGC4689).

2. The NIR mass-to-light ratios do hint at some variation with metallicity. Theoretical stellar population synthesis models imply that metallicity increases as M/L decreases. The observational results for the sample Virgo cluster spirals leads to a similar conclusion when comparing to the NIR color behavior in J, H, & K to mass-to-light ratios.

3. Bulge NIR colors and any color gradients are probably a direct result of combinations of metallicity and dust, while disk colors are probably less affected by dust and more influenced by HI decificiency and current levels of star formation. The Virgo cluster environment may actually affect the observed J-K colors in individual galaxies.

4. The J-K vs. Metallicity calibration determined for the disk colors along with HII region abundances is more shallow than those derived for integrated colors of ellipticals, globular clusters, and blue compact dwarf galaxies. The errors cited for many previous studies are nearly as large as the gradients that are identified. The errors for the disk J-K colors in this study are below 0.2 mag. But, this still falls short of providing a strong NIR to metallicity measure.

5. Color-color studies show that NIR colors of the old stellar component can be measureably influenced by other non-stellar affects such as nebular emission and extinction, the amount of HI gas within the galaxies, and variations of stellar age within the stars. This prevents a strong observational non-degenerate calibration of metallicity to the J-K index because there is no firm reason to believe the color gradients are the sole result of metallicity content within the stars. In addition, HI deficiency trends are captured in the color-color plots, as deficiency increases the NIR colors become more elliptical-like.

6. In the complex, flocculent, and dynamic structures of spiral type Sc galaxies the NIR J-K index does not have enough wavelength "leverage" to untangle the color effects of stellar ages, dust contribution, and other non-stellar NIR emissions from the influences that metallicity has upon colors. J-K vs. metallicity cannot be sufficiently calibrated.

Appendix A

Images, Contours, and Profiles

This appendix contains the NIR J, H, & K blanked images and contour plots that were used to help analyze the data within this thesis. The image plates are listed from top to bottom in order from J, H, to K image. Also, directly after these images are three dimensional surface-brightness profiles for each galaxy. The more complex detail discussed for each galaxy refer to these more involved 3-d profiles. Specifically, one can see that all the NIR passbands do also trace the spiral structure of the galaxies including bulges, bars, disks, and spiral arms.

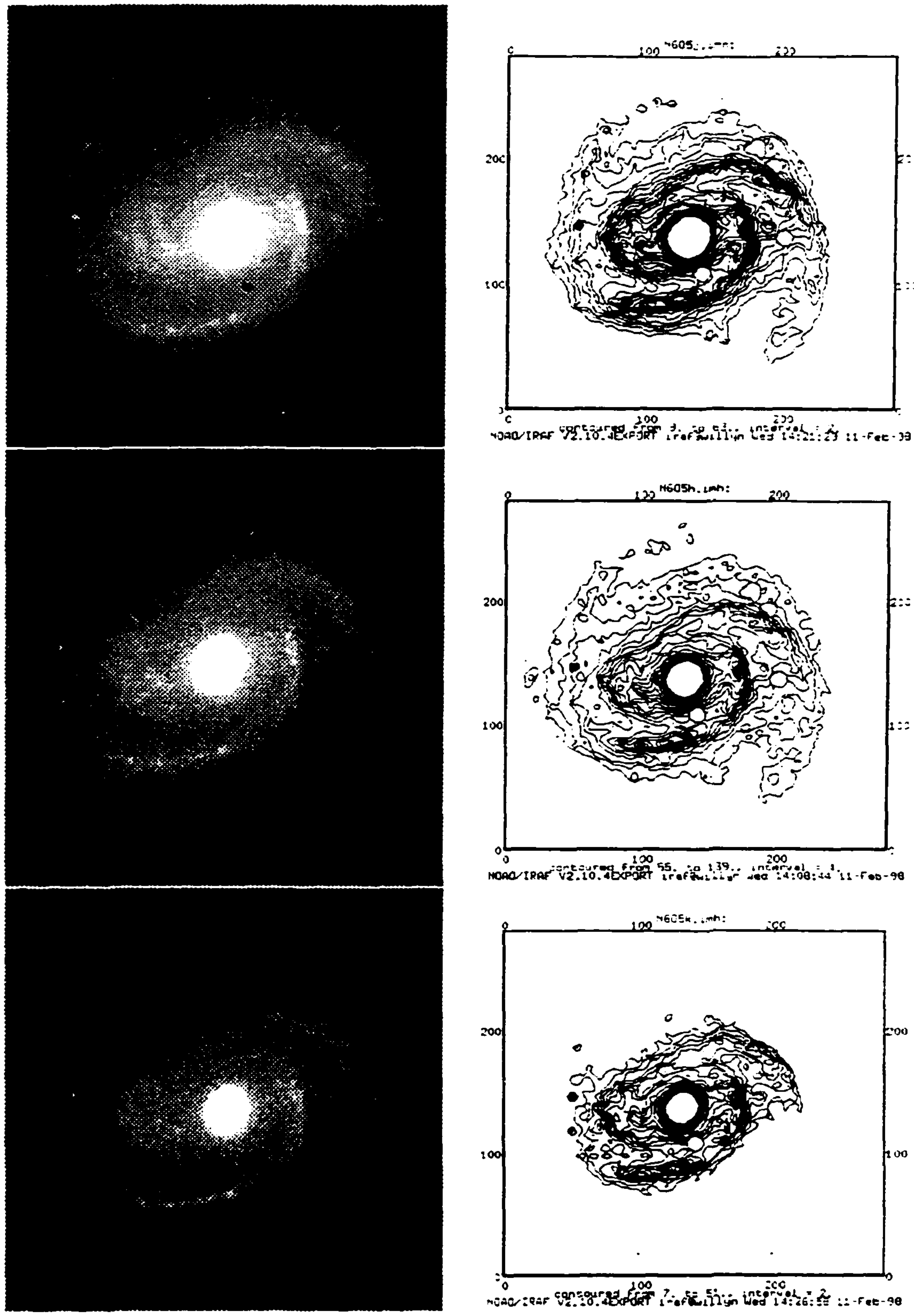

Fig. A.1a.— NGC4321 - J,H, and K Image and respective contour.

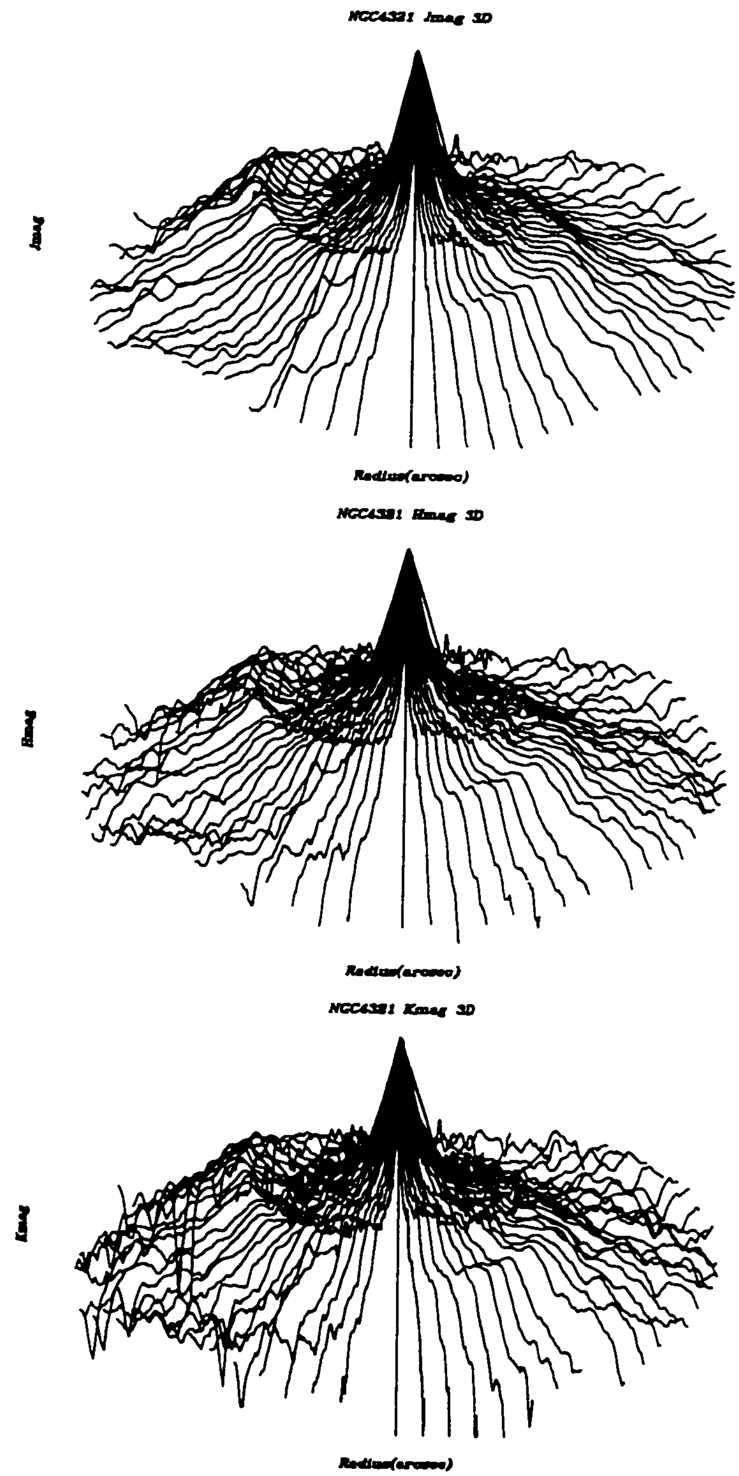

Fig. A.1b.— NGC4321 - J,H, and K 3-D Profiles.

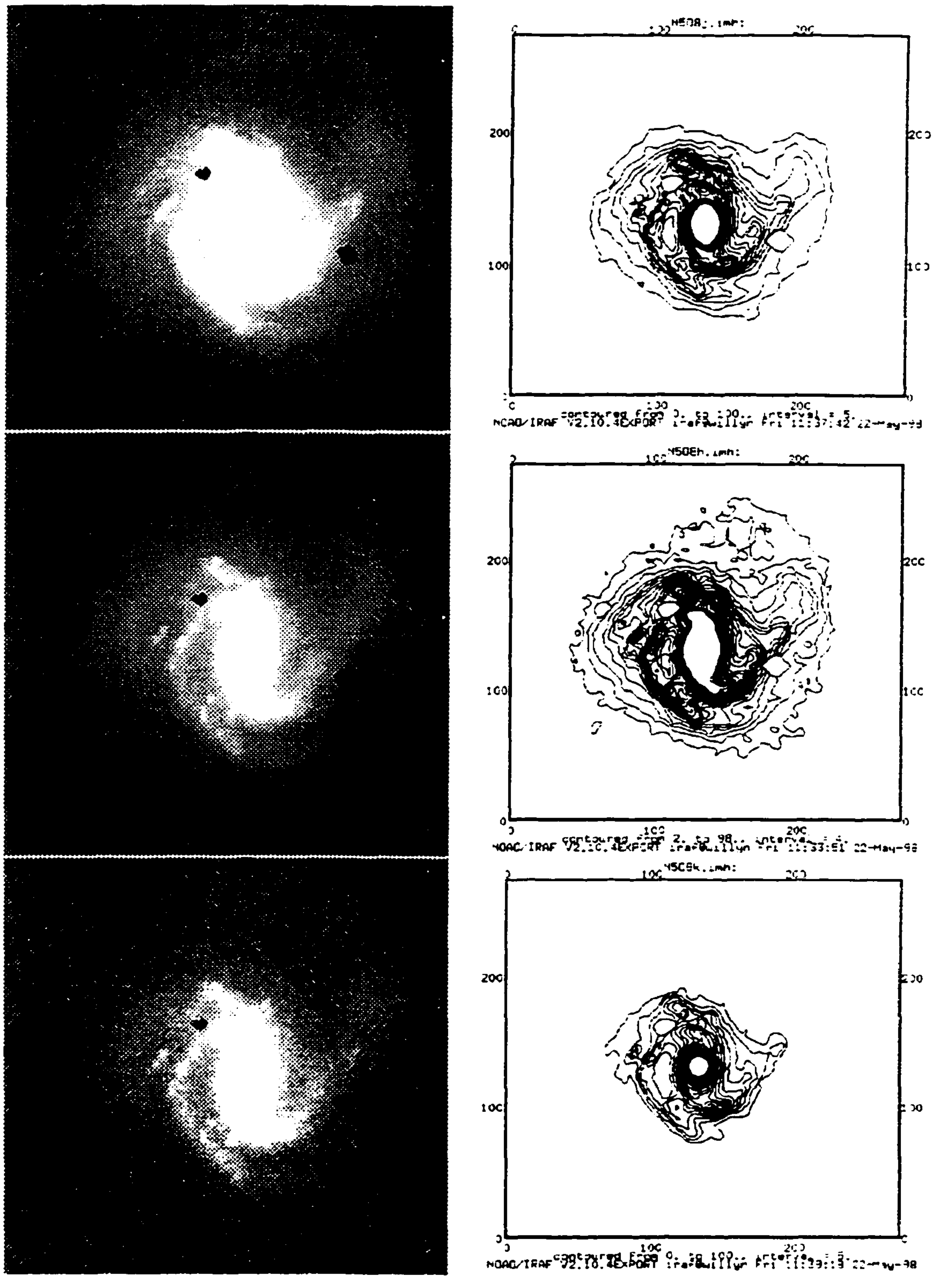

Fig. A.2a.— NGC4303 - J,H, and K Image and respective contour.

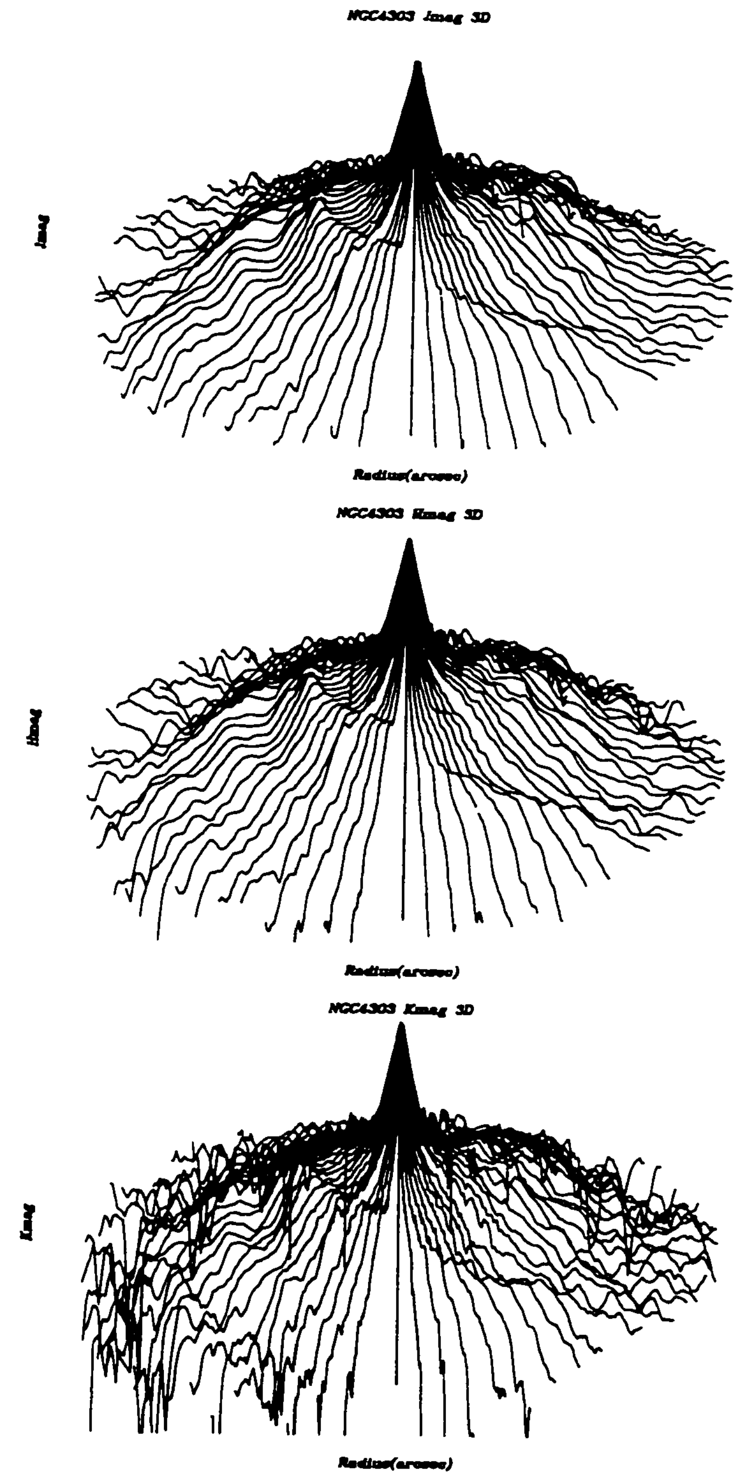

Fig. A.2b.— NGC4303 - J,H, and K 3-D Profiles.

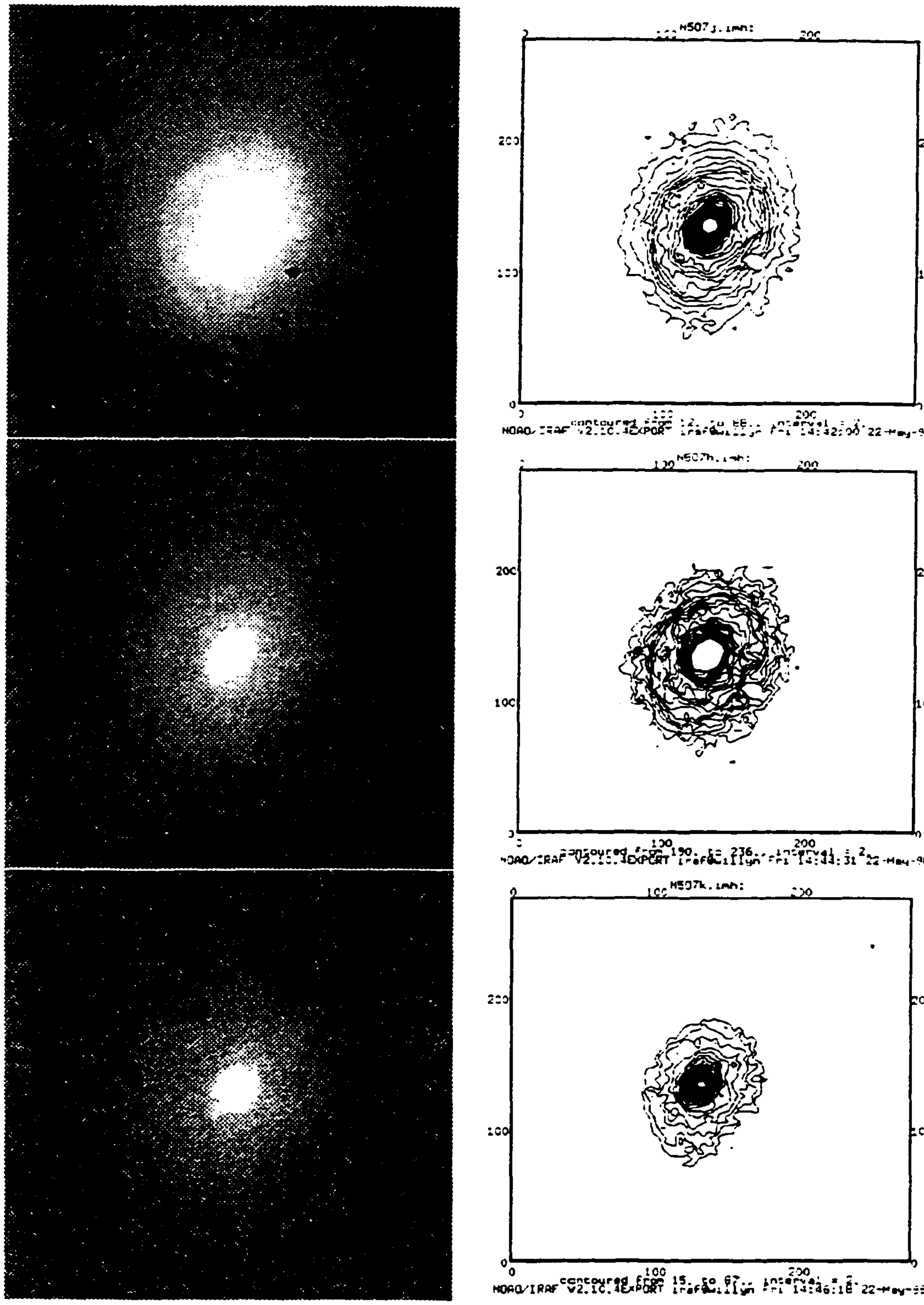

Fig. A.3a.— NGC4689 - J,H, and K Image and respective contour.

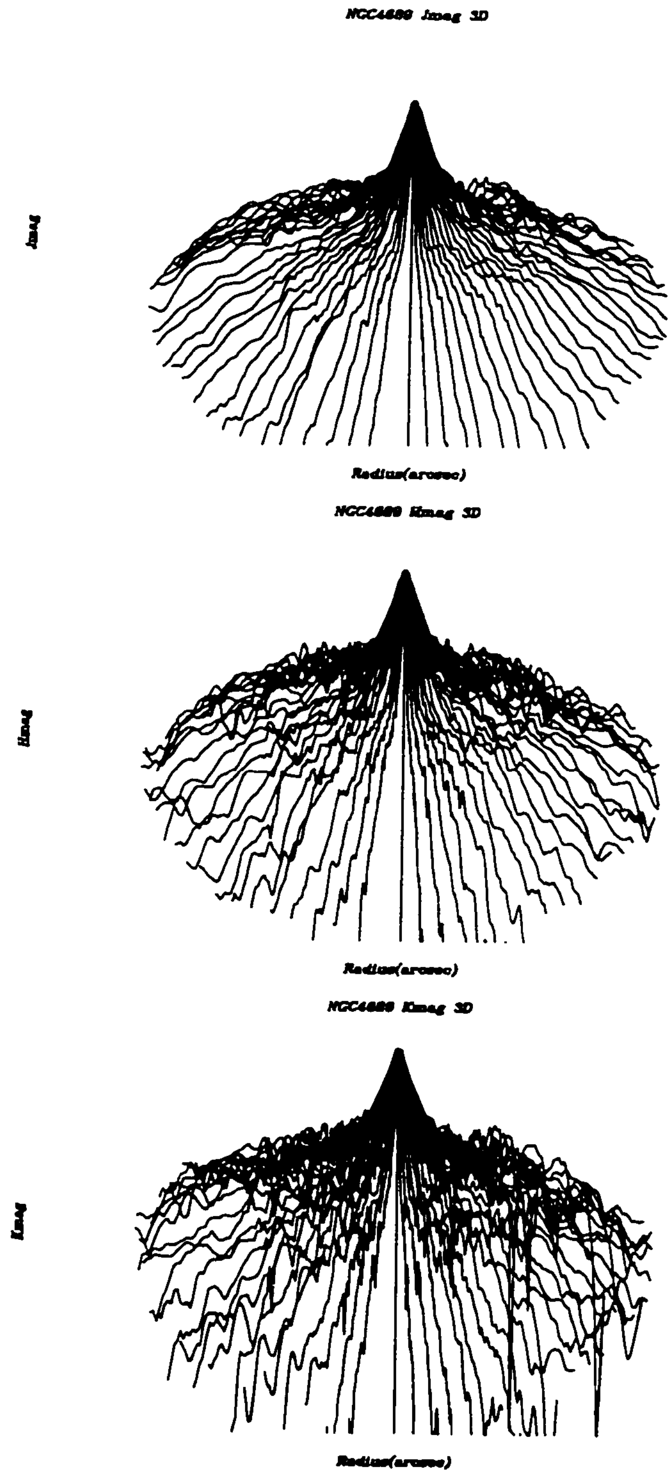

Fig. A.3b.— NGC4689 - J,H, and K 3-D Profiles.

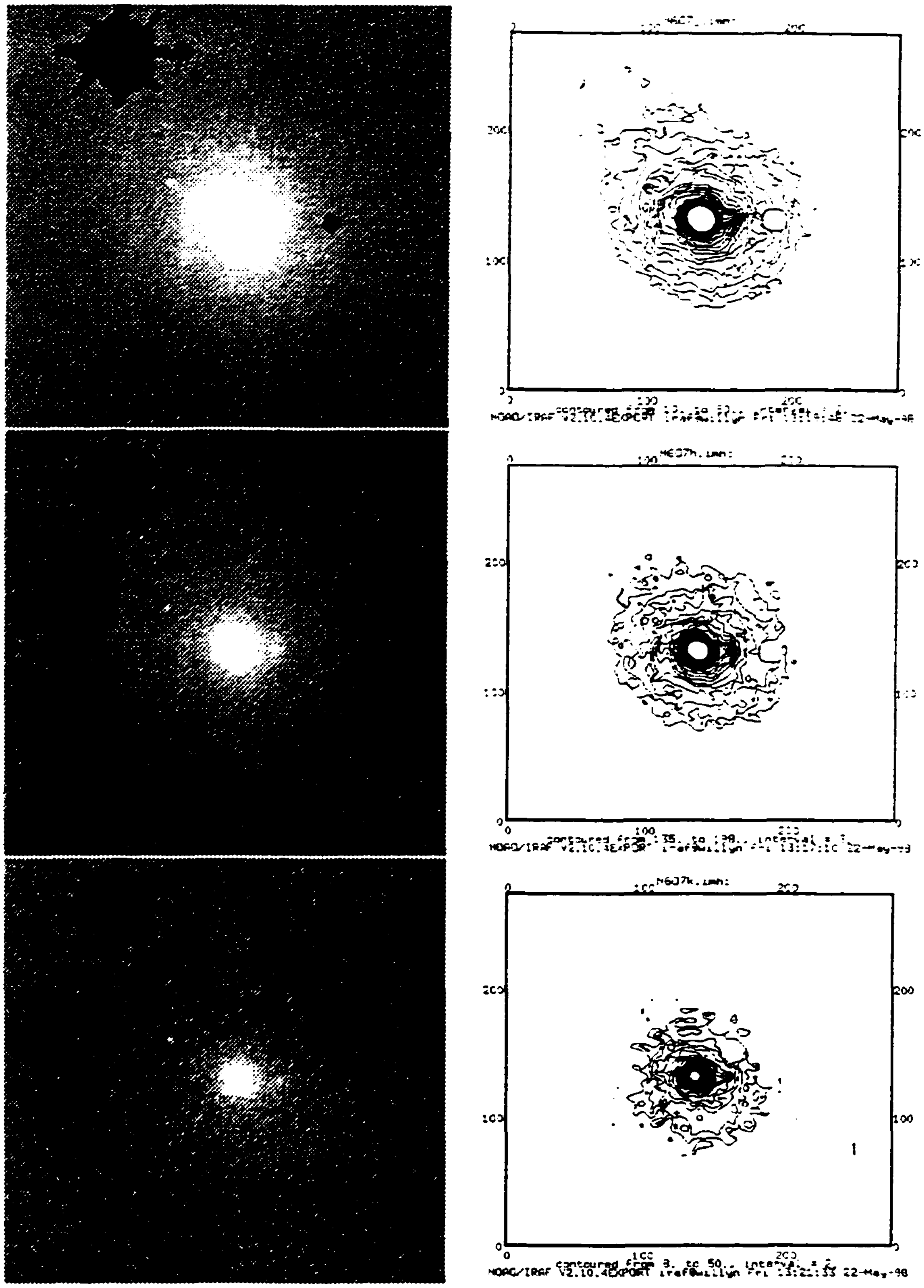

Fig. A.4a.— NGC4571 - J,H, and K Image and respective contour.

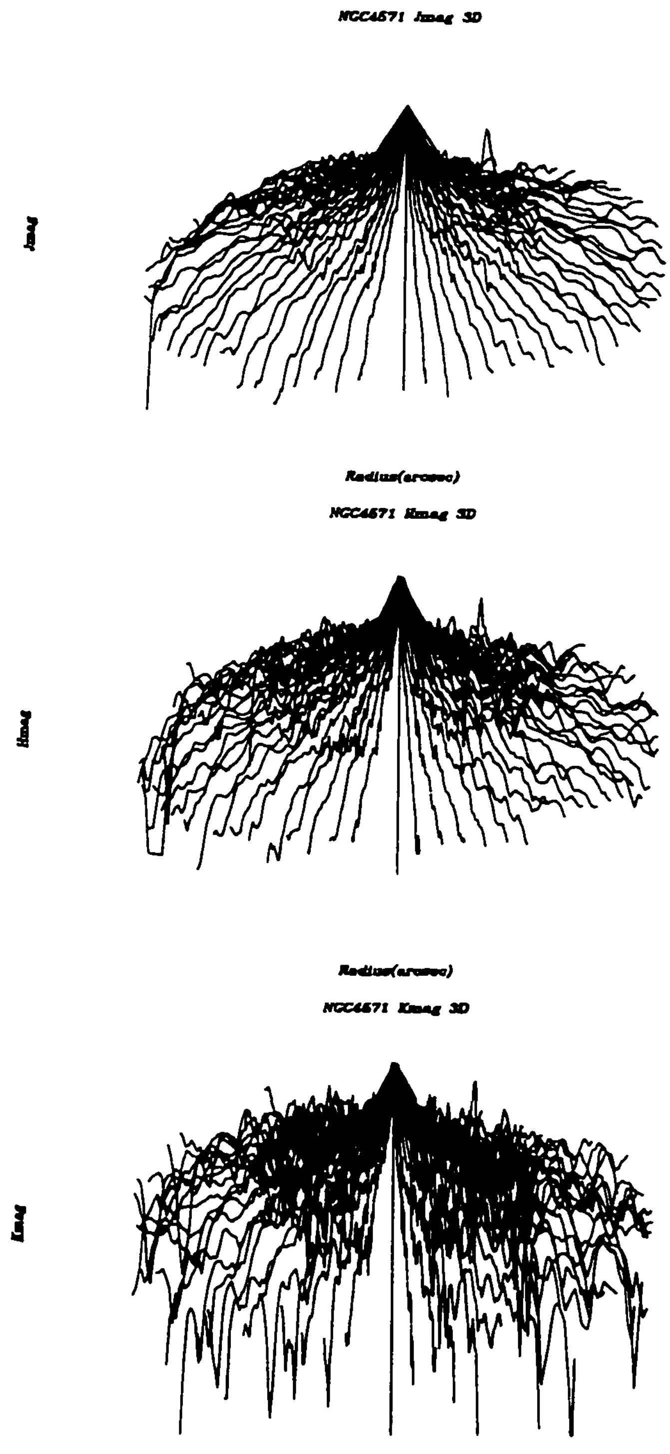

Fig. A.4b.— NGC4571 - J,H, and K 3-D Profiles.

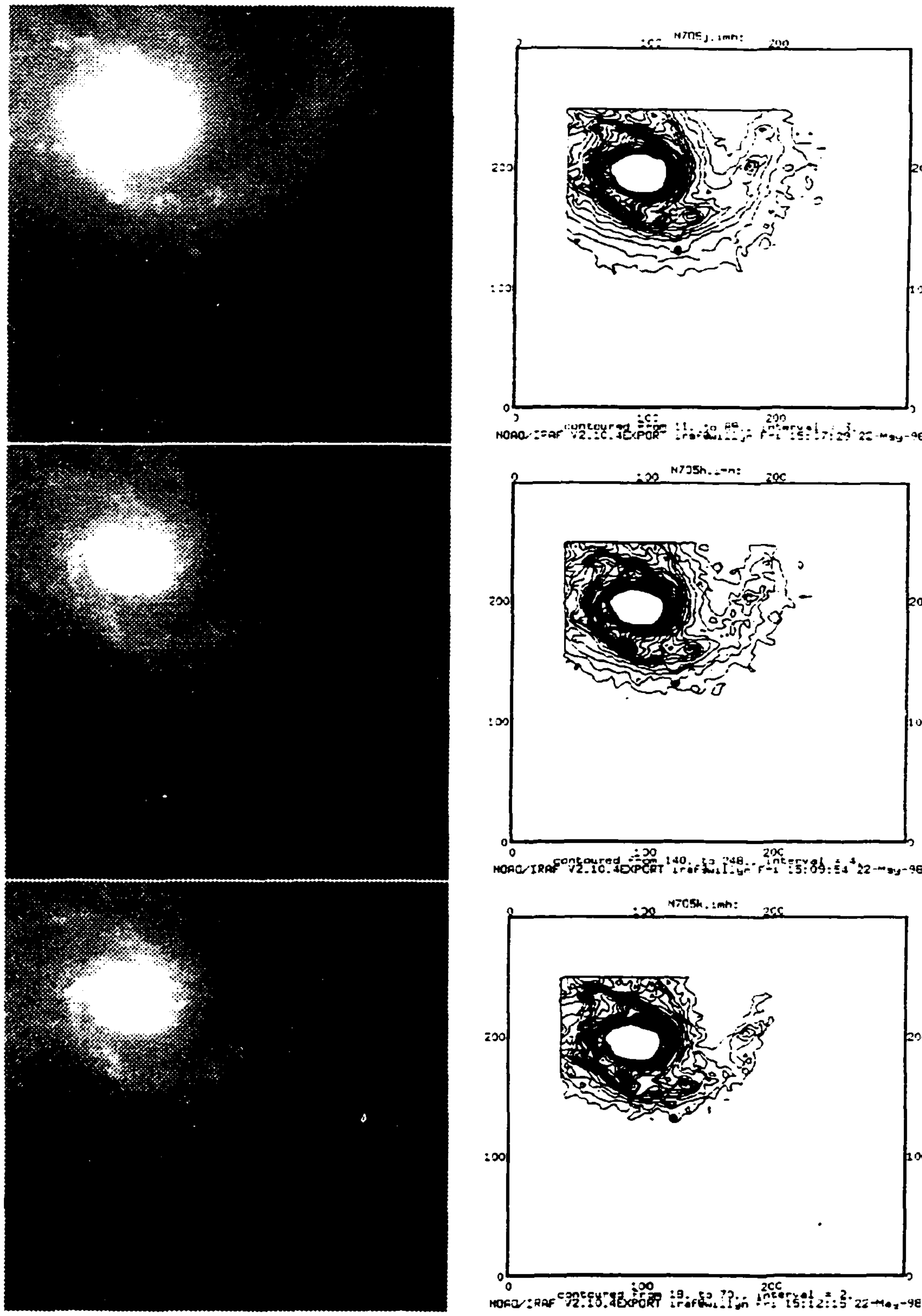

Fig. A.5a.— NGC4254 - J,H, and K Image and respective contour.

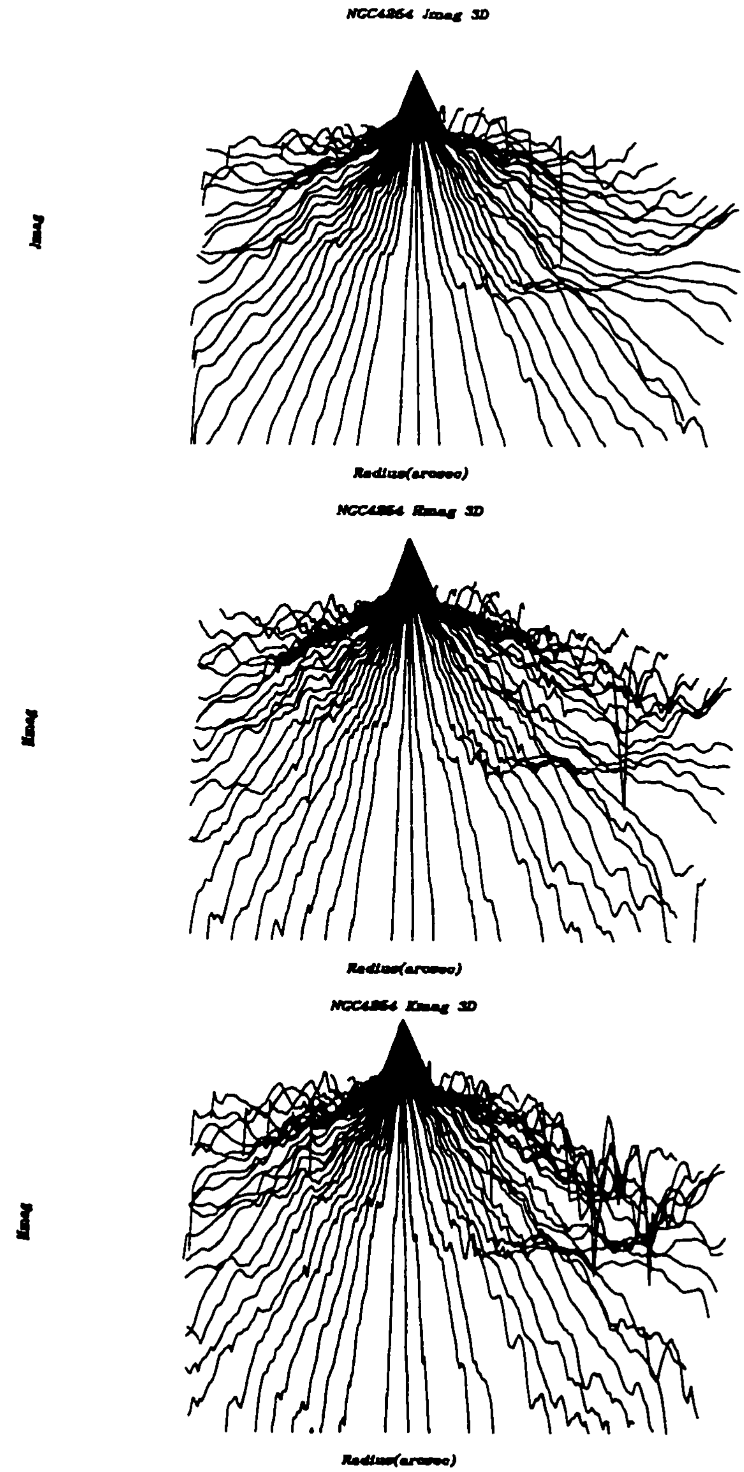

Fig. A.5b.— NGC4254 - J,H, and K 3-D Profiles.

REFERENCES

[Acker et al. 1989]Acker. A.. Köppen. J., Stenhold. M.. & Jasnewicz. G. 1989. A&A. 80. 201

[Adams et al. 1984]Adams. S.. Seaton. M.J.. Howarth. I.D. & Aurière. M. 1984. MNRAS. 207. 471

[Adam & Köppen 1985]Adam. J. & Köppen. J. 1985. A&A. 142. 461

[Aller et al. 1979]Aller. L.H.. Ross. J.E.. Keyes. C.D.. & Czyak. S.J. 1979. Ap&SS. 64. 347

[Anderson et al. 1980]Anderson. R.. 1980. ApJ. 230. 121

[Andredakis & Sanders 1994]Andredakis. Y.C. & Sanders. R.H. 1994. MNRAS. 267. 283

[Aller & Czyzak 1983]Aller. L.H. & Czyak, S.J. 1983. Ap&SS. 51. 211

[Arfken & Weber 1995]Arfken. G.B. & Weber, H.J., in *Mathematical Methods of Physicists*. 4th ed.. 1995. Academic Press: New York. p. 664

[Arimoto & Yoshii 1986]Arimoto, N., & Yoshii, Y.. 1986, à. 164. 260

[Arsenault et al. 1988]Arsenault, R., Boulesteix, J., Georgelin. Y.. & Roy. J.R.. 1988. à. 200, 29

[Auer & Mihalas 1969]Auer, L.H., & Mihalas, D., 1969. ApJ. 158. 641

[Auer & Mihalas 1970]Auer, L.H., & Mihalas. D., 1970, MNRAS. 149. 65

[Bahcall & Kylafis 1985]Bahcall. J.N. & Kylafis. N.D. 1985. ApJ. 288. 252

[Balcells & Peletier 1994]Balcells. M. & Pelerier, R.F. 1994. AJ. 107. 135

[Baldwin et al. 1991]Baldwin. J.A.. Ferland. G.J.. Martin. P.G.. Corbin. M.R.. Cota. S.A.. Peterson. B.M.. & Slettebak. A.. 1991. ApJ. 374. 580

[Barbon et al. 1989]Barbon. R.. Cappellaro. E.. & Turatto. M.. 1989. A&AS. 81. 421

[Barker 1980]Barker. T. 1980. Ap.J.. 237. 482

[Barker 1983]Barker. T. 1983. Ap.J.. 270. 641

[Barker & Cudworth 1984]Barker. T. & Cudworth. K.M. 1984. ApJ. 278. 610

[Binggeli et al. 1987]Binggeli. B.. Tammann. G.A.. & Sandage. A.. 1987. AJ. 94. 251

[Binney 1982]Binney. J.. in *Morphology and Dynamics of Galaxies*. ed. L. Martinet & M. Mayor. 1982. Sauverny. Switzerland: Geneva Observatory. p. 1

[Binney & Tremaine 1987]Binney. J. & Tremaine. S.. in *Galactic Dynamics*. ed. J. Ostriker 1987. Princeton University Press. New Jersey. p. 89

[Boeshaar & Bond]Boeshaar. G.O. & Bond. H.E.. 1977. ApJ. 213. 421

[Boothroyd & Sackmann 1988]Boothroyd. A.I. & Sackmann. I.J. 1988. ApJ. 328. 653

[Bothun et al. 1984]Bothun. G.D.. Romanishin. W.J.. Strom. S.E.. & Strom. K.M. 1984. AJ. 89. 1300

[Buell 1998]Buell. J. 1998. Ph.D. Thesis. Univ. Oklahoma

[Cardelli et al. 1989]Cardelli, A.J., Clayton. G.C.. & Mathis. J.S. 1989. AJ. 345. 245

[Cayatte et al. 1990]Cayatte. V.. van Gorkom. J.H.. Balkowski. C.. & Kotanyi. C. 1990. AJ. 100, 604

[Charlot & Bruzual 1991]Charlot. S.. Bruzual. G. 1991. ApJ. 367. 126

[Clegg & Middlemass 1987]Clegg, R.E.S. & Middlemass, D. 1987, MNRAS, 228, 759

[Clegg et al. 1987]Clegg, R.E.S., Peimbert, M., & Torres-Peimbert, S. 1987, MNRAS, 224, 761

[Cohen & Gillett 1989]Cohen, J.G. & Gillett, F.C., 1989, ApJ, 346, 803

[Cowan 1996]Cowan, J., McWilliam, A., Sneden, C., Burris, D.L., & Preston, G., 1996, ApJ, In preparation

[Diaz 1989]Diaz, A.I. 1989, in *Evolutionary Phenomena in Galaxies*, ed. J.E. Beckman, B.E.J. Pagel (Cambridge University Press, Cambridge), p. 377

[Diaz & Tosi 1984]Diaz, A.I. & Tosi, M. 1984, MNRAS, 208, 365

[de Jong 1996]de Jong, R.S., 1996, A&A, 313, 377

[Dopita & Ryder 1994]Dopita, M.A. & Ryder, S.D., 1994, ApJ, 430, 163

[de Vaucouleurs 1948]de Vaucouleurs, G., 1948, ARA&A, 11, 247

[de Vaucouleurs 1958]de Vaucouleurs, G., 1958, ApJ, 128, 465

[de Vaucouleurs & Longo 1988]de Vaucouleurs, G. & Longo, A., 1988, in *Catalogue of Visual and Infrared Photometry of Galaxies from 0.5μm to 10μm*, (1961-1985), The University of Texas Monographs in Astronomy, No. 5.

[de Vaucouleurs et al. 1991]de Vaucouleurs, G., de Vaucouleurs, A., Corwin, H.G., Jr., Buta, R.J., Paturel, G., & Fouque', P., 1991, in *Third Reference Catalogue of Bright Galaxies*, (New York: Springer) (RC3).

[Devereux et al. 1987]Devereux, N.A., Becklin, E.E., & Scoville, N. 1979, ApJ, 312, 529

[Dolidze & Dzhimshelejshvili 1966]Dolidze. M. & Dzhimshelejshvili. G.N. 1966. Astr. Tsirk.. 7

[Ellis et al. 1992]Ellis. T.. Drake. R.. Fowler. A.M.. Gatley. I.. Heim. J.. Luce. R.. Merrill. K.M.. Probst. R... & Bucholtz. N.. 1992. in *Infrared Cameras for Astronomy. Procedings of SPIE. 1765. 94.*

[Faber & Gallager 1979]Faber. S.M. & Gallager. J.S. 1979. ARA&A.17. 135

[Ferland 1990]Ferland. G. J. 1990. Ohio State University Report 90-02.

[Frogel 1985]Frogel. J.A. 1985. ApJ. 298. 528

[Garnett & Dinerstein 1988]Garnett. D.R. & Dinerstein. H.L. 1988. AJ. 95. 119

[Garnett & Dinerstein 1989]Garnett. D.R. & Dinerstein. H.L. 1989. PASP. 101. 541

[Gillett et al. 1989]Gillett. F.C.. Jacoby. G.H.. Joyce. R.R.. Cohen. J.G.. Newyebauer. G.. Suifer. B.T.. Nakajima. T.. & Matthews. K.. 1989. ApJ. 338. 862

[Gilroy et al. 1988]Gilroy. K.K.. Sneden. C.. Pilachowski. C.A.. & Cowan. J.C. 1988. ApJ. 327. 298

[Giovanelli & Haynes 1985]Giovanelli. R. & Haynes. M. 1985. ApJ. 292. 404

[Guhathakurta et al. 1988]Guhathakurta. P.. van Gorkom. J.H.. Kotanyi. C.G.. & Balkowski, C. 1988. AJ. 96. 851

[Güsten & Mezger 1982]Güsten, R. & Mezger. P.G. 1982. Vistas Astr.. 26. 159

[Green et al. 1987]Green, E.M.. Demarque P.. & King, C.R. 1987. in *The Revised Yale Isochrones and Luminosity Functions.* (Yale University Observatory: New Haven)

[Grevesse & Anders 1989]Grevesse. N. & Anders. E. 1989. Cosmis Abundances of Matter. AIP Conf. Prec. 183. ed. C.J. Waddington. (New York:AIP).

[Haro 1951]Haro. G. 1951. PASP. 63. 144

[Hawley & Miller 1978]Hawley. S.A.& Miller. J.S.. 1978 ApJ. 220. 609

[Haynes 1990]Haynes. M.P.. 1990. in *Clusters of Gala . s.* ed. W.R. Oegerle. M.J. Fitchett. & L. Danly (Cambridge University Press. Cambridge). p. 177

[Henry et al. 1992]Henry. R.B.C.. Pagel. B.E.J.. Lasseter. D.F.. & Chincarini. G.L. 1992 MNRAS. 258. 321

[Henry et al. 1994]Henry. R.B.C.. Pagel. B.E.J.. & Chincarini. G.L. 1994 MNRAS. 266. 421

[Henry & Howard 1995]Henry. R.B.C. & Howard. J.W. 1995 ApJ. 438. 170

[Henry et al. 1996]Henry. R.B.C.. Kwitter. K.B.. & Howard. J.W. 1996 ApJ. 458. 215

[Héraudeau et al. 1996]Héraudeau Ph.. Simien. F. & Mamon. G.A. 1996. A&AS. 117. 417

[Hodge & Kennicutt 1983]Hodge. P.W.. & Kennicutt. R.C.. 1983 AJ. 88. 296

[Hubble 1930]Hubble E.. 1930. ApJ. 71. 231

[Huchra 1984]Huchra. J. 1984. Center for Astrophysics Preprint No. 2067

[Hunt et al. 1997]Hunt L.E.. Malkan. M.A.. Salvati. M.. Mandolesi. N.. Palazzi. E.. & Wade. R.. 1997. ApJS. 108. 229

[Husfield & Kudritzki 1984]Husfield, D.. Kudritzki. R.P.. Simon. K.P.. & Clegg. R.E.S. 1984. A&A. 134. 139

[Iben 1983]Iben, I. 1983, ApJ, 275, L23

[Iben & Renzini 1983]Iben, I. & Renzini, A. 1983, ARA&A, 21, 271

[Jedrzejewski 1987]Jedrzejewski, R. 1987, MNRAS, 226, 747

[Jensen & Thuan]Jensen, E., Thuan, T. : *Photometry, Kinematics, & Dynamics of Galaxies* ed. D.S. Evans, 1979, Univ. Texas Press, Austin, p. 113

[Keel 1983]Keel, W.C., 1983, ApJS, 52, 229

[Kent et al. 1991]Kent, S.M., Dame, T., & Fazio, G. 1991, ApJ, 378, 131

[Kennicutt 1985]Kennicutt Jr., R.C. 1985, in *ESO Workshop on the Virgo Cluster Galaxies*, ed. O.G. Richter & B. Binggeli (Garching bei Munchen, Germany) p. 227

[Kennicutt 1983]Kennicutt Jr., R.C. 1983, ApJ, 272, 54

[Kennicutt 1989]Kennicutt Jr., R.C. 1989, ApJ, 344, 685

[King 1966]King, I.R., 1966, AJ, 71, 64

[Kodaira 1986]Kodaira, K., Watanabe, M., & Okamura, S. 1986, ApJS, 62, 703

[Kormendy 1993]Kormendy, J. *IAU Symposium 153, Planetary Nebulae*, ed. H. deJonghe, H. J. Habring, 1993, Kluwer, Dordrecht, p. 209

[Kormendy & Illingworth 1982]Kormendy, J., Illingworth, F. 1982, ApJ, 256, 460

[Kormendy 1977]Kormendy, J., 1977, ApJ, 217, 406

[Kudritzki 1976]Kudritzki, R.P., 1976, A&A, 52, 11

[Kurucz 1991]Kurucz, R.L., in *Precision Photometry*, 1991, ed. A. Davis, Philip, Upgren, & James, p. 27

[Kwitter & Henry 1996]Kwitter, K.B., & Henry, R.B.C. 1996, ApJ, in press.

[Leitherer & Heckman 1995]Leitherer, C., & Heckamn, T.M., 1995, ApJS, 96, 9

[Maehara et al. 1986]Maehara, H., Okamura, S., Noguchi, T., He, X.T., & Liu, J., 1986, in *Second Japan-China Workshop on Stellar Activities and Observational Techniques*, Univerity of Kyoto, Kyoto, P. 71

[Maehara et al. 1987]Maehara, H., Okamura, S., Noguchi, T., He, X.T., Liu, J., Huang, Y.W., & Feng, X.C. 1987, A&A, 178, 221

[Martin & Roy 1992]Martin, P., & Roy, J.R., 1992, ApJ, 397, 463

[Matteucci 1989]Matteucci, F., 1989, in *Evolutionary Phenomena in Galaxies*, ed. J.E. Beckman, B.E.J. Pagel (Cambridge University Press, Cambridge), p. 297

[Matteucci 1992]Matteucci, F., 1992, in *Morphological and Physical Classification of Galaxies*, ed. G. Longo, M. Capaccioli, G. Brusarello (Kluwer Academic Publishers, Dordrecht), p. 245

[Mendoza 1983]Mendoza, C. *IAU Symposium 131, Planetary Nebulae*, ed. S. Torres-Peimbert, Kluwer, Dordrecht, p. 143

[Mendez et al. 1988]Mendez, R.H., Kudritzki, R.P., Herrero, A., Husfield, & D., Groth, H.G.G., 1988, A&A, 190, 133

[Mihalas 1978]Mihalas, D. *Stellar Atmospheres*, 2nd Ed. (W.H. Freeman: San Francisco) 1978.

[Miller 1969]Miller, J., 1969 ApJ, 157, 1215

[O'Connell 1986]O'Connell, R.W., 1994, in *Nuclei of Normal Galaxies: Lessons from the Galactic Center*, ed. R. Genzel (Kluwer Academic Publishers, Dordrecht), p. 213

[O'Dell et al. 1964]O'Dell, C.R., Peimbert, M., & Kinman, T.D., 1964, ApJ, 140, 119

[Pagel & Edmunds 1981]Pagel, B.E.J. & Edmunds, M.G. 1981, ARA&A, 19, 77

[Pagel 1989]Pagel, B.E.J. 1989, Rev. Mex. Astr. Astrofis., 18, 161

[Pease 1928]Pease, F.G., 1928, PASP, 40, 342

[Peimbert 1990]Peimbert, M. 1990, Rep. Prog. Phys., 53, 1559

[Peimbert 1973]Peimbert, M. 1973, Mem. Soc. Roy. Sci. Liége, 5, 307

[Peletier 1989]Peletier, R.F. 1989, Ph.D. Thesis, University of Groningen, The Netherlands

[Peletier et al. 1994]Peletier, R.F., Valentijn, E.A., Moorwood, A.F., & Freudling W. 1994, Ap&SS, 108, 621

[Peletier & Balcells 1996]Peletier, R.F., & Balcells, M. 1996, AJ, 111, 2238

[Peña et al. 1989]Peña, M., Ruiz, M.T., Maza, J., & González, L.E. 1989, Rev. Mex. A&A, 17, 25

[Peña et al. 1990]Peña, M., Ruiz, M.T., Torres-Peimbert, & S., Maza, J. 1990, A&A, 237, 454

[Peña et al. 1991]Peña, M., Torres-Peimbert, S., & Ruiz, M.T. 1991, PASP, 103, 865

[Peña 1996]Peña, M., 1996, private communication

[Perek & Kohoutek 1967]Perek, L. & Kohoutek, L. 1967, *Catalogue of Galactic Planetary Nebulae*, Academia, Praha

[Phillips & Edmunds 1991]Phillips, S. & Edmunds, M.G. 1991 MNRAS, 251, 84

[Pierce et al 1992]Pierce, M.J., McClure, R.D., & Racine, R., 1992 ApJ, 393, 523

[Pitts & Tayler 1989]Pitts, E. & Tayler, R.J. 1989 MNRAS, 240, 373

[Rauscher 1995]Rauscher, B.J., 1995 AJ, 109, 1608

[Renzini et al. 1981]Renzini, A. & Voli, M. 1981 A&A, 94, 175.

[Romanishin 1998]Romanishin, W. 1998 Private Communication.

[Romanishin 1991]Romanishin, W. & Henry, R.B.C. 1991 KPNO Observing Time Request *Stellar Abundance Gradients in Virgo Spirals from IR Maps.*

[Romanishin 1990]Romanishin, W. 1990 AJ, 100, 373.

[Ryder & Dopita 1994]Ryder, S.D. & Dopita M.A. 1994 ApJ, 430, 142.

[Salpeter 1955]Salpeter, E.E. 1955 ApJ, 121, 161

[Sandage 1961]Sandage, A., 1961, in *The Hubble Atlas of Galaxies.* (Carnegie Institution of Washington, Washington D.C.)

[Sandage & Bedke 1988]Sandage, A. & Bedke, J., 1988, in *An Atlas of Galaxies Useful for Measuring the Cosmological Distance Scale.* (Washington, NASA) (NASA SP-496)

[Sarazin 1988]Sarazin, C.L., 1988, in *X-Ray Emissions from Clusters of galaxies.* (Cambridge University Press, Cambridge)

[Searle 1971]Searle, L., 1971, ApJ, 168,327

[Searle & Zinn 1978]Searle, L., & Zinn, R., 1978, ApJ, 225,357

[Scowen et al. 1992]Scowen, P.A., Dufour, R.J., & Hester, J.J. 1992, AJ, in press??

[Schönberner 1981]Schönberner. D. 1981. A&A. 103. 119

[Schönberner 1983]Schönberner. D. 1983. ApJ. 272. 708

[Shaw & Bidelman 1987]Shaw. R.A. & Bidelman. W.P. 1987. PASP. 99. 27

[Shaw & Gilmore 1989]Shaw. M.A. & Gilmore. G. 1989. MNRAS. 237. 903

[Shields et al. 1991]Shields. G.A.. Skillman. E.D.. & Kennicutt Jr.. R.C. 1991. ApJ. 371. 82

[Sibille et al. 1974]Sibille. F.. Lunel. M.. & Bergeat. J. 1974. Ap&SS. 30. 173

[Skillman et al. 1996]Skillman. E.D.. Kennicutt Jr.. R.C.. Shields. G.A.. & Zaritsky. D. 1996. ApJ. 462. 147

[Terndrup et al.1994]Terndrup. D.M.. Davies. R.L.. Frogel. J.A.. DePoy. D.L.. & Wells. L.A. 1994. ApJ. 432. 518

[Thronson et al. 1990]Thronson. H.A.. Majewski. S.. Descartes. L.. & Hereld. M. 1990. ApJ. 364. 456

[Thuan 1983]Thuan. T.X. 1983. ApJ. 268. 667

[Tinsley 1980]Tinsley. B.M.. 1980. Fund. of Cos. Phys. 5. 287

[Torres-Peimbert & Peimbert 1979]Torres-Peimbert. S.. & Peimbert. M. 1979. Rev. Mex. A&A. 4. 341

[Torres-Peimbert 1981]Torres-Peimbert. S.. Rayo. J.. & Peimbert. M. 1981. Rev. Mex. A&A. 6. 315

[Torres-Peimbert et al. 1990]Torres-Peimbert. S.. Peimbert. M.. & Peña. M. 1990. A&A. 233. 540

[van den Bergh et al. 1990]van den Bergh, S., Pierce, M.J., & Tully, R.B., 1990, ApJ, 359, 4

[VandenBerg 1985]VandenBerg, D.A. 1985, ApJS, 58, 711

[Vazdekis et al. 1996]Vazdekis, A., Casuso, E., Peletier, R.F., & Beckman, J.E. 1996, ApJS, 106, 307

[Véron-Cetty & Véron 1993]Véron-Cetty, M.P., Véron, P., 1993, in *A Catalogue of Quasars and Active Galactic Nuclei*, (ESO, Garching) 6th ed.

[Vila-Costas & Edmunds 1992]Vila-Costas, M.B. & Edmunds, M.G. 1992, MNRAS, 259, 121

[Wainscoat et al. 1989]Wainscoat, R.J., Freeman, K.C., & Hyland, A.R. 1989, ApJ, 337, 163

[Webster 1988]Webster, B.L., 1988, MNRAS, 230, 377

[Warmels 1986]Warmels, R.H., 1986, PH.D. Thesis, Univ. Groningen

[Warmels 1988]Warmels, R.H., 1988, à, 72, 427

[Werner & Heber 1991]Werner, K. & Heber, U., in *Stellar Atmospheres: Beyond Classical Models*, ed. L Crivellari et al. 1991, P. 341

[Whitmore 1990]Whitmore, B.C., 1990, in *Clusters of Galaxies*, ed. W.R. Oegerle, M.J. Fitchett, & L. Danly (Cambridge University Press, Cambridge), p. 139

[Whitmore et al. 1985]Whitmore, B.C., McElroy, D.B., & Tonry, J.L. 1985, ApJS, 59, 1

[Wilson et al. 1972]Wilson, W.J., Schwarz, P.R., Neugebauer, G. Harvey, P.M., & Becklin, E.E. 1972, ApJ, 177, 523

[Willner et al. 1972]Willner, S.P., Becklin, E.E., & Visvanathan, N. 1972, ApJ, 175, 609

[Worthey 1994]Worthey, G. 1994, ApJS, 95, 107

[Wyse & Gilmore 1988]Wyse, R.F.G. & Gilmore, G. 1988, ApJ, 95, 1404

[Zaritsky et al. 1989]Zaritsky, D., Elston, R., & Hill, J.M. 1989, AJ, 97, 97

[Zeippen et al. 1987]Zeippen, C.J., Butler, K., & LeBourlot, J. 1987, A&A, 188, 251

This thesis was prepared with the Joe LaTeX macros v1.0.

IMAGE EVALUATION TEST TARGET (QA-3)

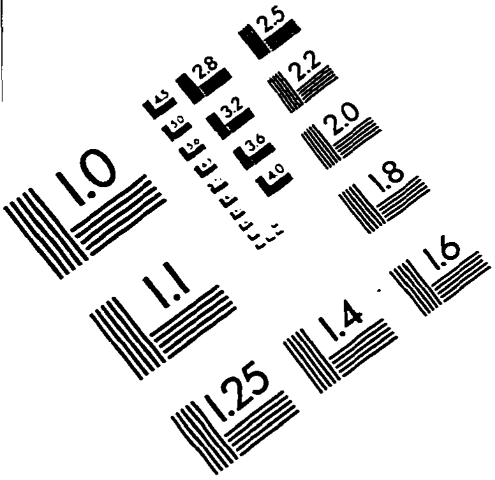

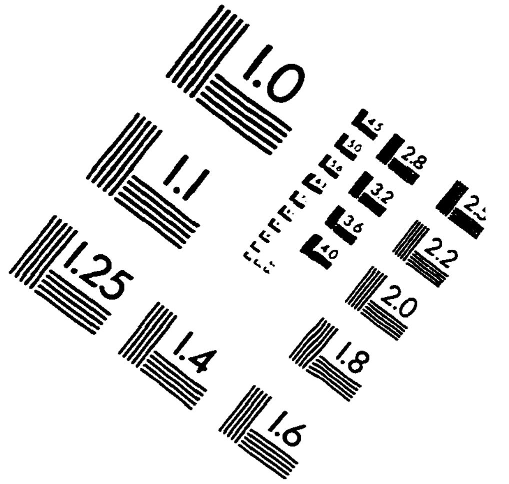

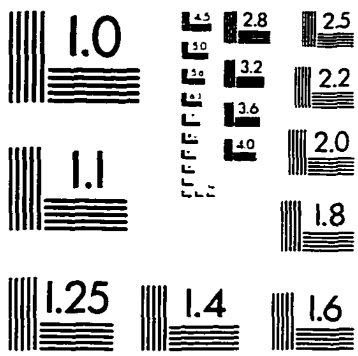

150mm

6"

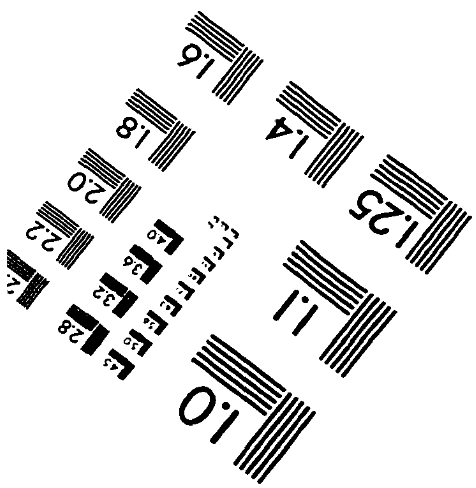

APPLIED IMAGE, Inc
1653 East Main Street
Rochester, NY 14609 USA
Phone: 716/482-0300
Fax: 716/288-5989